nature cancer

Article

https://doi.org/10.1038/s43018-022-00506-7

Fucosylation of HLA-DRB1 regulates CD4$^+$ T cell-mediated anti-melanoma immunity and enhances immunotherapy efficacy

Received: 6 July 2022

Accepted: 14 December 2022

Published online: 23 January 2023

Check for updates

Daniel K. Lester[1,2,3], Chase Burton[1,2,3,4,5], Alycia Gardner[2,4,5], Patrick Innamarato[2,4,5], Krithika Kodumudi[4,5], Qian Liu[1,2,3], Emma Adhikari[1,2,3], Qianqian Ming[3,6], Daniel B. Williamson[7], Dennie T. Frederick[8], Tatyana Sharova[8], Michael G. White[9], Joseph Markowitz[5,10], Biwei Cao[11], Jonathan Nguyen[12], Joseph Johnson[13], Matthew Beatty[4,5], Andrea Mockabee-Macias[1,3], Matthew Mercurio[1,3], Gregory Watson[1,3], Pei-Ling Chen[14], Susan McCarthy[12], Carlos MoranSegura[12], Jane Messina[14], Kerry L. Thomas[15], Lancia Darville[16], Victoria Izumi[16], John M. Koomen[16,17], Shari A. Pilon-Thomas[4,5], Brian Ruffell[4,5], Vincent C. Luca[3,6], Robert S. Haltiwanger[7], Xuefeng Wang[11], Jennifer A. Wargo[9,18], Genevieve M. Boland[8,19] & Eric K. Lau[1,3] ✉

Immunotherapy efficacy is limited in melanoma, and combinations of immunotherapies with other modalities have yielded limited improvements but also adverse events requiring cessation of treatment. In addition to ineffective patient stratification, efficacy is impaired by paucity of intratumoral immune cells (itICs); thus, effective strategies to safely increase itICs are needed. We report that dietary administration of L-fucose induces fucosylation and cell surface enrichment of the major histocompatibility complex (MHC)-II protein HLA-DRB1 in melanoma cells, triggering CD4$^+$ T cell-mediated increases in itICs and anti-tumor immunity, enhancing immune checkpoint blockade responses. Melanoma fucosylation and fucosylated HLA-DRB1 associate with intratumoral T cell abundance and anti-programmed cell death protein 1 (PD1) responder status in patient melanoma specimens, suggesting the potential use of melanoma fucosylation as a strategy for stratifying patients for immunotherapies. Our findings demonstrate that fucosylation is a key mediator of anti-tumor immunity and, importantly, suggest that L-fucose is a powerful agent for safely increasing itICs and immunotherapy efficacy in melanoma.

Melanoma is one of the deadliest skin cancers, with an estimated ~99,780 new diagnoses and ~7,650 deaths in 2022 in the United States alone (American Cancer Society Facts and Figures, 2022). Despite reports of striking efficacy, durable immunotherapy responses have been limited to subsets of patients[1,2]. In an attempt to improve responses, clinical trials have tested combinations of immunotherapies with other therapeutic interventions, with limited success[1,3]. Unfortunately, patients often experience substantial adverse events, sometimes resulting in cessation of treatment. Ineffective patient stratification is another ongoing challenge for the effective administration

A full list of affiliations appears at the end of the paper. ✉e-mail: eric.lau@moffitt.org

of immunotherapies. Although biomarkers of responsiveness remain under active investigation, one commonality of poor response is insufficient abundance and tumor-suppressive activity of itICs[4]. Therefore, elucidating itIC biology and developing safe and effective strategies to increase tumor-suppressive itICs are crucial for improving the efficacy of immunotherapies and related biomarkers.

Fucosylation, the conjugation of glycoproteins with the sugar L-fucose (L-fuc) at asparagine or serine–threonine residues (*N*- or *O*-linked, respectively) is mediated by 13 fucosyltransferases (FUTs) and impacts protein functions that are crucial for immune and developmental processes[5,6]. Whereas altered fucosylation has been reported in a number of cancers, our understanding of its mechanisms and functional contributions is limited[7,8]. We previously found that global fucosylation decreases during melanoma progression, and increased tumor fucosylation levels correlate with favorable patient-survival outcomes[9]. Furthermore, increasing melanoma fucosylation in a syngeneic mouse model reduced tumor growth and metastasis and significantly increased itICs. How fucosylation regulates anti-tumor immunity, however, was unknown. Here, we report that dietary L-fuc can regulate the biology and interactions between $CD4^+$ T and melanoma cells via cell surface stabilization of an MHC-II protein, which robustly induces itICs and anti-melanoma immunity. Tumoral MHC-II protein expression, which is known to trigger $CD4^+$ T cell-mediated responses, is associated with immune-mediated tumor suppression and increased responsiveness to immunotherapies[10,11]. Our findings demonstrate the ability of L-fuc to improve the efficacy of immunotherapies by promoting MHC-II–$CD4^+$ T cell-mediated responses and identify fucosylation-based biomarkers that may enhance patient stratification.

Results

Increased fucosylation blunts melanoma growth and increases itICs

We initially assessed how L-fuc-induced changes in itICs might contribute to melanoma suppression using a $NRAS^{G13D}$-mutant mouse melanoma (SW1) model[9]. Oral L-fuc administration increased tumor fucosylation (approximately twofold), reduced tumor growth (~50%) and increased total itICs (~10–50-fold) (including $CD3^+$ ($CD4^+$ and $CD8^+$) T, natural killer (NK), macrophage, dendritic cell (DC) and myeloid-derived suppressor (MDSC)-like cell subpopulations, without altering splenic lymphocyte profiles) (Extended Data Fig. 1a, Fig. 1a,b and Extended Data Fig. 1b,c, respectively). Of total itICs, $CD4^+$ and $CD8^+$ T cells were the most increased subpopulation (approximately doubled) (Fig. 1c,d). Oral L-fuc induced similar changes in tumor fucosylation, growth and itICs (specifically increased $CD4^+$ and $CD8^+$ T cells) in a $BRAF^{V600E}$-mutant mouse melanoma (SM1) model[12] (Extended Data Fig. 1d–j, respectively). By contrast, L-fuc did not reduce SW1 tumor growth in immunodeficient mice (Extended Data Fig. 1k), confirming that the presence and activity of itICs are essential for L-fuc-triggered tumor suppression.

We confirmed an essential role for tumor-specific fucosylation by overexpressing murine fucokinase (mFuk) in SW1 melanoma cells to exclusively increase tumor fucosylation. mFuk expression alone suppressed tumor growth and increased total itICs comparably to oral L-fuc administration alone. Again, $CD4^+$ and $CD8^+$ T cells were the most increased itICs (Extended Data Fig. 1l,m and Fig. 1e–h). These data indicate that melanoma-specific fucosylation is an essential determinant of L-fuc-triggered itIC induction and tumor suppression, regardless of any other physiological host effects that L-fuc may elicit (for example, microbiome or metabolic effects).

Correlations between tumor fucosylation and $CD3^+$ T cells in humans were assessed by immunofluorescently analyzing a 40-patient melanoma microarray. Patients with higher-than-median tumor fucosylation levels exhibited significantly increased intratumoral $CD3^+$ T cell densities (Fig. 1i). Intriguingly, average melanoma fucosylation levels were lower in male patients (Fig. 1j) but exhibited a stronger association with intratumoral $CD3^+$ T cells (Fig. 1k).

These data indicate that melanoma fucosylation substantially shapes the itIC landscape, correlates with increased intratumoral $CD3^+$ T cells in mice and humans and can be boosted by oral L-fuc to increase itICs and suppress *BRAF*- and *NRAS*-mutant melanomas.

L-fuc triggers $CD4^{\pm}$ T cell-induced itICs and alters $CD4^{\pm}$ T cell biology

The contribution of $CD4^+$ and $CD8^+$ T cells to L-fuc-triggered tumor suppression was assessed by immunodepletion in the SW1 model. L-fuc reduced tumor growth by >50% in control and $CD8^+$ T cell-depleted mice, whereas this effect was completely abrogated by $CD4^+$ T cell depletion (Fig. 1l–n, immunodepletion confirmed by splenic profiling, and Extended Data Fig. 1n,o). Consistent with known roles for $CD4^+$ T cells in recruiting and activating tumor-suppressive itICs[13], $CD4^+$ T cell depletion also blocked L-fuc-induced increases in total itICs, including intratumoral NK cells, DCs and $CD8^+$ T cells, observed in control mice (Extended Data Fig. 1p and Fig. 1o). Similarly, in the SM1 model, $CD4^+$ but not $CD8^+$ T cell depletion abrogated L-fuc-triggered tumor suppression and increases in total itICs and itIC subpopulations (immunodepletion confirmed by splenic profiling, Extended Data Fig. 1q–w)).

Phosphoproteomic and fucosylated proteomic analyses revealed that L-fuc mechanistically regulates $CD4^+$ T cell biology by significantly altering protein kinase A (PKA) and (to a lesser extent) actin signaling, potentially via integrin B5, an upstream regulator of both of these pathways[14] that we discovered to be one of five proteins most highly bound to *Aleuria aurantia* lectin (AAL) (and likely fucosylated) in human peripheral blood monocyte (PBMC)-derived, CD3–CD28-activated $CD4^+$ T cells, as well as Jurkat cells treated with L-fuc (Extended Data Fig. 2a–f). The fact that integrin, PKA and actin signaling have been

Fig. 1 | Increasing melanoma fucosylation reduces tumor growth and increases itIC abundance, particularly $CD4^+$ and $CD8^+$ T cells. Volumetric growth curves, total itIC counts, percent itIC subpopulations ($CD3^+$ T cells, DCs, NK cells, macrophages (MΦ) and MDSC-like (MDSC) cells) and intratumoral $CD3^+CD4^+$ ($CD4^+$) and $CD3^+CD8^+$ ($CD8^+$) T cell counts of SW1 tumors (**a**–**d**, respectively) or of empty vector (EV)- or mFuk-expressing SW1 tumors (**e**–**h**, respectively) in C3H/HeN mice. Red triangle, initiated L-fuc (LF) supplementation. The growth curves show mean ± standard error of the mean (s.e.m.) from groups of mice as follows: $n = 11$ control and $n = 10$ L-fuc-fed mice (**a**), $n = 4$ mice per group (**b**,**d**), $n = 7$ mice per group (**e**), $n = 3$ mice per group (**f**,**h**) (b,d,f,h show mean ± s.e.m.). **i**, Association of melanoma-specific fucosylation and $CD3^+$ T cell density (log_2 scale) in a 40-patient melanoma tissue microarray (med = median fucosylation signal per melanoma cell). **j**, Box plots showing lower melanoma-specific fucosylation in male ($n = 22$) versus female ($n = 18$) patients. The minima and maxima represent the minimum and maximum tumor fucosylation values while the centra represent median values. *P* values shown are two-sided *P* values derived from the Spearman correlation test. **k**, Scatterplots show higher correlation (cor) between melanoma-specific fucosylation and $CD3^+$ T cell density (log_2 scale) in male (Spearman's $\rho = 0.43$; $P = 0.036$) versus female (Spearman's $\rho = 0.25$; $P = 0.3367$) patients. The gray bands highlight 95% confidence bands for the prediction line (based on linear regression). Volumetric growth curves for SW1 tumors in PBS (control)-injected (both (control and L-fuc) groups, $n = 7$ mice) (**l**), $CD8^+$ T cell- (both groups, $n = 6$ mice) (**m**) or $CD4^+$ T cell- (**n**) immunodepleted C3H/HeN mice (both groups, $n = 7$ mice). **o**, Comparison of intratumoral NK, DC, $CD8^+$ T and $CD4^+$ T cell subpopulations (absolute cell numbers) from tumors ($n = 4$ (control) and $n = 3$ (L-fuc)) (**l**), (for both groups, $n = 4$) (**n**). All error bars represent s.e.m. With the exception of **e**, for which one-way ANOVA was performed, two-sided *t*-tests were performed for all other analyses.

https://doi.org/10.1038/s43018-022-00506-7

reported to mediate T cell activation, motility and immune synapse formation[15,16] suggests that L-fuc promotes T cell trafficking to the tumor, a notion confirmed using an SW1 melanoma C3H mouse model treated with or without FTY720 (an inhibitor of lymph node egress). Inhibition of lymph node egress completely abrogated L-fuc-triggered tumor suppression (Fig. 2a,b). Strikingly, L-fuc-triggered tumor suppression was associated with increases in intratumoral CD4$^+$ T central and effector memory subpopulations that were abrogated by FTY720 (Fig. 2a,c (blue dashed boxes) and Supplementary Table 1), consistent with the role that PKA plays in regulating memory phenotype in T cells[17]. Intriguingly, oral L-fuc induced significant, albeit transient, increases in intratumoral monocyte-derived DCs (moDCs) and lymph node conventional DC2 (cDC2) cells, which can promote memory CD4$^+$ T cell phenotypes and cross-talk with CD4$^+$ T cells to mediate tumor

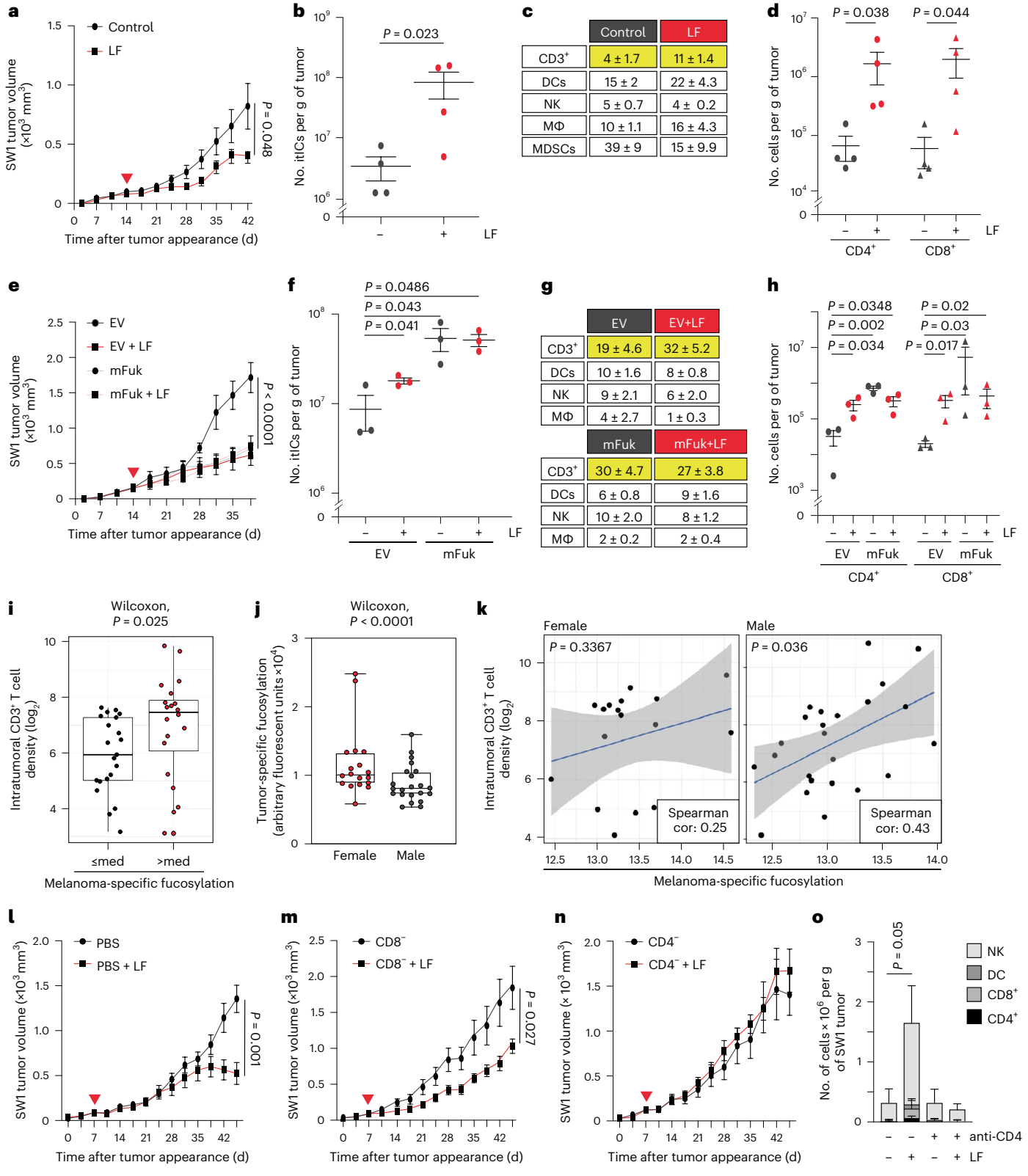

https://doi.org/10.1038/s43018-022-00506-7

a

CD4⁺ T cells	
Naive	CD45⁺CD11b⁻CD4⁺CD44⁻CD62L⁺CD95⁻
Stem central memory	CD45⁺CD11b⁻CD4⁺CD44⁻CD62L⁺CD95⁺
Central memory	CD45⁺CD11b⁻CD4⁺CD44⁺CD62L⁺CD95⁺
Effector memory	CD45⁺CD11b⁻CD4⁺CD44⁺CD62L⁻CD95⁺

CD8⁺ T cells	
Naive	CD45⁺CD11b⁻CD8⁺CD44⁻CD62L⁺CD95⁻
Stem central memory	CD45⁺CD11b⁻CD8⁺CD44⁻CD62L⁺CD95⁺
Central memory	CD45⁺CD11b⁻CD8⁺CD44⁺CD62L⁺CD95⁺
Effector memory	CD45⁺CD11b⁻CD8⁺CD44⁺CD62L⁻CD95⁺

DCs	
cDC1	CD45⁺CD11c⁺F4 80⁻MHC-II⁺CD11b⁻CD103⁺
cDC2	CD45⁺CD11c⁺F4 80⁻MHC-II⁺CD11b⁺CD103⁻FCγR1⁻
moDC	CD45⁺CD11c⁺F4 80⁻MHC-II⁺CD11b⁺CD103⁻FCγR1⁺

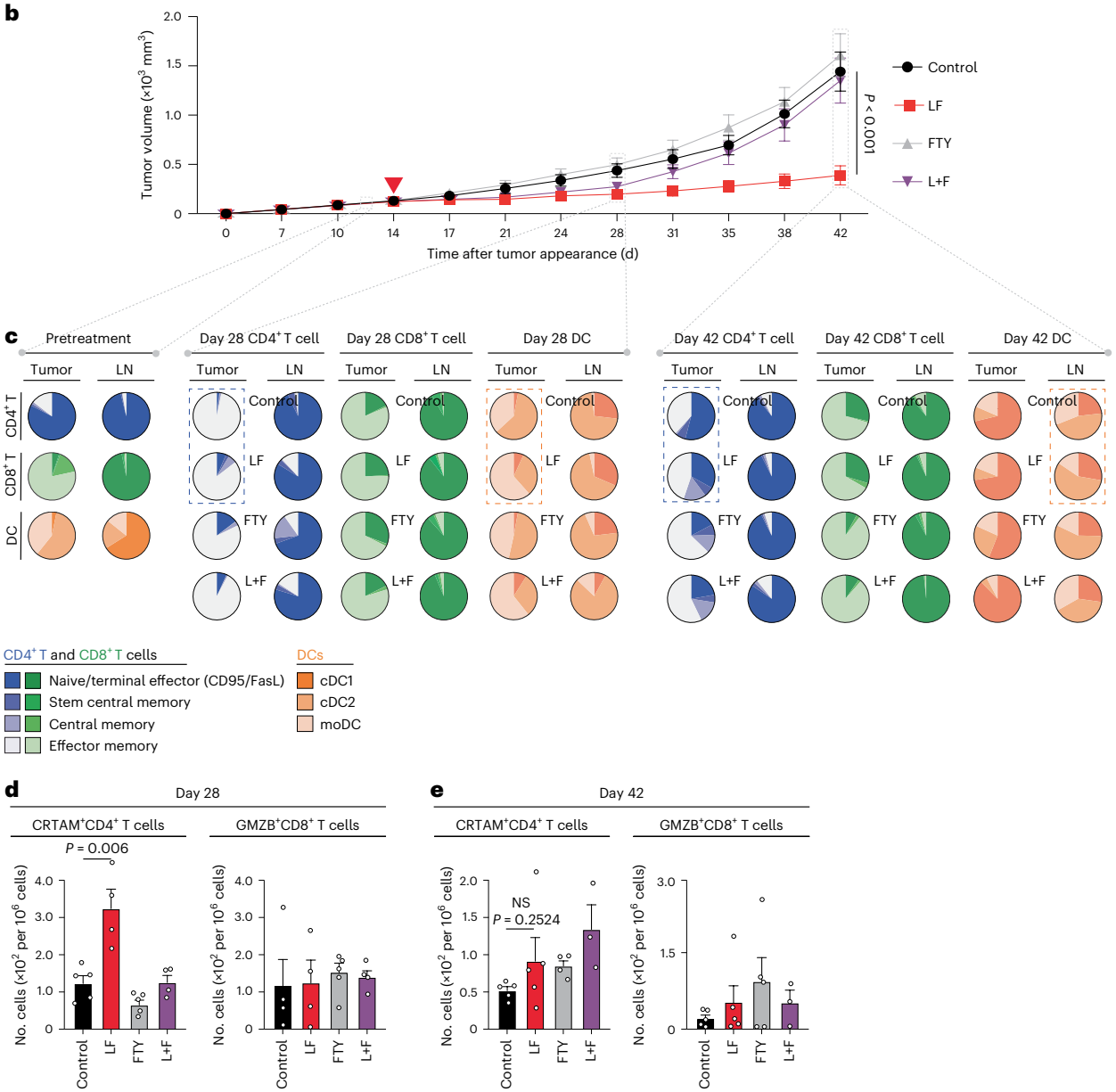

Fig. 2 | Lymph node egress is necessary for L-fuc-triggered tumor suppression; L-fuc increases intratumoral CD4⁺ T stem and central memory cells. a, Immune subpopulation markers use to profile by flow cytometry. **b**, Volumetric growth curves for SW1 tumors in C3H/HeN mice fed without (control, $n = 3$ mice) or with (L-fuc, $n = 10$ mice) L-fuc and treated with FTY720 (control mice were administered FTY720 (FTY) ($n = 10$ mice); L-fuc-supplemented mice were administered FTY720 (L + F) ($n = 10$ mice)). FTY720 was administered at 20 µg per mouse every 2 d starting on day 12, just before the initiation of L-fuc administration. **c**, Pie charts showing ratios of intratumoral or lymph node (LN)-resident CD4⁺ or CD8⁺ T cell subpopulations as well as DC subtypes from mice at days 14, 28 and 42 (each pie chart represents 4–5 mice). Assessment of cytotoxic CD4⁺ T cell populations (CRTAM⁺) and cytotoxic CD8⁺ T cell populations (GrzB⁺) from tumors at day 28 (**d**) ($n = 5$ mice for all groups except L-fuc, where $n = 4$ mice) and day 42 (**e**) ($n = 5$ mice each for control and L-fuc groups, $n = 4$ mice each for FTY and L + F groups). NS, not significant. Corresponding raw flow cytometric data for these charts are shown in Supplementary Table 1. The tumor growth curves and column charts show mean ± s.e.m. per group of mice.

https://doi.org/10.1038/s43018-022-00506-7

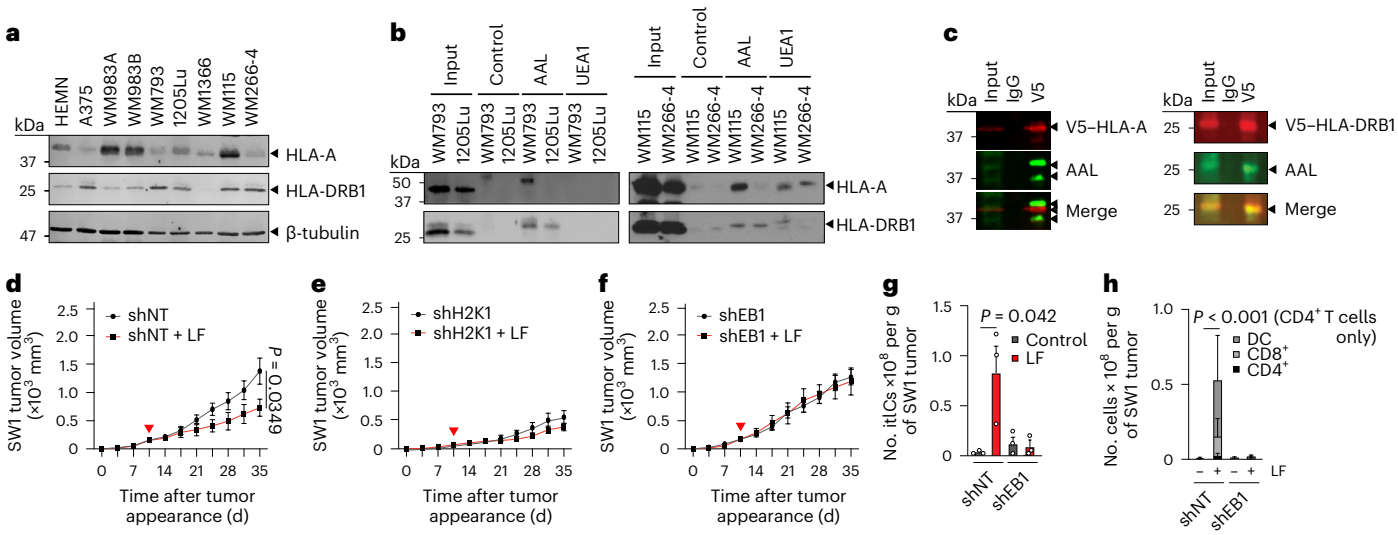

Fig. 3 | HLA-DRB1 is expressed, fucosylated and required for L-fuc-triggered melanoma suppression and increased itIC abundance. a, IB analysis of HLA-A and HLA-DRB1 levels in primary human melanocytes (HEMN) or the indicated human melanoma cell lines. **b**, LPD and IB analysis of patient-matched primary and metastatic cell line pairs WM793 and 1205Lu (left) and WM115 and WM266-4 (right) for HLA-A and HLA-DRB1. **c**, V5-immunoprecipitation and IB analyses of WM793 cells expressing (left) V5-tagged HLA-A or (right) V5-tagged HLA-DRB1. Volumetric growth curves for non-targeting control short hairpin RNA (shRNA) (shNT)- (**d**), H2K1-targeting shRNA (shH2K1)- (**e**) or H2EB1-targeting shRNA (shEB1)- (**f**) expressing SW1 tumors in C3H/HeN mice ($n = 8$ mice for each shNT group, $n = 6$ for each shH2K1 group and $n = 6$ and 7 for shEB1 and shEB1 with L-fuc groups, respectively). Flow cytometric comparison of total itIC counts (**g**) or the indicated subpopulations (**h**) from shNT- or shEB1-expressing tumors in **d**,**f**. $n = 3$ mice per group. For **d**–**f**, the red triangle indicates initiated L-fuc supplementation; growth curves and column charts show mean ± s.e.m. from each mouse group. In **a**–**c**, representative images are shown for $n = 3$ independent biological replicate experiments.

suppression, respectively[18–20] (Fig. 2a,c (orange dashed boxes) and Supplementary Table 1). Finally, L-fuc also transiently but significantly increased cytotoxic CD4⁺ T cells at the midpoint (day 28) of the experiment (Fig. 2d,e).

These data confirmed that CD4⁺ T cells play a key role in induction of itICs and suppression of melanomas by L-fuc, suggesting that L-fuc triggers key changes in CD4⁺ T cell signaling and biology at the tumor and lymph node levels that are important for tumor suppression. Importantly, the fact that mFuk expression alone in melanoma cells resulted in smaller tumors with increased itICs (Fig. 1e–h) suggests that melanoma-specific fucosylated protein(s) can also promote anti-tumor immunity, although the mechanism was unclear.

Fucosylated HLA-DRB1 induces itICs and melanoma suppression

To identify melanoma proteins that contributed to fucosylation-triggered, CD4⁺ T cell-mediated melanoma suppression, we subjected fucosylated proteins from human melanoma cells to liquid chromatography–mass spectrometric (LC–MS/MS) analysis followed by Ingenuity Pathway Analysis[21] (Extended Data Fig. 3a, left). These analyses identified 'Antigen presentation pathway' as the only immune-related pathway, in which the MHC-I and MHC-II proteins HLA-A and HLA-DRB1, respectively, were identified as the only antigen-presentation and plasma membrane proteins with T cell-modulating functions[22] (Extended Data Fig. 3a, right). We confirmed their expression in human melanocytes and melanoma cells by immunoblot (IB) analysis (Fig. 3a). Furthermore, lectin pulldown (LPD) using AAL and *Ulex europaeus* agglutinin I (UEA1) lectins, which bind to common core and terminal fucosylated glycans, respectively[23–28], revealed association of both proteins with AAL (and to a lesser extent, UEA1), suggesting *N*-linked core glycosylation–fucosylation (Fig. 3b). Finally, immunoprecipitation and IB analysis of V5-tagged HLA-A or HLA-DRB1 revealed direct recognition of HLA-DRB1 by AAL, indicating that a fraction of total HLA-DRB1 but not HLA-A is directly fucosylated in melanoma (Fig. 3c).

To determine contributions of HLA-A or HLA-DRB1 to fucosylation-triggered anti-tumor immunity, we knocked down their C3H/HeN mouse orthologs H2K1 or EB1 (ref. [29]), respectively, in SW1 tumors (Extended Data Fig. 3b) and assessed growth and itICs in vivo. Whereas L-fuc impaired control tumor growth, H2K1 knockdown suppressed tumor growth regardless of L-fuc (Fig. 3d,e), potentially reflecting tumor-protective, immunosuppressive roles of MHC-I proteins[30,31]. Notably, EB1 knockdown completely abolished L-fuc-triggered tumor suppression and induction of total itICs, including DC, CD8⁺ and CD4⁺ T cell subpopulations (Fig. 3f–h), similar to the effects elicited by CD4⁺ T cell depletion (Fig. 1l–o).

Consistent with roles of HLA-DRB1 in CD4⁺ T cell activation[32–34], our findings demonstrate that HLA-DRB1 is expressed and fucosylated in melanoma and required for L-fuc-triggered CD4⁺ T cell-mediated itIC induction and melanoma suppression.

Fucosylation regulates HLA-DRB1 localization and immunological effects

We reasoned that determining how HLA-DRB1 is regulated by fucosylation would provide important insight into its crucial role in L-fuc-triggered anti-tumor immunity. Using NetNGlyc version 1 and NetOGlyc version 4 (https://services.healthtech.dtu.dk)[35], we predicted *N*- and *O*-linked glycosylation sites at Asn48 (N48) and Thr129 (T129), respectively, which are conserved sites within constant regions of human and mouse HLA-DRB1 (Fig. 4a, top)[29,36]. Importantly, EB1 exhibits ~80% sequence homology with HLA-DRB1 and contains the conserved glycosylation–fucosylation site at N46 (ref. [29]). Modeling of HLA-DRB1 interactions with prominent binding partners HLA-DM or CD4–TCR suggests that fucosylation of neither site affects interaction interfaces or peptide loading or presentation (Fig. 4a, bottom).

Nano-LC–MS/MS analysis of HLA-DRB1 immunoprecipitated from WM793 cells identified the fragment FLEYSTSECHFFNGTER as glycosylated–fucosylated at N48 with the predicted glycan HexNAc(4) Hex(3)Fuc(1) (Fig. 4b and Extended Data Fig. 4a). We mutated N48 or

https://doi.org/10.1038/s43018-022-00506-7

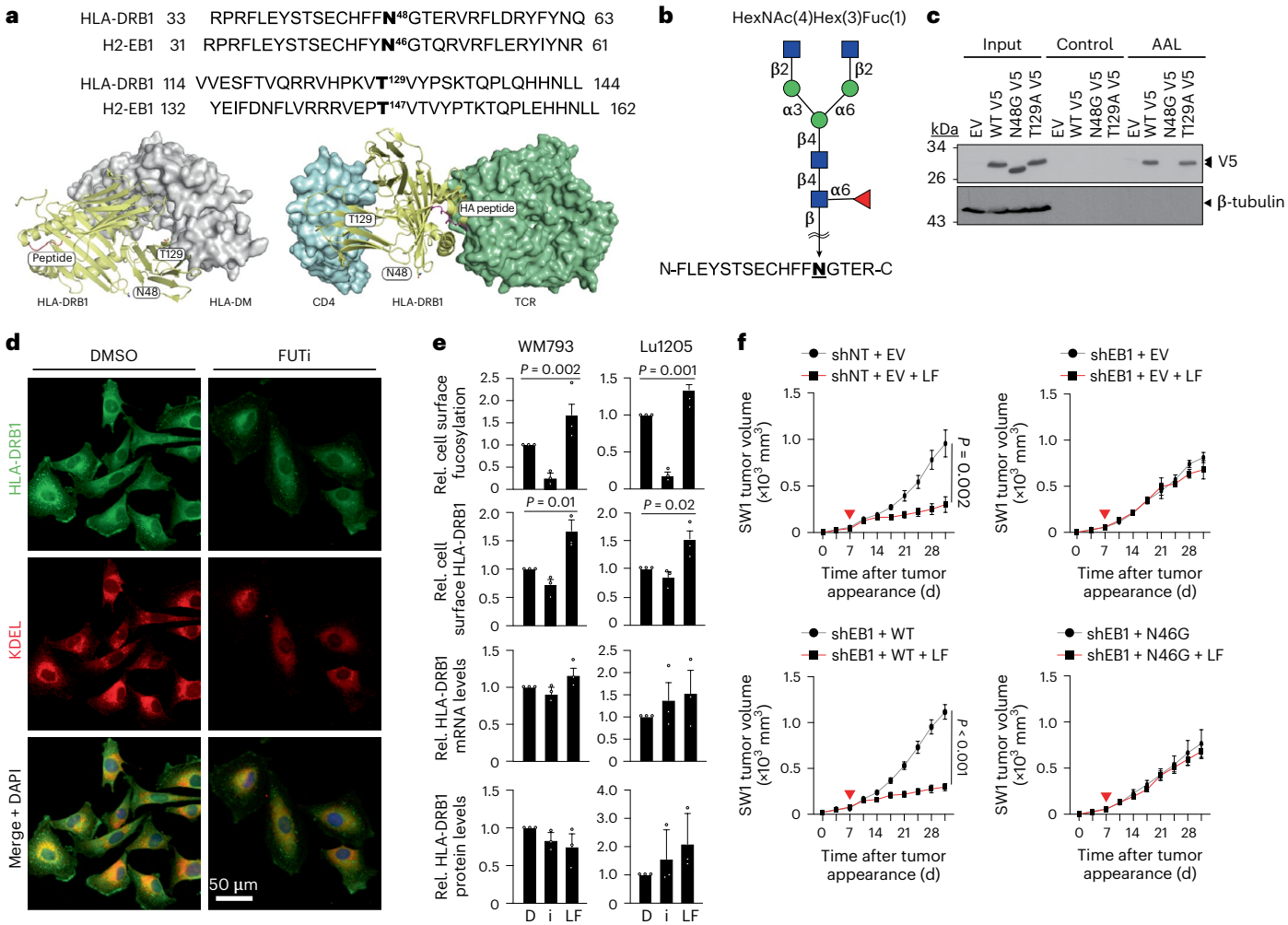

Fig. 4 | *N*-linked fucosylation of HLA-DRB1 at N48 regulates its cell surface localization and is required for tumor suppression and increased itIC abundance. a, Top, amino acid sequence alignments showing conservation of predicted *N*- and *O*-linked fucosylation sites in human HLA-DRB1 (N48 and T129) and mouse H2EB1 (N46 and T147). Structural modeling of the HLA-DRB1–HLA-DM (bottom left) and CD4–HLA-DRB1–TCR (bottom right) complexes. Potential glycosylation sites, N48 and T129, of the HLA-DR1 β-chain are shown as sticks. CD4 (cyan), HLA-DRB1 (yellow), antigen peptide (magenta) and TCR (green) (bottom right). **b**, The HLA-DRB1 peptide fragment was identified by nano-LC–MS to be fucosylated on N48, with the predicted HexNAc(4)Hex(3)Fuc(1) glycan structure shown above. **c**, LPD and IB analyses of EV and V5-tagged WT HLA-DRB1 (WT)-, HLA-DRB1^{N48G} (N48G)- and HLA-DRB1^{T129A} (T129A)-expressing WM793 cells. **d**, DMSO- or FUTi-treated WM793 cells immunofluorescently stained for endogenous HLA-DRB1 (green), KDEL (ER marker; red) and 4,6-diamidino-2-phenylindole (DAPI) (blue) (×20 magnification). **e**, Flow cytometric analysis for relative (rel.) cell surface fucosylation (top) and cell surface HLA-DRB1 (top middle), quantitative PCR with reverse transcription (RT–qPCR) analysis of relative HLA-DRB1 mRNA levels (bottom middle) and IB analysis of HLA-DRB1 protein levels (bottom) in WM793 and 1205Lu cells treated with DMSO (D), 250 μM FUTi (i) or 250 μM L-fuc. $n = 3$ biologically independent experiments. **f**, Volumetric growth curves for shNT and EV (control SW1 tumors) (top left) or shEB1 tumors reconstituted with EV (top right), EB1^{WT} (bottom left) or EB1^{N46G} (bottom right) in C3H/HeN mice. Control (gray) or L-fuc-supplemented water (red, 100 mM; red triangle, initiated supplementation) was provided ad libitum. Tumor growth curves show mean ± s.e.m. per mouse group. $n = 7$ mice per group except the shEB1 and EV group, which had six mice. For **c**,**d**, representative images are shown for $n = 3$ independent biological replicate experiments.

T129 to Gly or Ala, respectively, to abolish and verify fucosylation[37–39]. Unlike wild-type (WT) or the T129A 'glycofucomutant' HLA-DRB1, the HLA-DRB1^{N48G} glycofucomutant did not bind to AAL in LPD assays (Fig. 4c), confirming fucosylation at N48 on an N-linked glycan.

To determine how fucosylation might regulate HLA-DRB1, we assessed its subcellular localization in WM793 cells that were pharmacologically modulated for fucosylation by treatment with 2F-peracetyl-fucose (a FUT inhibitor (FUTi)[40]) versus vehicle (dimethylsulfoxide, DMSO; control). Cells treated with FUTi exhibited dimmer, more central, endoplasmic reticulum (ER)-colocalization of HLA-DRB1 than vehicle-treated cells, suggesting less accumulation at the cell surface (Fig. 4d). Furthermore, flow cytometry revealed that cell surface fucosylation and HLA-DRB1 both decreased or increased after FUTi or L-fuc treatments, respectively, whereas mRNA and protein levels remained unchanged; thus fucosylation promotes cell surface localization of HLA-DRB1 (Fig. 4e and Extended Data Fig. 4b). Finally, global proteomic profiling to identify interactors that might mediate fucosylation-regulated cell surface localization of HLA-DRB1 revealed that N48 glycosylation–fucosylation promotes binding to calnexin, which has been reported to mediate maturation and trafficking of MHC-II complexes to the surface[41] (Extended Data Fig. 5a–d).

To assess how HLA-DRB1 glycosylation–fucosylation contributes to tumor suppression and itICs, we compared control- or EB1-knocked-down SW1 tumors reconstituted with WT or glycofucomutant (N46G) EB1 (confirmation of knockdown reconstitution and fucosylation by IB and LPD, respectively, in Extended Data Fig. 5e).

Abrogation of L-fuc-induced itIC and tumor growth suppression by EB1 knockdown was rescued by reconstitution with only WT but not glycofucomutant EB1, demonstrating that glycosylation–fucosylation of EB1 or HLA-DRB1 is essential for L-fuc-triggered itIC induction and melanoma suppression (Fig. 4f and Extended Data Fig. 5f,g). This is consistent with our finding that loss of glycosylation–fucosylation of HLA-DRB1 or EB1 abrogates its cell surface localization and impairs its ability to induce anti-tumor immunity. Thus, despite the other fucosylated proteins identified in melanoma cells (Extended Data Fig. 3), these data confirm that the N48 glycosylation–fucosylation of HLA-DRB1 is a key regulator of anti-melanoma immunity and tumor suppression. Despite other potential host physiological effects of dietary L-fuc (for example, microbiome, metabolome, etc.), these data confirm that L-fuc-induced itIC increases and melanoma suppression are critically mediated by melanoma-intrinsic expression and fucosylation of HLA-DRB1, which promotes its cell surface accumulation to trigger $CD4^+$ T cell-mediated anti-tumor immune responses.

Oral L-fuc augments anti-PD1-mediated melanoma suppression

Expression of MHC-II reportedly correlates with increased anti-PD1 efficacy[42,43]. Indeed, patients who failed anti-PD1 therapy exhibited relative >45% reduced cell surface MHC-II but not MHC-I (Extended Data Fig. 5h). As anti-PD1 efficacy can be limited by itIC abundance[44], particularly of $CD4^+$ T and memory $CD4^+$ T cells[10,45–49], we tested whether the ability to increase $CD4^+$ T cell-mediated itIC induction and tumor suppression using oral L-fuc could be leveraged to augment anti-PD1 efficacy. In the SW1 model, oral L-fuc suppressed tumors as much as anti-PD1 but did not enhance efficacy of anti-PD1 therapy (~50–60%; Fig. 5a, left). By contrast, in the SM1 model, L-fuc was less tumor suppressive than anti-PD1 therapy alone but rather augmented durable suppression in combination with anti-PD1 therapy (Fig. 5a, right). Importantly, we also found that L-fuc does not alter cell surface levels of programmed cell death ligand 1 (PD-L1) in mouse or human melanoma cells (Extended Data Fig. 6a), suggesting that the L-fuc-associated tumor suppression in these models is attributed to determinants beyond the PD1–PD-L1 axis.

To clarify how the combination of L-fuc and anti-PD1 therapy enhanced suppression, we characterized immune cell profiles in the tumors and lymph nodes of SM1 tumor-bearing mice over a time course of treatment with L-fuc, with or without anti-PD1 therapy. Administration of L-fuc (1) alone increased intratumoral $CD4^+$ T central and effector memory cells, an effect that was increased when combined with anti-PD1 therapy (Fig. 5b (blue dashed boxes) and Supplementary Table 2) and (2) initially expanded intratumoral cDC2 cells, followed by later expansion of cDC2 cells and moDCs in the lymph nodes when combined with anti-PD1 therapy (Fig. 5b (orange dashed boxes) and Supplementary Table 2). In addition to expanding the absolute numbers of intratumoral $CD4^+$ and $CD8^+$ T cells at the endpoint (day 63), the combination of L-fuc and anti-PD1 therapy increased the relative percentage of intratumoral $CD8^+$ T central memory cells (Fig. 5b (green dashed box) and Supplementary Table 2). Thus, L-fuc can suppress some melanomas as effectively as anti-PD1 therapy, whereas, in others, it can enhance efficacy, which is associated with increased intratumoral $CD4^+$ T central and effector memory subpopulations and lymph node cDC2 and moDC populations, consistent with the effects of L-fuc observed in Fig. 2.

Clinical implications of tumor fucosylation and fucosylated HLA-DRB1

Given the potent enhancement of anti-PD1 efficacy by oral L-fuc administration in mice, we investigated whether tumor fucosylation or total/fucosylated HLA-DRB1 might correlate at all with responsiveness to anti-PD1 therapy in human patient biopsies, as the identification of preliminary correlations might support their subsequent development into predictive biomarkers for anti-PD1 responsiveness. To this end, we devised a new technique: we modified the conventional proximity ligation assay (PLA)[50] to facilitate immunofluorescent visualization of fucosylated HLA-DRB1 by applying anti-HLA-DRB1 antibody together with biotinylated AAL, which has previously been successfully used to stain tissues specifically for core-fucosylated glycans[51] (Fig. 6a). This technique, lectin-mediated PLA (L-PLA), revealed cytoplasmic and/or membranous localization of endogenous fucosylated HLA-DRB1 in melanoma cells (Fig. 6b) that is lost upon FUTi treatment (Fig. 6c), confirming L-fuc-stimulated cell surface localization of HLA-DRB1 (Fig. 4d,e and Extended Data Fig. 4b). The cytoplasmic and/or 'vesicular-appearing' staining is consistent with HLA-DRB1 that was fucosylated in the endoplasmic reticulum (ER)–Golgi and is en route to the surface via the secretory pathway. In applying this technique further to formalin-fixed, paraffin-embedded (FFPE) melanoma tissue specimens, we observed similar staining patterns for fucosylated HLA-DRB1 (Fig. 6d,e), which were completely abolished by washing the tissue with L-fuc, confirming specificity for fucosylated HLA-DRB1 (Fig. 6f).

To assess correlations of (1) tumor-specific fucosylation and total/fucosylated HLA-DRB1 of individual tumor cells and (2) intratumoral numbers $CD4^+$ T cells with responder status to single-agent anti-PD1 therapy, we implemented L-PLA on primary melanoma biopsies from two distinct responder and two non-responder patients followed by single-cell segmented signal quantitation (Fig. 7a,b). Tumors of responders clearly contained tumor cell populations with high levels of fucosylation and total HLA-DRB1 as compared to non-responders (Fig. 7b(i,ii)). Although the tumor of only one of two responders contained melanoma cells with increased levels of fucosylated HLA-DRB1 compared with those of the non-responders (Fig. 7b(iii)), this trend mirrored that of intratumoral $CD4^+$ T cell counts (Fig. 7b(iv)), consistent with the role for fucosylated HLA-DRB1 in $CD4^+$ T cell-mediated tumor suppression.

We assessed potential associations between tumor fucosylation, total/fucosylated HLA-DRB1, $CD4^+$ T cells and responder status in expanded cohorts of patients with melanoma treated with anti-PD1 therapy. Levels of tumor fucosylation and total and fucosylated

Fig. 5 | Administration of combination L-fuc and anti-PD1 therapy suppresses tumors and increases intratumoral $CD4^+$ T central and effector memory cells. a, Volumetric growth curves for SW1 tumors in C3H/HeN mice (left) and SM1 tumors in C57BL/6 mice (right) fed with or without L-fuc and treated with PBS (control) or anti-PD1 therapy (concurrent initiation of L-fuc with or without anti-PD1 therapy (red triangle)). The tumor growth curves show mean ± s.e.m. per mouse group. For each group, $n = 7$ mice except PBS with L-fuc and anti-PD1 therapy with L-fuc groups, which each have eight mice. **b**, Volumetric growth curves for SM1 tumors in C57BL/6 mice fed with or without L-fuc and treated with PBS (control) or anti-PD1 therapy (PD1) (concurrent initiation of L-fuc with or without anti-PD1 therapy (red triangle)). The tumor growth curves show mean ± s.e.m. from ≥7 mice per group. At day 7 (before administration of L-fuc or anti-PD1 therapy, $n = 3$ mice), day 21 (endpoint for tumors of control-treated mice, $n = 5$ mice per group), day 31 (endpoint for tumors of L-fuc-treated mice, $n = 5$ mice per group) and day 63 (endpoint for tumors of anti-PD1-treated mice, $n = 5$ mice per group), the primary tumors (tumor) and draining lymph nodes of 4–5 mice per treatment group were analyzed by flow cytometry for intratumor levels of $CD4^+$ and $CD8^+$ T subpopulations (naive or terminal; stem central, central or effector memory) and DC subpopulations (cDC1, cDC2 and moDC) as in Fig. 2. Proportions of $CD4^+$, $CD8^+$ and DC subpopulations in each organ at each time point are represented by the color-coded pie charts (each pie chart represents 4–5 mice). Absolute numbers of the subpopulations per 10^6 cells of tumor or tissue homogenate at each time point are represented in the color-coded column charts. Corresponding raw flow cytometric data for these charts are shown in Supplementary Table 2. Column charts show mean ± s.e.m. from each mouse group.

https://doi.org/10.1038/s43018-022-00506-7

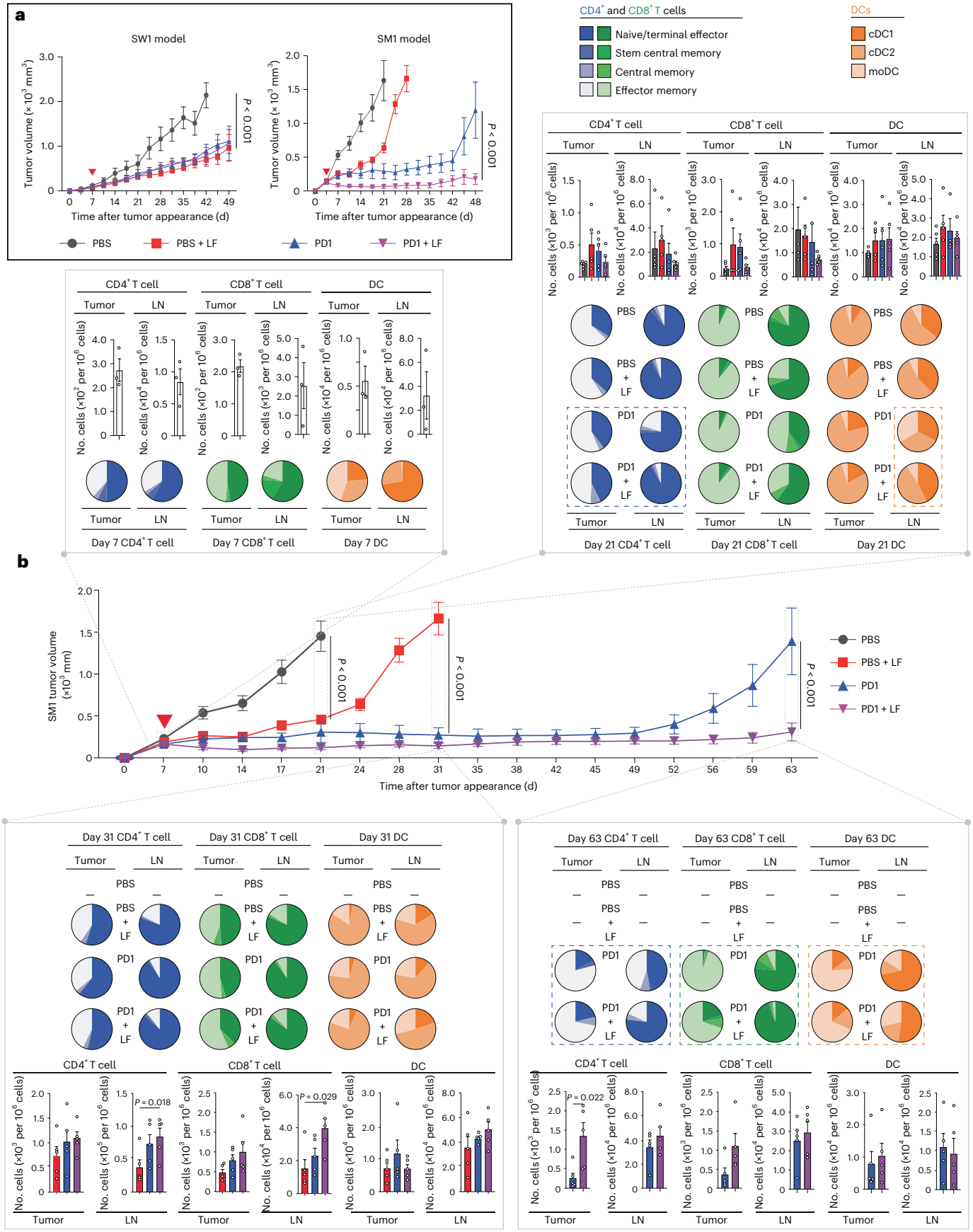

https://doi.org/10.1038/s43018-022-00506-7

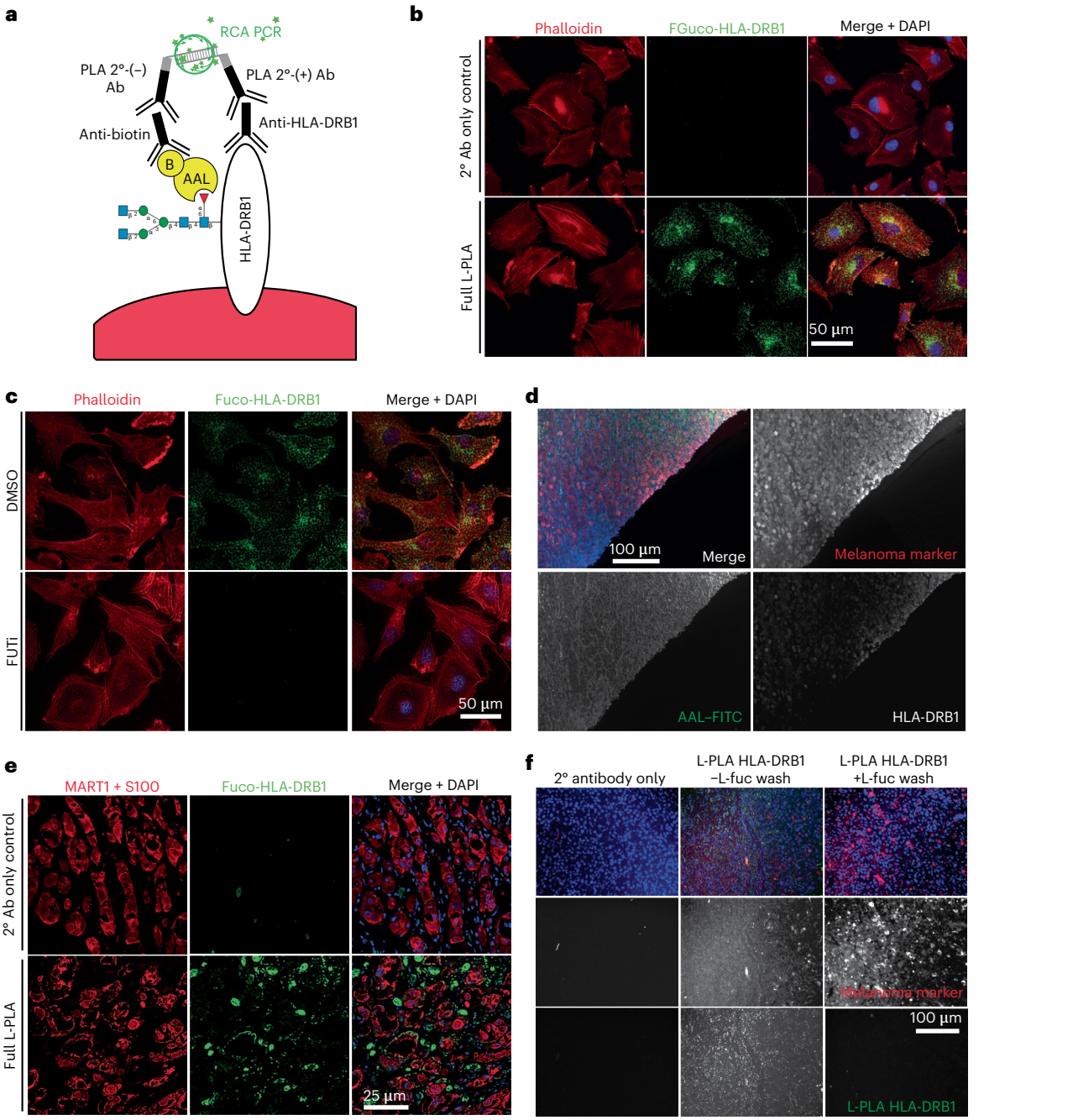

Fig. 6 | Immunofluorescent visualization of fucosylated HLA-DRB1: development of the lectin-mediated proximity ligation technique. a, Schematic of L-PLA using fucosylated HLA-DRB1 (fuco-HLA-DRB1) as an example. We stained for (1) HLA-DRB1 using anti-HLA-DRB1 antibody followed by oligonucleotide-conjugated PLA secondary antibody (2° Ab) (+) and (2) fucosylated glycan using biotinylated ('B') AAL lectin followed by anti-biotin antibody followed by oligonucleotide-conjugated PLA secondary (−). Ligated PLA oligonucleotides were subjected to rolling circle amplification PCR (RCA PCR), giving rise to fluorescent punctae. **b**, Representative images of secondary antibody-only control (top) or full L-PLA (bottom) staining of endogenous, fucosylated HLA-DRB1 (green) performed on coverslip-grown WM793 cells (with phalloidin (red) and DAPI (blue) co-stains). **c**, To further demonstrate that fucosylated HLA-DRB1 L-PLA staining is fucosylation species-specific, we performed L-PLA of endogenous, fucosylated HLA-DRB1 (green) on WM793 cells treated with DMSO or FUTi (phalloidin (red) and DAPI (blue) co-stains). **d**, To demonstrate specificity of individual L-PLA primary antibodies, FFPE melanoma tissue was stained for a melanoma marker (MART1 and S100 cocktail; red), AAL–FITC (green), HLA-DRB1 (white) and DAPI (blue). **e**, Representative images of secondary antibody-only control (top) or full L-PLA (bottom) staining of endogenous, fucosylated HLA-DRB1 (green) performed on human melanoma specimens (with MART1 and S100 (red) and DAPI (blue) co-stains). **f**, FFPE melanoma tissues were subjected to L-PLA HLA-DRB1 staining with or without washing with 500 mM L-fuc and subsequent staining with MART1 and S100 (red) and DAPI (blue). Total loss of fucosylated HLA-DRB1 (green) signal in tissue washed with L-fuc confirms the fucose-specificity of L-PLA for fucosylated HLA-DRB1. Single melanoma marker and fucosylated HLA-DRB1 channels are shown in white for clear visualization. For **b**–**f**, representative images are shown for $n = 3$ independent biological replicate experiments.

https://doi.org/10.1038/s43018-022-00506-7

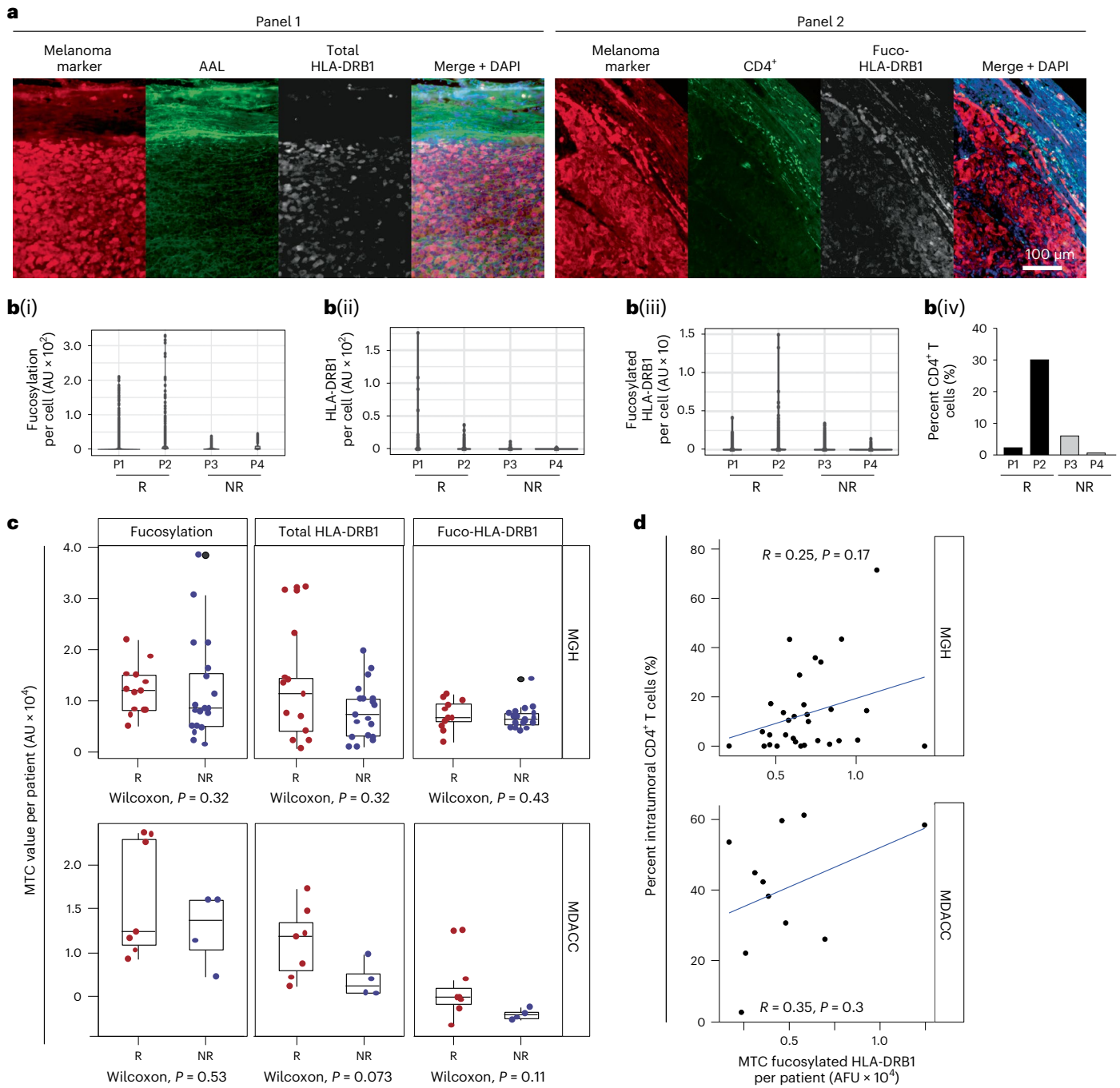

Fig. 7 | Clinical implications of melanoma fucosylation and fucosylated HLA-DRB1 for anti-PD1 therapy in melanoma. a, Representative images of one anti-PD1-treated Moffitt patient tumor subjected to immunofluorescent staining for the two indicated panels of markers. **b**, Dot plots showing single-cell distribution of total fucosylation (AAL) (i), total (ii) and fucosylated (iii) HLA-DRB1 staining intensities per melanoma cell and percent CD4$^+$ T cells (of total cells) within tumors of two responder (R; patients (P)1 and 2) and two non-responder (NR; patients 3 and 4) Moffitt patients (iv). AU, arbitrary units. **c**, Box plots showing mean tumor cellular (MTC; means derived from single tumor cell intensities) fucosylation (left), total (center) and fucosylated (right; fuco-HLA-DRB1) HLA-DRB1 staining intensities of anti-PD1 responder (red dots) and non-responder (blue dots) patients from MGH ($n = 32$) (top) or the MDACC ($n = 11$) (bottom). In all box plots, the middle line indicates the median, the lower and upper hinges represent the first and third quartiles and whiskers (from the hinges) extend to 1.5× the interquartile range (IQR). **d**, Percent intratumoral CD4$^+$ T cells (of total cells) plotted against corresponding average MTC fucosylated HLA-DRB1 values for each patient in the MGH (top) and MDACC (bottom) cohorts. *P* values shown are two-sided *P* values derived from the Spearman correlation test.

HLA-DRB1 in tumor cells were generally higher in anti-PD1 responders than in non-responders from Massachusetts General Hospital (MGH; $n = 31$; Fig. 7c, top) and the MD Anderson Cancer Center (MDACC; $n = 11$; Fig. 7c, bottom). Total tumor fucosylated HLA-DRB1 exhibited weak or no association with tumoral CD4$^+$ T cells (Fig. 7d, top and bottom), although the association was modestly increased when restricted to CD4$^+$ T cells localized at the periphery of the tumors (Extended Data Fig. 6b,c; absolute CD4$^+$ T numbers in Supplementary Table 3). Importantly, we found that some specimens containing divergent tumor–stroma content did exhibit divergent correlation strengths (for

example, core biopsies containing only tumor versus non-core biopsies containing substantial stroma). For example, a 'highly correlated' anti-PD1 responder (non-core biopsy) containing substantial tumor–stromal interface exhibited correlated high levels of fucosylated HLA-DRB1 and CD4$^+$ T cells, whereas a 'non-correlated' responder (a core biopsy) did not (Extended Data Fig. 6d), suggesting that variable stromal content within biopsies may have at least partially undermined the strength of the correlations that we assessed.

The lack of significant correlation may also be attributed to the dynamic relationship between fucosylated HLA-DRB1 and CD4$^+$ T cell infiltration that is further weakened by suboptimal inclusion criteria and/or patient stratification. Comparison of these markers in five patient-matched tumors before and after anti-PD1 therapy revealed no significant correlation in total HLA-DRB1 levels. However, before treatment, tumor cell fucosylation was significantly higher in the complete responder versus partial responders and non-responders; this dropped to the equivalently lower levels of the other patients after treatment. With the exception of one non-responder, the complete responder also exhibited significantly increased fucosylated HLA-DRB1 in tumor cells before treatment (Extended Data Fig. 6e). The consistent trends in tumor fucosylation and fucosylated tumor HLA-DRB1 observed across the three independent cancer center cohorts appear to support potential utility but importantly point to the need for further study in expanded patient pre-treatment biopsy cohorts that are controlled for a number of specific clinical variables, which will be discussed below.

Discussion

Here, we report the administration of a dietary sugar as a way to increase itICs and enhance efficacy of the immune checkpoint blockade anti-PD1 agent. These studies reveal insights into the post-translational regulation and immunological roles of melanoma cell-expressed MHC-II proteins, further highlighting their relationship with itICs[42,43,45–49]. Specifically, fucosylation regulates the cell surface abundance of HLA-DRB1, which triggers robust CD4$^+$ T cell-mediated itIC induction and melanoma suppression. It is important to acknowledge that our reliance on AAL lectin predominantly focuses our study on α1,6-fucosylated proteins. Although this does not diminish the crucial role that α1,6-fucosylated HLA-DRB1, which was identified as fucosylated via lectin-agnostic click chemistry mass spectrometric screening, plays in L-fuc-triggered anti-tumor immune responses, it is possible that proteins with other fucosylation linkages might contribute to aspects of anti-tumor immunity. It is also likely that the statistical strength of our analyses of tumor fucosylation with patient outcomes (Fig. 7) was limited by use of only AAL lectin, which precludes the detection of other structural forms of fucosylation. Nonetheless, the ability to leverage this mechanism using oral L-fuc administration may help to enhance other immunotherapeutic modalities (that is, other checkpoint inhibitors or adoptive cell-transfer therapies). Notably, as a non-toxic dietary sugar with a past safety precedent as an experimental therapy for children with leukocyte adhesion deficiency II[52,53], L-fuc appears to be a potentially safe and tolerable therapeutic agent.

The consistent trends that we observed in higher tumor fucosylation and fucosylated HLA-DRB1 across anti-PD1 responders versus non-responders between the three independent cancer center cohorts support their potential utility as biomarkers of anti-PD1 responsiveness. However, further analyses in expanded patient biopsy cohorts are clearly needed. Considering the variable tumor-suppressive effects of L-fuc observed in our anti-PD1-treated SM1 and SM1 mouse models, there are likely similar biological and clinical variables in patients that must be further explored and that may have precluded statistical significance in our small analyses.

In terms of biological variables, how T cell biology is regulated by fucosylation, for example, has heretofore been unclear. Reported divergent effects of fucosylation on T cell activation versus exhaustion (that is, via regulation of PD-L1 expression) point to FUT-specific expression and roles that remain to be elucidated[54–56]. The fact that L-fuc does not alter the cell surface levels of PD-L1 in human or mouse melanoma cells (Extended Data Fig. 6a), suggesting that the discrepant tumor suppression by single-agent versus combination L-fuc and anti-PD1 therapy in our SW1 and SM1 mouse models (Fig. 5a), is attributed to determinants beyond the PD1–PD-L1 axis. Indeed, our global fucosylated and phosphoproteomic analyses suggest that fucosylation in CD4$^+$ T cells impacts integrin β5, PKA and actin signaling (Extended Data Fig. 2) and that this is associated with increased intratumoral T cell presence and memory phenotypes in our models (Figs. 2 and 5), consistent with previous reports that those functions are regulated by those pathways in T cell biology[15–17,57]. The fact that L-fuc can increase CD4$^+$ T central memory cells also partially explains how it can augment anti-PD1 efficacy, which is associated with the presence of these cells[10]. How L-fuc may regulate these signaling pathways and enrich for CD4$^+$ T memory subsets within the tumor microenvironment and, furthermore, how L-fuc alters DC biology and induces their intratumoral accumulation (Figs. 2 and 5) may contribute to anti-tumor immune responses and tumor suppression in this context are unclear and warrant further lines of study. In addition, sex might be a determinant, as melanoma fucosylation levels are lower but correlate more strongly with intratumoral CD3$^+$ T cells in male versus female patients (Fig. 1j,k). Reduced melanoma fucosylation, which is expected to lower itICs, might explain increased lethality in male patients (American Cancer Society Facts and Figures, 2022).

The availability of pre-treatment anti-PD1 tumor tissue specimens for this study was extremely limited. Thus, the specimens that we acquired were subject to clinical variability that may have undermined statistical robustness in our analyses. Subsequent studies investigating tumor fucosylation, total/fucosylated HLA-DRB1 and CD4$^+$ T cells as biomarkers will need to factor for clinical variables including therapies received before anti-PD1 therapy and pre-existing medical conditions as well as time from biopsy to anti-PD1 treatment. Because we were unable to control for these confounders in our specimens, it is unclear how they may have impacted tumor and HLA-DRB1 fucosylation and CD4$^+$ T cell biology and thus the strength of correlations between these markers and responsiveness to treatment. Likewise, the importance and contribution of the immune environment of the peri-tumoral stroma in this setting remains to be elucidated, as some of our biopsies contained stroma, whereas other tumor core biopsies did not. Prior studies focusing on tumor–immune interactions and immunotherapies (including anti-PD1 therapy) have highlighted the importance of analyzing biomarker staining patterns at tumor–immune and tumor–stromal interfaces contained within biopsies, as these are areas of enriched immunological activity and signaling[58–60]. Indeed, our observation of 'highly correlated' and 'non-correlated' anti-PD1 responder biopsies containing disparate amounts of tumor stroma highlight how lack of sufficient stroma in tumor biopsies likely undermined the statistical robustness of the correlations between fucosylated HLA-DRB1 and CD4$^+$ T cells (Extended Data Fig. 6d). The acquisition of such biopsy specimens that are controlled for the variables detailed above is an important consideration for subsequent studies. Our findings highlight the need for a prospective clinical trial with defined protocols for collection of monotherapy anti-PD1 pre-treatment biopsies at defined time points proximal to therapy and clear biopsy protocols to yield tumor specimens that contain substantial intact stromal interface.

In conclusion, fucosylation of HLA-DRB1 is a key regulator of itIC abundance in melanomas, and this mechanism, together with fucosylation-regulated CD4$^+$ T cell biology, can be therapeutically exploited using oral L-fuc administration. Elucidation of the mechanistic determinants is expected to advance our understanding of the immunobiology of melanoma and other cancers and to inform efforts in implementing fucosylation and/or fucosylated HLA-DRB1 as biomarkers and of L-fuc as a therapeutic agent.

Methods

Our research complies with all relevant ethical regulations: all animal experiments were approved by the Moffitt IACUC committee. All patient specimen-staining analyses are considered as IRB exempt: investigators were blinded from all patient health information, and the specimens were previously collected under IRB-approved protocols per respective institutional IRB committees. All cell line and antibody information is provided in the Nature Portfolio Reporting Summary.

General cell culture

The following cell lines were from the American Tissue Type Collection: A375, HEMN (normal adult epidermal melanocytes) and Jurkat. The following cell lines were from Rockland Immunochemicals: WM983A, WM983B, WM1366, WM115, WM266-4, WM164, WM793 and Lu1205. SW1 melanoma cells (gift from the Ronai laboratory at the Sanford Burnham Prebys Medical Discovery Institute) and SM1 melanoma cells (gift from the Smalley laboratory at the Moffitt Cancer Center) were cultured in DMEM containing 10% FBS, 1 g ml^{-1} glucose and 4 mM L-glutamine at 37 °C with 5% CO_2. HEMN cells were grown in Lonza MGM-4 growth medium; before collection for IB analysis, the cells were switched to the same medium as the other cells overnight. Cell lines were transfected using Lipofectamine 2000 (Invitrogen). Primary $CD4^+$ T cells were collected using the EasySep Human $CD4^+$ negative selection isolation kit (Stemcell Technologies) according to the manufacturer's protocols. Upon arrival at the laboratory, all cell lines are quarantined until they have passed footprint identification and mycoplasma testing (as mycoplasma negative). The identities of all cell lines (human and mouse) in the Lau laboratory are verified annually by short tandem repeat-based authentication 'CellCheck' services provided through IDEXX BioResearch.

Cloning and mutagenesis

The gene encoding mFuk was cloned using cDNA from SW1 cells into the pLenti-C-Myc-DDK-IRES-Puro expression vector (OriGene Technologies) using BamHI and NheI restriction sites. Mouse EB1 constructs were cloned using cDNA from SW1 cells into the pLenti-C-Myc-DDK-IRES-Puro expression vector (OriGene Technologies) using AscI and XhoI restriction sites. pLKO shNT, pLKO shK1-1, pLKO shK1-2, pLKO shEB1-1 and pLKO shEB1-2 were obtained from MilliporeSigma. pLX304::EV was obtained from OriGene Technologies. pLX304::HLA-A and pLX304::HLA-DRB1 constructs were obtained from DNAasu[61]. HLA-$DRB1^{N48G}$ and HLA-$DRB1^{T129A}$ as well as $EB1^{N46G}$ mutants were generated using the QuikChange II XL site-directed mutagenesis kit according to the manufacturer's protocol (Agilent Technologies).

Lectin pulldown

Control beads and AAL or UEA1 lectin-conjugated agarose beads were pre-blocked for 2 h in blocking buffer (2% IgG-free BSA (Jackson ImmunoResearch Laboratories)) on a rotator at 4 °C. Cells were lysed on ice in 1% Triton X-100 lysis buffer (1% Triton X-100, 20 mM Tris-HCl, pH 7.4, 150 mM NaCl in ddH_2O with protease and phosphatase inhibitors (Thermo Fisher Scientific)), briefly sonicated and pelleted. The resulting lysates were normalized in protein concentration to the sample with the lowest concentration, diluted to a final concentration of 0.25% Triton X-100 with dilution buffer (0% Triton X-100, 20 mM Tris-HCl, pH 7.4, 150 mM NaCl in ddH_2O with protease and phosphatase inhibitors), incubated with 15 µl pre-blocked beads (beads were centrifuged out of a block and resuspended in dilution buffer) and rotated overnight at 4 °C. Next, the beads were washed twice with dilution buffer and subjected to (12%) SDS–PAGE and IB analysis using the indicated antibodies.

Mass spectrometric analyses

Profiling fucosylated proteins. EV-, pLenti-FUK-GFP- or shFUK-expressing WM793 cells were cultured in biological triplicate in the presence of 50 µM L-fuc-alkyne for ~72 h to ~80% confluence. Cells were lysed in 1.5% *N*-dodecyl-β-D-maltoside, 20 mM HEPES, pH 7.4, and protease and phosphatase inhibitors. Lysates were precipitated with acetone overnight, and pelleted proteins were resuspended and subjected to click chemistry labeling with biotin–azide using the Click-iT kit according to the manufacturer's protocol (Invitrogen). The negative control included EV cells not labeled with L-fuc-alkyne. All biotinylated–fucosylated samples were pulled down using neutravidin beads (pre-blocked with 2% IgG-free BSA). Samples were submitted to the Sanford Burnham Prebys proteomics core facility for on-bead digestion and LC–MS/MS analysis. Hits that were increased by >1.5 fold in pLenti-FUK-GFP-expressing cells and unchanged or decreased in pLenti-EV-GFP-expressing cells or decreased in pLenti-shFUK-expressing cells were subjected to Ingenuity Pathway Analysis (Qiagen).

Profiling HLA-DRB1 glycosylation–fucosylation. Stained bands (~1 µg) of exogenously expressed V5–HLA-DRB1 purified from WM793 cells were minced, reduced and alkylated using 20 mM TCEP (Tris(2-carboxyethyl)phosphine) and iodoacetamide in 50 mM Tris-HCl. Gel pieces were washed with 20 mM ammonium phosphate in 50% methanol overnight at 4 °C, followed by dehydrating for 30 min with 100% acetonitrile. Samples were next digested with trypsin for 4 h at 37 °C and eluted through C_{18} ZipTips with 50% methanol and 0.1% formic acid (FA). Five microliters of the elution were diluted in 0.1% FA and injected into a Q Exactive Orbitrap mass spectrometer equipped with an Easy Nano-LC HPLC system and a reverse-phase column (Thermo Fisher Scientific). A binary gradient solvent system consisting of 0.1% FA in water (solvent A) and 90% acetonitrile with 0.1% FA in water (solvent B) was used to separate peptides. Raw data were analyzed using both Proteome Discoverer version 2.1 (Thermo Fisher Scientific) with the Byonic (Protein Metrics) module and Byonic standalone version 2.10.5. All extracted ion chromatograms were generated using Xcalibur Qual Browser version 4.0 (Thermo Fisher Scientific). The UniProt sequence Q5Y7D1_Human was used as the reference sequence for peptide analysis.

Phosphoproteomic profiling of $CD4^{\pm}$ T cells. The indicated $CD4^+$ T cells were lysed in RIPA buffer with protease and phosphatase inhibitors. Briefly, ~1 mg of each lysate was reduced with 4.5 mM dithiothreitol for 30 min at 60 °C, alkylated with 10 mM iodoacetamide at room temperature in the dark for 20 min and digested overnight at 37 °C with an enzyme-to-protein ratio of trypsin of 1:20 (Worthington). Resulting peptides were desalted using a reversed-phase Sep-Pak C_{18} cartridge (Waters) and lyophilized for 48 h. Lyophilized peptides were enriched for global phosphopeptides (pSTY) using IMAC Fe-NTA magnetic beads (Cell Signaling Technology) on a KingFisher Flex Purification System (Thermo Fisher Scientific), followed by SpeedVac concentration and resuspension in loading buffer (5% ACN and 0.1% TFA) before auto-sampling and LC–MS/MS as described below.

Fucoproteomic profiling of $CD4^{\pm}$ T cells. The indicated $CD4^+$ T cells were lysed in RIPA buffer with protease and phosphatase inhibitors and subjected to LPD using control or AAL beads. The beads were washed with PBS and subjected to on-bead trypsin digestion. Resulting peptides were further denatured with 30 mM ammonium bicarbonate at 95 °C for 5 min and then acidified with TFA at a final concentration of 1%. ZipTip-purified, eluted peptides were concentrated with a SpeedVac and resuspended in loading buffer (5% ACN and 0.1% TFA) before auto-sampling and LC–MS/MS as described below.

Profiling HLA-DRB1 interactors. V5-tagged WT or N48G glycofucomutant HLA-DRB1-expressing WM793 cells were lysed and subjected to V5 bead pulldown. Five percent of pulled down protein was immunoblotted to ensure equal sample submission for processing as described above and LC–MS/MS as described below.

Liquid chromatography–mass spectrometry

Tryptic peptides were analyzed using a nanoflow ultra-high-performance liquid chromatograph and an electrospray Orbitrap mass spectrometer (RSLCnano and Q Exactive Plus, Thermo) for tandem MS peptide sequencing. Peptide mixtures were loaded onto a pre-column (100-µm ID × 2-cm column packed with C_{18} reversed-phase resin; particle size, 5 µm; pore size, 100 Å) and washed for 5 min with aqueous 2% acetonitrile and 0.1% FA. Solvent A comprised 98% ddH_2O, 2% acetonitrile and 0.1% FA, and solvent B comprised 90% acetonitrile, 10% ddH_2O and 0.1% FA. Trapped peptides were eluted or separated on a C_{18} analytical column (75-µm ID × 50 cm; particle size, 2 µm; pore size, 100 Å; Thermo Fisher Scientific) using a 90-min gradient at a flow rate of 300 nl min^{-1} of 2% to 3% solvent B over 5 min, 3% to 30% solvent B over 27 min, 30% to 38.5% solvent B over 5 min, 38.5% to 90% solvent B over 3 min and then held at 90% for 3 min, followed by 90% to 2% solvent B in 1 min and re-equilibrated for 18 min. MS resolution was set at 70,000, and MS/MS resolution was set at 17,500 with a maximum IT of 50 ms. The top 16 tandem mass spectra were collected using data-dependent acquisition following each survey scan and 60-s exclusion for previously sampled peptide peaks. For phosphoproteomic, fucoproteomic and HLA-DRB1 WT and glycofucomutant interactor profiling, MaxQuant[62] software (version 1.6.2.10) was used to identify and/or quantify phosphopeptides and proteins for the data-dependent acquisition runs. The false discovery rate was set to 1%.

PyMOL structural modeling

In Fig. 4a, structural modeling was performed using PyMOL (Molecular Graphics System, version 2.0, Schrödinger) of the HLA-DRB1–HLA-DM complex (PDB ID 4FQX), HLA-DRB1 (yellow) and DM (gray). For the CD4–HLA-DRB1–TCR complex, the model was reconstituted by superimposing the DRB1 β-chains from the CD4–HLA-DR1 complex (PDB ID 3S5L) and the TCR–HLA-DR1 complex (PDB ID 6CQR) using PyMOL. RMSD between the 163 backbone atoms is 0.497. The potential glycosylation sites N48 and T129 of the HLA-DR1 β-chain are shown as sticks. The color scheme is CD4 (cyan), HLA-DRB1 (yellow), antigen peptide (magenta) and TCR (green).

Tumor-infiltrating lymphocyte-isolation protocol

Tumors of SW1 or SM1 melanoma cells from C3H/HeJ or C57BL/6 mice, respectively, were digested using 1× tumor digest buffer (0.5 mg ml^{-1} collagenase I, 0.5 mg ml^{-1} collagenase IV, 0.25 mg ml^{-1} hyaluronidase V, 0.1 mg ml^{-1} DNase I in HBSS (MilliporeSigma)) and homogenized using a Miltenyi MACS dissociator. Red blood cells were lysed using ACK lysis buffer (Life Technologies). Tumor homogenate cells were counted using a standard hemocytometer.

Human donor peripheral CD4± T cell-isolation protocol

Human $CD4^+$ T cells were (1) isolated from fresh PBMCs using a $CD4^+$ T cell negative selection isolation kit (Stemcell Technologies) according to manufacturer's protocols, (2) cultured in the presence of vehicle or 250 µM L-fuc and (3) activated using anti-CD3/CD28 Dynabeads (Thermo Fisher Scientific) at a bead:$CD4^+$ T cell ratio of 1:1. After 48 h, cell pellets were collected and lysed for fucoproteomic or phosphoproteomic profiling.

Flow cytometry

Gating schemes are provided in the Supplementary Information. Unless otherwise indicated, cytometry was performed using an LSR Flow Cytometer (BD Biosciences), and analysis was performed using FACSDiva version 9, CellQuest version 6 and FlowJo version 9 software (BD Biosciences).

Intratumoral immune cell and splenic profiling. Total itICs were gated first to single cells as described in Supplementary Fig. 1. Single-cell suspensions from tumor and spleen tissue were stained with Live/Dead Zombie NIR (BioLegend) at 1:1,000 in PBS for 20 min. Cell suspensions were centrifuged and stained with the following with antibodies at 0.5 µg ml^{-1} per antibody: APC anti-mouse CD3, Pacific Blue anti-mouse CD4, BV785 anti-mouse CD8, PerCP anti-mouse CD25, FITC anti-mouse F4/80, Pe-Cy7 anti-mouse CD11c, PE anti-mouse NK1.1 or PE anti-mouse DX5 and PerCP-Cy5.5 anti-mouse CD11b. Compensation controls were prepared using 0.5 µg ml^{-1} of each antibody with UltraComp eBeads (Thermo Fisher Scientific). After staining, cells were washed, fixed (2% formaldehyde), washed and subjected to flow cytometric analysis. Dendritic and $CD4^+$ T cell subpopulations were subjected to staining and flow cytometric analyses as in Supplementary Figs. 2 and 3.

Assessment of cell surface fucosylation, HLA-DRB1 and PD-L1. The indicated cells were treated for 72 h with DMSO, 250 µM FUTi (MilliporeSigma) or 250 µM L-fuc (Biosynth), followed by staining with 0.1 µM PKH26 (MilliporeSigma) before fixation in 4% formaldehyde solution. Cells were stained with anti-HLA-DRB1 antibody and fluorescein AAL or anti-human or anti-mouse PD-L1 antibodies overnight, followed by three washes and staining with Alexa Fluor 594 donkey anti-rabbit antibody. Cells were washed and subjected to flow cytometric analyses using a FACSCalibur (BD Biosciences) as in Supplementary Fig. 4.

Assessment of cell surface pan-MHC-I and pan-MHC-II. Surgically resected patient tumors were minced to fragments less than 1 mm and digested in 1× tumor digest buffer. Single-cell suspensions were strained through 40-µm nylon mesh and counted for viability by trypan blue exclusion. Strained tumor homogenates were stained using Live/Dead Zombie NIR, PE anti-pan-MHC-I (HLA-A–HLA-C), FITC anti-pan-MHC-II, PerPCy5.5 anti-CD45, APC anti-CD90 and BV421 anti-EpCAM antibodies and subjected to flow cytometric analysis as in Supplementary Fig. 5.

Immunoblot analyses

Cells were lysed on ice in standard RIPA buffer (25 mM Tris-HCl, pH 7.6, 150 mM NaCl, 5 mM EDTA, 1% NP-40 or 1% Triton X-100, 1% sodium deoxycholate, 0.1% SDS in diH_2O with protease and phosphatase inhibitors), sonicated and pelleted, and the resulting lysates were normalized by protein concentration using the DC assay (Bio-Rad Laboratories). Lysates were subjected to (12%) SDS–PAGE and IB using the indicated antibodies. IB imaging and analysis was performed using either an Odyssey FC scanner and Image Studio (LI-COR Biosciences) or film.

Quantitative PCR with reverse transcription

RNA from the indicated cells was extracted using the GenElute Mammalian Total RNA extraction system (MilliporeSigma) and reversed transcribed using the High-Capacity cDNA Reverse Transcription Kit (Thermo Fisher Scientific). RT–qPCR was performed using FastStart Universal SYBR Green Master Mix (Rox) (Roche Diagnostics) using CFX Manager version 3.1 on a Bio-Rad CFX96 Real-Time system (Bio-Rad Laboratories). RT–qPCR cycles were as follows: 95 °C for 10 min, 35 cycles of 95 °C for 15 s, 55 °C for 60 s and 72 °C for 30 s. Gene expression was normalized to histone H3A expression. Primers for RT–qPCR were generated using NCBI Primer BLAST software (National Center for Biotechnology Information). Oligonucleotide sequences are provided in Supplementary Table 4.

Fluorescent immunocytochemical and immunohistological staining and analysis

General immunofluorescent cell staining. Cells were grown on German glass coverslips (Electron Microscopy Services) and fixed in fixation buffer (4% formaldehyde, 2% sucrose in PBS) for 20 min at room temperature. Cells were washed with PBS, permeabilized in permeabilization buffer (0.4% Triton X-100 and 0.4% IgG-free BSA

(Jackson ImmunoResearch Laboratories) in PBS for 20 min at room temperature, washed with PBS again and incubated with the indicated antibodies. Unless otherwise indicated, images were acquired using a Keyence BZ-X710 microscope and processed and analyzed using ImageJ version 1.53a (NIH).

General immunofluorescent tissue staining. FFPE tumor sections (or tumor microarray (TMA) slides) were melted at 70 °C for 30 min, de-paraffinized using xylene and rehydrated in serial alcohol washes. The slides were pressure cooked at 15 psi for 15 min in 1× DAKO antigen-retrieval buffer (Agilent Technologies). Slides were subjected to two 5-min standing washes in PBS before blocking in 1× Carbo-Free Blocking Solution (Vector Laboratories) for 2–3 h, followed by two more washes and staining with the indicated lectin and/or antibodies before washing and mounting with VECTASHIELD and DAPI (Vector Laboratories).

Mouse tumor fucosylation analysis. For Extended Data Fig. 1a,d,k, tumors were immunostained with FITC-conjugated AAL lectin (0.4 µg ml^{-1}) and rabbit anti-MART1 and rabbit anti-S100 antibodies. Images were acquired using a Keyence BZ-X710 microscope, and images were processed and analyzed using ImageJ version 1.53a (NIH) as follows: melanoma marker-positive regions were assigned as regions of interest in which we measured the integrated density of the AAL signal. Integrated densities of control tumors were assigned as 1, and integrated AAL density values of experimental tumors were divided by control values to produce relative fold changes and plotted as column charts.

Melanoma TMA analysis. For Fig. 1i–k, melanoma TMA (ME1002b; US Biomax; 18 female and 22 male patients, ages 25–88 years, stages 1A–4, cutaneous and mucosal tumors) was immunostained with FITC-conjugated AAL lectin (0.4 µg ml^{-1}), rabbit anti-MART1, rabbit anti-S100 and anti-CD3 antibodies, followed by Alexa Fluor 568 (Cy3) donkey anti-rabbit and Alexa Fluor 647 (Cy5) donkey anti-mouse secondary antibodies. Slides were mounted with VECTASHIELD and DAPI. An Aperio ScanScope FL scanner (Leica Biosystems) was used to scan the TMA at 20×. Definiens Tissue Studio version 4.7 (Definiens) was used to identify individual cores followed by single-cell segmentation. Mean fluorescence intensity (MFI) values for fucosylation, melanoma markers and CD3 channels were extracted from each segmented cell; minimum MFI thresholds were set to enumerate melanoma and CD3$^+$ T cells. Average MFI values for each core were reported for fucosylation and melanoma marker channels.

We used nonparametric Wilcoxon rank-sum test to compare melanoma-specific fucosylation levels between CD3$^+$ T cell high versus low groups. Density values of CD3$^+$ T cells were all $\log_2$ transformed in the statistical analysis. Multivariable linear regression was used to assess association between fucosylation and T cells while adjusting for confounding factors including sex, age and stage. The Spearman correlation coefficient was used to measure the correlation between melanoma-specific fucosylation and T cells in different sex groups.

Lectin-mediated proximity ligation assay. Coverslip-grown cells or FFPE tumor sections subjected to L-PLA were processed upfront as described above. Both approaches used mouse anti-HLA-DRB1 antibody (0.2 µg ml^{-1}) and biotinylated AAL lectin (0.2 µg ml^{-1}), staining overnight at 4 °C. Coverslips and/or slides were washed twice with PBS and incubated with phalloidin Alexa Fluor 488 with goat anti-biotin antibody for 2 h at 4 °C. Subsequent steps of the protocol were adapted from the Duolink In Situ Green PLA kit's manufacturer's protocol (MilliporeSigma). PLA anti-goat MINUS and PLA anti-mouse PLUS probes were applied at 1:5 for 1 h at 37 °C. The coverslips and/or slides were washed twice with wash buffer A before ligation with 1:5 ligation buffer and 1:40 ligase in ddH_2O for 30 min at 37 °C. Coverslips and/or slides were washed twice with wash buffer A before incubation in amplification mix (1:5 amplification buffer and 1:80 polymerase in ddH_2O for 1.5 h at 37 °C). Coverslips and/or slides were washed twice with wash buffer B before mounting with VECTASHIELD and DAPI.

Immunofluorescent staining and analysis of anti-PD1-treated patients with melanoma. For Fig. 5c, the indicated FFPE sections were immunostained with anti-HLA-DRB1 antibody or by L-PLA as detailed above with the addition of anti-CD4 antibody. WTS imaging was performed using the Vectra 3 Automated Quantitative Pathology Imaging System (PerkinElmer). Tiles (20× region of interest) were sequentially scanned across the slide and spectrally unmixed using inForm (PerkinElmer). HALO (Indica Labs) was used to fuse tile images together. For each whole-tumor image, (1) every individual melanoma marker (MART1 and S100)-positive cell was segmented and quantitatively measured for total fucosylation and total and fucosylated HLA-DRB1, and (2) every CD4$^+$ T cell within the melanoma marker-positive tissue region and melanoma marker-negative periphery was counted. For each patient, marker values were displayed in box plots to visualize staining distribution of individual tumor cells. The total numbers of melanoma cells per patient section measured and analyzed were as follows: patient 1, 557,146 cells; patient 2, 743,172 cells; patient 3, 95,628 cells; and patient 4, 13,423 cells.

Anti-PD1-treated patient specimens

Moffitt Cancer Center patient specimens. For Fig. 5d,e and Extended Data Fig. 4d,e, de-identified specimens from MCC patients with advanced stage melanoma were collected and analyzed following patient consent under MCC Institutional Review Board (IRB)-approved protocols:

For Fig. 7b, 'responder' patients exhibited >20 months of progression-free survival, whereas 'non-responder' patients progressed after <6 months after receiving anti-PD1 therapy.

For Extended Data Fig. 5h, non-response status to PD1 checkpoint blockade (nivolumab or pembrolizumab) was defined by RECIST 1.1 as disease progression on therapy or within 3 months of the last dose.

University of Texas MD Anderson Cancer Center patient specimens. Biospecimens were retrieved, collected and analyzed after patient consent under University of Texas MDACC IRB-approved protocols. University of Texas MDACC patients with advanced (stages III–IV) melanoma between 1 July 2015 and 1 May 2020 who received >1 dose of PD1 checkpoint blockade agent (nivolumab or pembrolizumab) were identified from detailed review of clinic records. Responders or non-responders were defined as those with a complete or partial response or stable or progressive disease, respectively, by RECIST 1.1. Pathologic response was defined by the presence or absence of viable tumors on pathologic review when available.

Massachusetts General Hospital patient specimens. Patients initiating anti-PD1 therapy (pembrolizumab) as front-line treatment for metastatic melanoma at MGH provided written informed consent for the collection of tissue and blood samples for research (DF/HCC IRB-approved protocol 11-181). Responders showed radiographic decrease in disease at initial staging for ≥12 weeks. Non-responders did not exhibit radiographic response and/or had rapid progression. Progression-free survival was defined as days from treatment start to radiographic scan when progression was first noted (uncensored) or last progression-free scan (censored). Overall survival was defined as days from treatment start to date of death (uncensored) or last follow-up (censored).

Animal models

All animals were housed at the Vincent A. Stabile Research building animal facility at the MCC, which is fully accredited by the Association

for Assessment and Accreditation of Laboratory Animal Care International (434) and is managed in accordance with the Guide for the Care and Use of Laboratory Animals, the Animal Welfare Regulations Title 9 Code of Federal Regulations Subchapter A, 'Animal Welfare', parts 1–3 (AWR), the Public Health Service Policy on Humane Care and Use of Laboratory Animals and by the USF Institutional Animal Care and Use Committee's Principles and Procedures of Animal Care and Use. Experiments in this study received institutional approval by the Moffitt IACUC committee (protocol RIS00001625). Four-to-six-week-old female C3H/HeN and male C57BL6 mice were purchased from Charles Rivers Laboratories; immunodeficient NSG mice[63] were from the Lau laboratory breeding colony. All mice were housed in rooms on a standard 12-h–12-h light cycle, with a temperature range of 68–72 °F and humidity range of 30–70%.

Power calculations determined cohort sizes to detect significant changes in tumor sizes. Generally, by using ten mice per group, we estimate that we will be able to detect a 10% difference in tumor development between any two conditions with *a P* value of 0.05 and a power value of 0.80 and a 20% change with *a P* value of 0.05 and a power of 0.95. This calculation has been used previously to designate groups of ten mice[9], which accommodates for incidental loss of mice due to issues beyond our control (for example, tumor ulceration that requires exclusion from the study). Mouse tumor volumes were measured using length, width and depth divided by 2. At each experimental endpoint or if mice showed signs of metastatic disease, mice were humanely euthanized using CO_2 inhalation in accordance with American Veterinary Medical Association guidelines.

For all mouse models, 1×10^6 melanoma cells were injected subcutaneously in the right hind flanks of each mouse. Between 7 and 14 d, when tumor volumes reached ~150 mm^3, mice were supplemented with or without 100 mM L-fuc (Biosynth) via drinking water, which was provided ad libitum[9]. This dosage is within previously reported ranges for dietary supplementation with L-fuc and other similar dietary sugars (for example, D-mannose) in rodent studies[64–68]. When tumors reached the endpoint volume (~2 cm^3), animals were killed, and tumors and organs were processed for flow cytometric profiling or histological analysis as indicated. The maximum permitted tumor volume was not exceeded.

Models of control versus mFuk with or without L-fucose. For Fig. 1 and Extended Data Fig. 1, SW1 or SM1 mouse melanoma cells were injected into syngeneic C3H/HeN (or NSG) female or C57BL/6 male mice, respectively, as follows: parental SW1 cells for Fig. 1a, parental SM1 cells for Extended Data Fig. 1e, SW1 cells stably expressing either EV or mFuk for Fig. 1e and parental SW1 cells for Extended Data Fig. 1k.

Models of control versus L-fucose with or without FTY720. For Fig. 2b, SW1 mouse melanoma cells were injected into syngeneic C3H/HeN female mice. FTY720 (Cayman Chemicals) was administered at 20 µg every 2 d to inhibit lymph node egress[69] starting on day 12, just before the initiation of L-fuc administration, until endpoint.

Immunodepletion mouse models. For Fig. 1l–o and Extended Data Fig. 1s–w, 3 d before tumor engraftment, PBS (control) or ~300 µg anti-CD4 (20 mg per kg) or anti-CD8 (20 mg per kg) antibodies were administered by intraperitoneal injection into the indicated cohorts of mice. Immunodepletion antibody or PBS injections were continued every 3–4 d until endpoint. Syngeneic recipient C3H/HeN female or C57BL/6 male mice were injected with SW1 or SM1 cells, respectively.

HLA-A and HLA-DRB1 knockdown and glycofucomutant H2EB1 reconstitution mouse model. For Figs. 3d–h and 4f, SW1 mouse melanoma cells expressing shNT, shH2K1, shEB1, shNT and EV, shEB1 and EV, shEB1 and $EB1^{WT}$, or shEB1 and $EB1^{N46G}$ were injected into syngeneic C3H/HeN female mice.

Anti-PD1 mouse model. For Fig. 5, SW1 or SM1 mouse melanoma cells were injected into syngeneic C3H/HeN female or C57BL/6 male mice, respectively. After approximately 7 d, when the mouse tumors reached ~150 mm^3, the mice were supplemented either with or without 100 mM L-fuc via drinking water, which was provided ad libitum. Simultaneously, PBS (control) or anti-PD1 antibody (20 mg per kg) was administered via intraperitoneal injection every 3–4 d until endpoint.

Statistics and reproducibility

GraphPad Prism version 8 was used for statistical calculations unless otherwise indicated. For all comparisons between two independent conditions, *t*-tests were performed to obtain *P* values and s.e.m. For comparisons between ≥2 groups, one-way or two-way ANOVAs were performed, and *P* values and s.e.m. were obtained. For the TMA data, the Wilcoxon signed-rank test was used to determine significance. Data distribution was assumed to be normal but this was not formally tested; we have included individual data points in all relevant plots.

For molecular and cell-based assays, experiments were performed in three biologically independent replicates with similar results and outcomes. No data were excluded from analyses. Only when cell lines were either contaminated or lost knockdown or exogenous expression were the cell lines regenerated and the experiments performed again (that is, more than three times total). For cost feasibility, three biologically independent specimens were pooled for mass spectrometric profiling experiments, which were performed once. However, post-profiling validation experiments were performed in three biologically independent experiments with similar results.

Each of the 12 unique mouse models was performed once. However, with the exception of the NSG mouse model (Extended Data Fig. 1k), each mouse model contained built-in repeat control groups (for example, control and L-fuc-fed-only groups) that were repeated in at least one of the other models. Furthermore, SW1 mouse models were replicated in SM1 mouse models, which show conservation of our results across different melanoma mutational background and strains and sex of mice. No mice were excluded from the analyses unless tumors ulcerated or did not graft successfully before treatment.

In general, for molecular, cell-based and mouse-based experiments, the investigators were not blinded to allocation during experiments and outcome assessment; randomization was not used in these cases. However, the investigators were blinded to allocation during TMA and patient specimen immunostaining, signal measurement and initial analysis.

Reporting summary

Further information on research design is available in the Nature Portfolio Reporting Summary linked to this article.

Data availability

Mass spectrometry data have been deposited in ProteomeXchange with the primary dataset identifiers as follows: Extended Data Fig. 2a, PXD038065; Extended Data Fig. 2e, PXD038636; Extended Data Fig. 3a, PXD038303; Extended Data Fig. 5a, PXD038068. All other data supporting the findings of this study are available from the corresponding author on reasonable request. Source data are provided with this paper.

Code availability

No custom code was used in this study.

References

1. Weber, J. S. et al. Nivolumab versus chemotherapy in patients with advanced melanoma who progressed after anti-CTLA-4 treatment (CheckMate 037): a randomised, controlled, open-label, phase 3 trial. *Lancet Oncol.* **16**, 375–384 (2015).

2. Chacon, J. A. et al. Manipulating the tumor microenvironment ex vivo for enhanced expansion of tumor-infiltrating lymphocytes for adoptive cell therapy. *Clin. Cancer Res.* **21**, 611–621 (2015).
3. Tawbi, H. A. et al. Relatlimab and nivolumab versus nivolumab in untreated advanced melanoma. *N. Engl. J. Med.* **386**, 24–34 (2022).
4. Spitzer, M. H. et al. Systemic immunity is required for effective cancer immunotherapy. *Cell* **168**, 487–502 (2017).
5. Schneider, M., Al-Shareffi, E. & Haltiwanger, R. S. Biological functions of fucose in mammals. *Glycobiology* **27**, 601–618 (2017).
6. Marth, J. D. & Grewal, P. K. Mammalian glycosylation in immunity. *Nat. Rev. Immunol.* **8**, 874–887 (2008).
7. Keeley, T. S., Yang, S. & Lau, E. The diverse contributions of fucose linkages in cancer. *Cancers* **11**, 1241 (2019).
8. Adhikari, E. et al. L-fucose, a sugary regulator of antitumor immunity and immunotherapies. *Mol. Carcinog.* **61**, 439–453 (2022).
9. Lau, E. et al. The transcription factor ATF2 promotes melanoma metastasis by suppressing protein fucosylation. *Sci. Signal.* **8**, ra124 (2015).
10. Gentles, A. J. et al. The prognostic landscape of genes and infiltrating immune cells across human cancers. *Nat. Med.* **21**, 938–945 (2015).
11. Alspach, E. et al. MHC-II neoantigens shape tumour immunity and response to immunotherapy. *Nature* **574**, 696–701 (2019).
12. Knight, D. A. et al. Host immunity contributes to the anti-melanoma activity of BRAF inhibitors. *J. Clin. Invest.* **123**, 1371–1381 (2013).
13. Kennedy, R. & Celis, E. Multiple roles for $CD4^+$ T cells in anti-tumor immune responses. *Immunol. Rev.* **222**, 129–144 (2008).
14. Lim, C. J. et al. Integrin-mediated protein kinase A activation at the leading edge of migrating cells. *Mol. Biol. Cell* **19**, 4930–4941 (2008).
15. del Pozo, M. A., Sanchez-Mateos, P., Nieto, M. & Sanchez-Madrid, F. Chemokines regulate cellular polarization and adhesion receptor redistribution during lymphocyte interaction with endothelium and extracellular matrix. Involvement of cAMP signaling pathway. *J. Cell Biol.* **131**, 495–508 (1995).
16. Kumari, S. et al. Cytoskeletal tension actively sustains the migratory T-cell synaptic contact. *EMBO J.* **39**, e102783 (2020).
17. Oberprieler, N. G. et al. High-resolution mapping of prostaglandin E2-dependent signaling networks identifies a constitutively active PKA signaling node in $CD8^+CD45RO^+$ T cells. *Blood* **116**, 2253–2265 (2010).
18. Binnewies, M. et al. Unleashing type-2 dendritic cells to drive protective antitumor $CD4^+$ T cell immunity. *Cell* **177**, 556–571 (2019).
19. Tay, R. E., Richardson, E. K. & Toh, H. C. Revisiting the role of $CD4^+$ T cells in cancer immunotherapy—new insights into old paradigms. *Cancer Gene Ther.* **28**, 5–17 (2021).
20. Bajana, S. et al. Differential $CD4^+$ T-cell memory responses induced by two subsets of human monocyte-derived dendritic cells. *Immunology* **122**, 381–393 (2007).
21. Kramer, A., Green, J., Pollard, J. Jr. & Tugendreich, S. Causal analysis approaches in ingenuity pathway analysis. *Bioinformatics* **30**, 523–530 (2014).
22. Rossjohn, J. et al. T cell antigen receptor recognition of antigen-presenting molecules. *Annu. Rev. Immunol.* **33**, 169–200 (2015).
23. Orczyk-Pawilowicz, M., Augustyniak, D., Hirnle, L. & Katnik-Prastowska, I. Lectin-based analysis of fucose and sialic acid expressions on human amniotic IgA during normal pregnancy. *Glycoconj. J.* **30**, 599–608 (2013).
24. Bastian, K., Scott, E., Elliott, D. J. & Munkley, J. FUT8 α-(1,6)-fucosyltransferase in cancer. *Int. J. Mol. Sci.* **22**, 455 (2021).
25. Hashim, O. H., Jayapalan, J. J. & Lee, C. S. Lectins: an effective tool for screening of potential cancer biomarkers. *PeerJ* **5**, e3784 (2017).
26. Nonaka, M. et al. Mannan-binding protein, a C-type serum lectin, recognizes primary colorectal carcinomas through tumor-associated Lewis glycans. *J. Immunol.* **192**, 1294–1301 (2014).
27. Osuga, T. et al. Relationship between increased fucosylation and metastatic potential in colorectal cancer. *J. Natl Cancer Inst.* **108**, djw038 (2016).
28. Zou, X. et al. A standardized method for lectin microarray-based tissue glycome mapping. *Sci. Rep.* **7**, 43560 (2017).
29. Yuhki, N. et al. Comparative genome organization of human, murine, and feline MHC class II region. *Genome Res.* **13**, 1169–1179 (2003).
30. Chang, C. S., Brossay, L., Kronenberg, M. & Kane, K. P. The murine nonclassical class I major histocompatibility complex-like CD1.1 molecule protects target cells from lymphokine-activated killer cell cytolysis. *J. Exp. Med.* **189**, 483–491 (1999).
31. Raulet, D. H. et al. Specificity, tolerance and developmental regulation of natural killer cells defined by expression of class I-specific Ly49 receptors. *Immunol. Rev.* **155**, 41–52 (1997).
32. Gay, D. et al. Functional interaction between human T-cell protein CD4 and the major histocompatibility complex HLA-DR antigen. *Nature* **328**, 626–629 (1987).
33. Walser-Kuntz, D. R., Weyand, C. M., Fulbright, J. W., Moore, S. B. & Goronzy, J. J. HLA-DRB1 molecules and antigenic experience shape the repertoire of CD4 T cells. *Hum. Immunol.* **44**, 203–209 (1995).
34. Fleury, S. et al. HLA-DR polymorphism affects the interaction with CD4. *J. Exp. Med.* **182**, 733–741 (1995).
35. Steentoft, C. et al. Precision mapping of the human *O*-GalNAc glycoproteome through SimpleCell technology. *EMBO J.* **32**, 1478–1488 (2013).
36. Stern, L. J. et al. Crystal structure of the human class II MHC protein HLA-DR1 complexed with an influenza virus peptide. *Nature* **368**, 215–221 (1994).
37. Lenertz, L. Y. et al. Mutation of putative *N*-linked glycosylation sites on the human nucleotide receptor $P2X_7$ reveals a key residue important for receptor function. *Biochemistry* **49**, 4611–4619 (2010).
38. Tsiakas, K. et al. Mutation of the glycosylated asparagine residue 286 in human CLN2 protein results in loss of enzymatic activity. *Glycobiology* **14**, 1C–5C (2004).
39. Sun, J., Boado, R. J., Pardridge, W. M. & Sumbria, R. K. Plasma pharmacokinetics of high-affinity transferrin receptor antibody–erythropoietin fusion protein is a function of effector attenuation in mice. *Mol. Pharm.* **16**, 3534–3543 (2019).
40. Rillahan, C. D. et al. Global metabolic inhibitors of sialyl- and fucosyltransferases remodel the glycome. *Nat. Chem. Biol.* **8**, 661–668 (2012).
41. Anderson, K. S. & Cresswell, P. A role for calnexin (IP90) in the assembly of class II MHC molecules. *EMBO J.* **13**, 675–682 (1994).
42. Johnson, D. B. et al. Melanoma-specific MHC-II expression represents a tumour-autonomous phenotype and predicts response to anti-PD-1/PD-L1 therapy. *Nat. Commun.* **7**, 10582 (2016).
43. Rodig, S. J. et al. MHC proteins confer differential sensitivity to CTLA-4 and PD-1 blockade in untreated metastatic melanoma. *Sci. Transl. Med.* **10**, eaar3342 (2018).
44. Gellrich, F. F., Schmitz, M., Beissert, S. & Meier, F. Anti-PD-1 and novel combinations in the treatment of melanoma—an update. *J. Clin. Med.* **9**, 223 (2020).
45. Zuazo, M. et al. Functional systemic CD4 immunity is required for clinical responses to PD-L1/PD-1 blockade therapy. *EMBO Mol. Med.* **11**, e10293 (2019).

46. Pirozyan, M. R. et al. Pretreatment innate cell populations and CD4 T cells in blood are associated with response to immune checkpoint blockade in melanoma patients. *Front. Immunol.* **11**, 372 (2020).
47. Oh, D. Y. et al. Intratumoral $CD4^+$ T cells mediate anti-tumor cytotoxicity in human bladder cancer. *Cell* **181**, 1612–1625 (2020).
48. Tay, R. E., Richardson, E. K. & Toh, H. C. Revisiting the role of $CD4^+$ T cells in cancer immunotherapy—new insights into old paradigms. *Cancer Gene Ther.* **28**, 5–17 (2020).
49. Kagamu, H. et al. $CD4^+$ T-cell immunity in the peripheral blood correlates with response to anti-PD-1 therapy. *Cancer Immunol. Res.* **8**, 334–344 (2020).
50. Alam, M. S. Proximity ligation assay (PLA). *Curr. Protoc. Immunol.* **123**, e58 (2018).
51. Norton, P. et al. Development and application of a novel recombinant *Aleuria aurantia* lectin with enhanced core fucose binding for identification of glycoprotein biomarkers of hepatocellular carcinoma. *Proteomics* **16**, 3126–3136 (2016).
52. Etzioni, A. & Tonetti, M. Fucose supplementation in leukocyte adhesion deficiency type II. *Blood* **95**, 3641–3643 (2000).
53. Marquardt, T. et al. Correction of leukocyte adhesion deficiency type II with oral fucose. *Blood* **94**, 3976–3985 (1999).
54. Liang, W. et al. Core fucosylation of the T cell receptor is required for T cell activation. *Front. Immunol.* **9**, 78 (2018).
55. Okada, M. et al. Blockage of core fucosylation reduces cell-surface expression of PD-1 and promotes anti-tumor immune responses of T cells. *Cell Rep.* **20**, 1017–1028 (2017).
56. Alatrash, G. et al. Fucosylation enhances the efficacy of adoptively transferred antigen-specific cytotoxic T lymphocytes. *Clin. Cancer Res.* **25**, 2610–2620 (2019).
57. Nordenfelt, P., Elliott, H. L. & Springer, T. A. Coordinated integrin activation by actin-dependent force during T-cell migration. *Nat. Commun.* **7**, 13119 (2016).
58. Keren, L. et al. A structured tumor-immune microenvironment in triple negative breast cancer revealed by multiplexed ion beam imaging. *Cell* **174**, 1373–1387 (2018).
59. Nestarenkaite, A. et al. Immuno-interface score to predict outcome in colorectal cancer independent of microsatellite instability status. *Cancers* **12**, 2902 (2020).
60. O'Malley, D. P. et al. Immunohistochemical detection of PD-L1 among diverse human neoplasms in a reference laboratory: observations based upon 62,896 cases. *Mod. Pathol.* **32**, 929–942 (2019).
61. Yang, X. A public genome-scale lentiviral expression library of human ORFs. *Nat. Methods* **8**, 659–661 (2011).
62. Cox, J. & Mann, M. MaxQuant enables high peptide identification rates, individualized p.p.b.-range mass accuracies and proteome-wide protein quantification. *Nat. Biotechnol.* **26**, 1367–1372 (2008).
63. Maletzki, C. et al. NSG mice as hosts for oncological precision medicine. *Lab. Invest.* **100**, 27–37 (2020).
64. Grabinger, T. et al. Alleviation of intestinal inflammation by oral supplementation with 2-fucosyllactose in mice. *Front. Microbiol.* **10**, 1385 (2019).
65. Smith, P. L. et al. Conditional control of selectin ligand expression and global fucosylation events in mice with a targeted mutation at the FX locus. *J. Cell Biol.* **158**, 801–815 (2002).
66. Wang, H. et al. D-mannose ameliorates autoimmune phenotypes in mouse models of lupus. *BMC Immunol.* **22**, 1 (2021).
67. Wang, Y. et al. Loss of α1,6-fucosyltransferase suppressed liver regeneration: implication of core fucose in the regulation of growth factor receptor-mediated cellular signaling. *Sci. Rep.* **5**, 8264 (2015).
68. Zhang, D. et al. D-mannose induces regulatory T cells and suppresses immunopathology. *Nat. Med.* **23**, 1036–1045 (2017).
69. Zhi, L. et al. FTY720 blocks egress of T cells in part by abrogation of their adhesion on the lymph node sinus. *J. Immunol.* **187**, 2244–2251 (2011).

Acknowledgements

We are grateful to all Lau laboratory members and to S. Chellappan, J. Cleveland, J. Conéjo-Garcia, G. DeNicola, F. Karreth, A. Gomes and D. Abate-Daga at the Moffitt Cancer Center for critical readings of the manuscript. We also thank Z. Ronai for his mentorship, as well as Michiko Fukuda, Minoru Fukuda and H. Freeze for their technical advice and guidance in glycobiological studies. We acknowledge E. Sahakian for technical assistance and advice and M. Meister, T. Alvarez and T. Christie for administrative support. This work has been supported in part by the Moffitt/USF Vivarium, Flow Cytometry Core, Biostatistics and Bioinformatics Shared Resource, Analytical Microscopy, Tissue Core and Proteomics and Metabolomics Core Facilities (we thank in particular N. Clark and J. Balasi for technical Tissue Core support and B. Fang for proteomic repository assistance) and the Advanced Analytical and Digital Laboratory at the H. Lee Moffitt Cancer Center and Research Institute, an NCI-designated Comprehensive Cancer Center (P30-CA076292). We acknowledge the Proteomic Shared Resource of the Sanford Burnham Prebys Medical Discovery Institute for their assistance with fucosylated proteomic screening. Support from an NIGMS grant (GM061126 to R.S.H.), an NCI grant (KO8CA252164 to J.M.), NCI grants (K99CA172705, R00CA172705 and R01CA241559 to E.K.L.), a Miles for Moffitt grant (to E.K.L.) and a Harry J. Lloyd Charitable Trust Melanoma Research grant (to E.K.L.) are gratefully acknowledged.

Author contributions

Conceptualization: E.K.L., D.K.L., S.A.P.-T., V.C.L.; methodologies: E.K.L., D.K.L., C.B., P.I., K.K., Q.L., E.A., D.B.W., M.B., A.M.-M., M.M., G.W., C.M., S.M., A.G., L.D., V.I.; computational analysis: Q.M., D.B.W., B.C., J.J., J.N., X.W.; resources: J. Markowitz, J. Messina, P.-L.C., K.L.T., D.T.F., T.S., M.G.W., J.A.W., G.M.B., B.R.; writing: E.K.L., D.K.L.; supervision: E.K.L., S.A.P.-T., V.C.L., R.S.H., X.W., B.R., J.M.K.; funding acquisition: E.K.L., R.S.H. All authors commented on the manuscript.

Competing interests

G.M.B. has SRA with Palleon Pharmaceuticals, Olink Proteomics, InterVenn Biosciences and formerly with Takeda Oncology. She consults for Merck and InterVenn. She served on the SAB and a steering committee for Nektar Therapeutics. J. Markowitz has served on an advisory board for Array BioPharma in the past 2 years and has been a PI of grants and funding to his institution from Morphogenesis, Navigate BioPharma, Jackson Laboratory, Microba, Merck, MacroGenics and Reata Pharmaceuticals. The Moffitt Cancer Center has licensed intellectual property related to the proliferation and expansion of tumor-infiltrating lymphocytes (TILs) to Iovance Biotherapeutics. Moffitt has also licensed intellectual property to Tuhura Biopharma. S.A.P.-T. is an inventor on such intellectual property. S.A.P.-T. is listed as a co-inventor on a patent application with Provectus Biopharmaceuticals. S.A.P.-T. participates in sponsored research agreements with Provectus Biopharmaceuticals, Iovance Biotherapeutics, Intellia Therapeutics, Dyve Biosciences and Turnstone Biologics that are not related to this research. S.A.P.-T. has received ad hoc consulting fees from Seagen and serves as an advisor for KSQ Therapeutics. The remaining authors declare no competing interests.

Additional information

Extended data is available for this paper at https://doi.org/10.1038/s43018-022-00506-7.

Supplementary information The online version contains supplementary material available at https://doi.org/10.1038/s43018-022-00506-7.

Correspondence and requests for materials should be addressed to Eric K. Lau.

Peer review information *Nature Cancer* thanks Charles Dimitroff for their contribution to the peer review of this work.

[1]Department of Tumor Biology, H. Lee Moffitt Cancer Center and Research Institute, Tampa, FL, USA. [2]Cancer Biology Ph.D. Program, University of South Florida, Tampa, FL, USA. [3]Molecular Medicine Program, H. Lee Moffitt Cancer Center and Research Institute, Tampa, FL, USA. [4]Department of Immunology, H. Lee Moffitt Cancer Center and Research Institute, Tampa, FL, USA. [5]Immunology Program, H. Lee Moffitt Cancer Center and Research Institute, Tampa, FL, USA. [6]Department of Drug Discovery, H. Lee Moffitt Cancer Center and Research Institute, Tampa, FL, USA. [7]Complex Carbohydrate Research Center, the University of Georgia, Athens, GA, USA. [8]Department of Surgery, Massachusetts General Hospital, Boston, MA, USA. [9]Department of Surgical Oncology, MD Anderson Cancer Center, Houston, TX, USA. [10]Department of Cutaneous Oncology, H. Lee Moffitt Cancer Center and Research Institute, Tampa, FL, USA. [11]Department of Biostatistics and Bioinformatics, H. Lee Moffitt Cancer Center and Research Institute, Tampa, FL, USA. [12]Advanced Analytical and Digital Laboratory, H. Lee Moffitt Cancer Center and Research Institute, Tampa, FL, USA. [13]Department of Analytic Microscopy, H. Lee Moffitt Cancer Center and Research Institute, Tampa, FL, USA. [14]Department of Pathology, H. Lee Moffitt Cancer Center and Research Institute, Tampa, FL, USA. [15]Department of Diagnostic Imaging, H. Lee Moffitt Cancer Center and Research Institute, Tampa, FL, USA. [16]Proteomics and Metabolomics Core, H. Lee Moffitt Cancer Center and Research Institute, Tampa, FL, USA. [17]Department of Molecular Oncology, H. Lee Moffitt Cancer Center and Research Institute, Tampa, FL, USA. [18]Department of Genomic Medicine, MD Anderson Cancer Center, Houston, TX, USA. [19]Broad Institute of Harvard and Massachusetts Institute of Technology, Massachusetts General Hospital, Boston, MA, USA. ✉e-mail: eric.lau@moffitt.org

https://doi.org/10.1038/s43018-022-00506-7

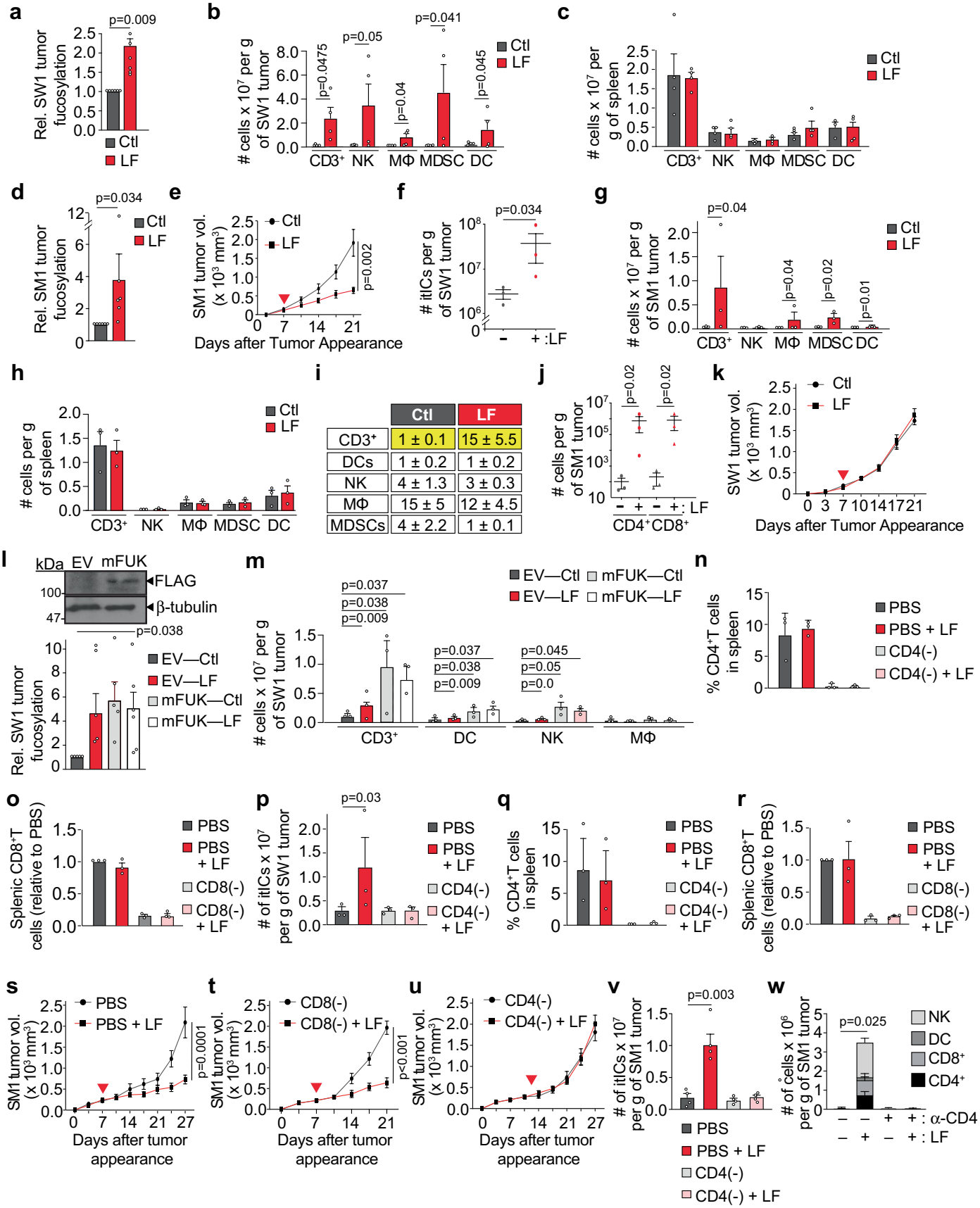

Extended Data Fig. 1 | See next page for caption.

https://doi.org/10.1038/s43018-022-00506-7

Extended Data Fig. 1 | Confirming increased tumor fucosylation and itIC counts, splenic immune cell profiles, and correlations between tumor fucosylation and CD3$^+$T cells in female vs. male melanoma patients. Immunofluorescent (IF) staining analysis of SW1 tumor FFPE sections for intratumoral fucosylation **(a)** (n = 2 representative fields from 3 mice per group). Flow cytometric profiling of intratumoral immune cell (itIC) subpopulations (CD3$^+$T cells, natural killer cells (NKs), macrophages (MΦ), MDSC-like cells (MDSCs), and dendritic cells (DCs)) in **(b)** SW1 tumors (n = 4 mice per group) and **(c)** spleens (n = 3 mice per group) in control (Ctl)- or L-fuc (LF)-supplemented SW1 tumor-bearing C3H/HeN mice from Fig. 1a. IF staining analysis of SM1 tumor FFPE sections for intratumoral fucosylation **(d)** (n = 2 representative fields from 3 mice per group)**. (e)** Volumetric growth curves (n = 7 and 8 mice for Ctl and LF groups, respectively), **(f)** total itIC counts, **(g)** absolute itIC subpopulations, **(h)** splenic immune cell profiles, **(i)** % itIC subpopulations, **(j)** intratumoral CD4$^+$ and CD8$^+$T cell counts of SM1 tumors in C57BL6 mice (for **(f-j)**, n = 3 mice per group). **(k)** Volumetric growth curves of SW1 tumors in NSG mice (n = 10 mice per group). **(l)** IB analysis confirming mFUK expression in SW1 cells (*upper*), IF staining analysis of SW1 tumor FFPE sections for intratumoral fucosylation (*lower*) (n = 2 representative fields from 3 mice per group), and **(m)** flow cytometric profiling of indicated immune populations in EV- or mFUK-expressing SW1 tumors from Ctl- or LF-supplemented C3H/HeN mice. **(n)** Flow cytometric profiling of splenic CD4$^+$T cells in control (PBS-injected) vs. CD4$^+$T cell-depleted (CD4(-)) SW1 tumor-bearing C3H/HeN mice supplemented ± LF. **(o)** IF staining profiling of splenic CD8$^+$T cells in control vs. CD8$^+$ T cell-depleted (CD8(-)) SW1 tumor-bearing C3H/HeN mice. Flow cytometric profiling of **(p)** total itIC counts in control vs. CD4(-) SW1 tumor-bearing C3H/HeN mice and **(q)** splenic CD4$^+$T cells in control vs. CD4(-) SM1 tumor-bearing C57BL6 mice supplemented ± LF. Percentages represent % CD4$^+$T of total splenic cells. **(r)** IF profiling of splenic CD8$^+$T cells in control vs. CD8(-) SM1 tumor-bearing C57BL6 mice fed ± L-fuc (for **(m-r)**, n = 3 mice per group). Volumetric growth curves for SM1 tumors in **(s)** control (PBS)-injected, **(t)** CD8(-), or **(u)** CD4(-) C57BL6 mice (for **(s-u)**, n = 7 mice per group, except for PBS + LF, which had 8 mice). **(v)** Flow cytometric profiling of total itIC counts in control **(s)** vs. CD4(-) **(u)** mice. **(w)** Comparison of intratumoral NK, DC, CD8$^+$T, and CD4$^+$T subpopulations from control or CD4(-) (α-CD4) depleted tumors in **(s)** and **(u)** (for **(v and w)**, n = 4 mice per group). *For each mouse model: when tumors reached ~150 mm^3, Ctl- or LF-supplemented water (100 mM; red triangle = initiated supplementation) was provided ad libitum. The tumor growth curves are means ± SEM per group. Relative fold-changes in splenic CD8$^+$ T cells were determined by (total intrasplenic CD8$^+$ signal area / total intrasplenic DAPI area) as a measure of relative CD8$^+$T cell abundance/spleen*. All error bars represent standard error of the mean.

https://doi.org/10.1038/s43018-022-00506-7

a

Top 5 fucosylation-altered signaling pathways identified in CD3/CD28-activated human CD4⁺T cells

	p-value	Overlap (hits/pathway components)
RhoA signaling	*2.31E-13*	*17.9% (7/39)*
PKA signaling	*7.86E-09*	*4.2% (7/166)*
Actin cytoskeleton signaling	*3.61E-07*	*5.4% (5/92)*
Cell cycle control of chromosomal replication	*7.30E-07*	*9.1% (4/44)*
Integrin signaling	*7.67E-07*	*4.7% (5/107)*

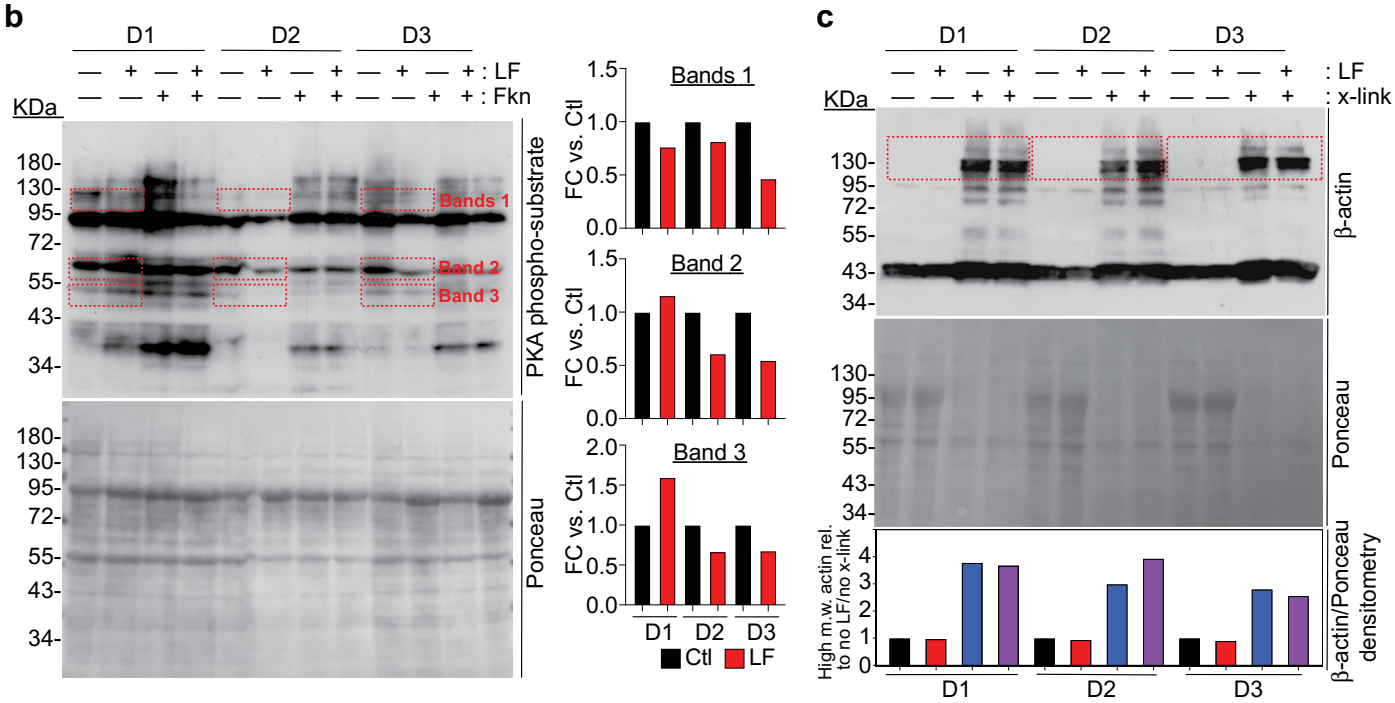

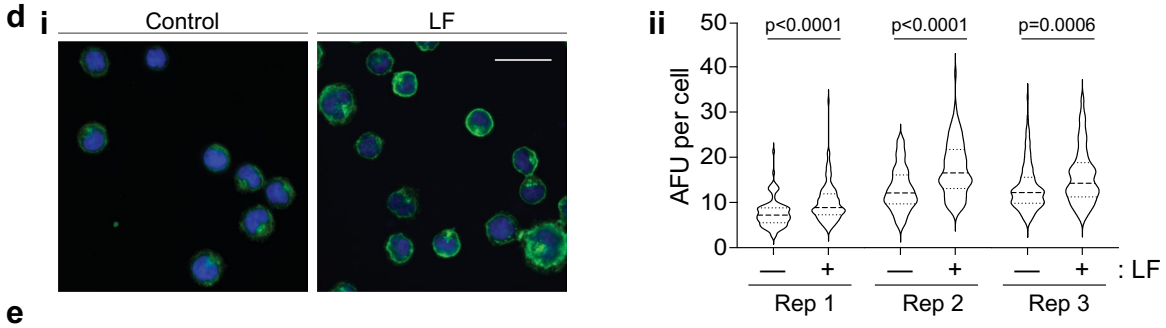

e

Top 5 AAL-bound (fucosylated) proteins identified in CD3/CD28-activated human CD4⁺T cells

	Fold-increased AAL binding by L-fucose treatment
ORC1 (origin recognition complex subunit 1)	*2.931*
POTEE/POTEF (POTE ankyrin domain family member E)	*2.766*
B4GALT1 (beta-1,4-galactosyltransferase 1)	*2.441*
ATG7 (autophagy related 7)	*2.233*
ITGB5 (integrin subunit beta 5)	*2.203*

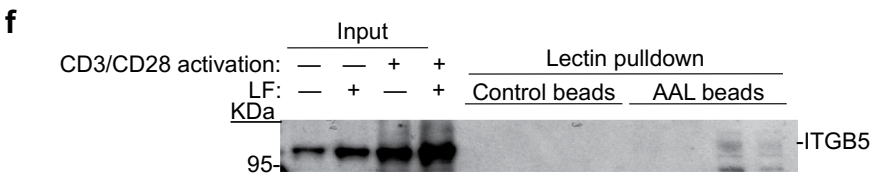

Extended Data Fig. 2 | See next page for caption.

https://doi.org/10.1038/s43018-022-00506-7

Extended Data Fig. 2 | Fucosylation of CD4$^+$T cells affects PKA activity and actin polymerization; and the identification of Integrin β5 as a highly fucosylated protein in activated CD4$^+$T cells. (a) Top 5 pathways in human CD4$^+$T cells that are affected by increased fucosylation identified by Ingenuity Pathway Analysis (Qiagen; pathways were identified from phosphoproteomic analyses of CD3/CD28-activated human PBMC-derived CD4$^+$T cells treated ± 250 μM L-fucose (LF) isolated from 3 independent healthy human donors (D1, D2, D3)). **(b)** (*left*) Immunoblot of PKA phosphorylated substrates (*top*) and Ponceau staining (*bottom*) of human PBMC-derived, CD3/CD28-activated CD4$^+$T cells that were treated ± 250 μM LF (for 72 h) ± 10 μM forskolin (Fkn, a PKA agonist; for 6 h). (*right*) Densitometric quantification of selected bands (red dashed boxes) normalized to Ponceau staining. **(c)** Immunoblot of β-actin (*top*) and Ponceau staining (*middle*) of 3 human donor PBMC-derived, CD3/CD28 activated CD4$^+$T cells were treated ± 250 μM LF ± 25 mM DTSP crosslinker (x-link). (*bottom*) Densitometric quantification of high molecular weight β-actin oligomers (red dashed boxes) normalized to Ponceau intensity and then normalized to -LF, -x-link samples. **(d) (i)** Coverslip-grown Jurkat cells treated ± 250 μM LF (for 72 h), fixed, and stained with DAPI (*blue*) and phalloidin-488 (*green*) for actin cytoskeleton. Scale bar: 25 μm. **(ii)** Integrated actin signal densities per cell from 3 biological replicates of Jurkat cells grown/treated as in **(i)** were measured using ImageJ v1.53a (NIH) and plotted as shown using GraphPad Prism v8. **(e)** Top 5 AAL-bound (fucosylated) proteins in human PBMC-derived, CD3/CD28-activated CD4$^+$T cells from **(a)** that were identified by Ingenuity Pathway Analysis (Qiagen). **(f)** Of the 5 top hits, we were only able to validate fucosylation of Integrin β5 by LPD analysis of human PBMC-derived, CD3/CD28-activated CD4$^+$T cells.

https://doi.org/10.1038/s43018-022-00506-7

a

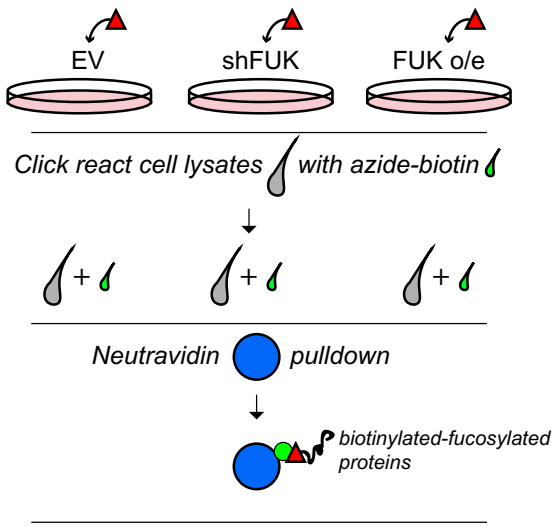

Top 20 pathways identified by Ingenuity Pathway Analysis

EIF2 signaling
Regulation of eIF4 and p70S6K signaling
mTOR signaling
Unfolded protein response
Protein ubiquitination pathway
Aldosterone signaling in epithelial cells
Glycolysis I
Gluconeogenesis I
Phagosome maturation
NRF2-mediated oxidative stress response
BAG2 signaling
Remodeling of epithelial adherens junctions
Glutaryl-CoA degradation
Sirtuin signaling pathway
Antigen presentation pathway
Tryptophan degradation III
TCA cycle II
eNOS signaling
Purine nucleotides de novo biosynthesis II
Germ cell-Sertoli cell junction signaling

1 immune-related cluster

CANX	*-3.249*
HLA-DRB1	*-1.437*
PDIA3	*-1.136*
CALR	*-0.962*
HLA-A	*-0.212*

11 plasma membrane proteins

STRAP	*-2.095*
SPTBN1	*-1.982*
CSPG4	*-1.906*
TFRC	*-1.688*
ATP1A1	*-1.59*
HLA-DRB1	*-1.437*
AIMP2	*-0.981*
ANXA5	*-0.739*
CLTC	*-0.314*
SLC3A2	*-0.224*
HLA-A	*-0.212*

b

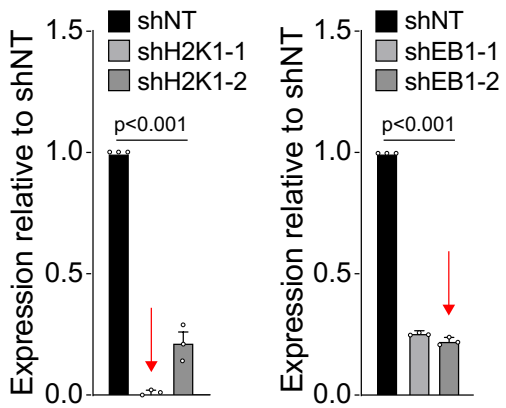

Extended Data Fig. 3 | See next page for caption.

https://doi.org/10.1038/s43018-022-00506-7

Extended Data Fig. 3 | Fucosylated mass spectrometric analysis and knockdown efficiency of H2K1 and H2EB1. (a) (*left*) Schematic for proteomic analysis of fucosylated proteins in human WM793 melanoma cells using pLenti-GFP empty vector (EV)-, pLenti-FUK-GFP (o/e)-, or shFUK-expressing WM793 cells from[8]. Click chemistry biotinylated-fucosylated proteins that were pulled down using Neutravidin beads from the 6-alkynyl-L-fucose-labeled cells were subjected to LC-MS/MS, and hits were subjected to the indicated filtering scheme followed by Ingenuity Pathway Analysis (Qiagen). (*right*) Top 20 pathways, plasma membrane- and immune-related proteins identified by Ingenuity Pathway Analysis (Qiagen) to be significantly altered by fucosylation. **(b)** qRT-PCR analysis confirming knockdown of H2K1 (shH2K1; *left*) or H2EB1 (shEB1; *right*) using 2 shRNAs per target compared to control non-targeting (shNT) shRNA. n = 3 biologically independent experiments. Red arrows indicate the specific shRNA clones used in functional experiments in the remainder of the study. All error bars represent standard error of the mean.

https://doi.org/10.1038/s43018-022-00506-7

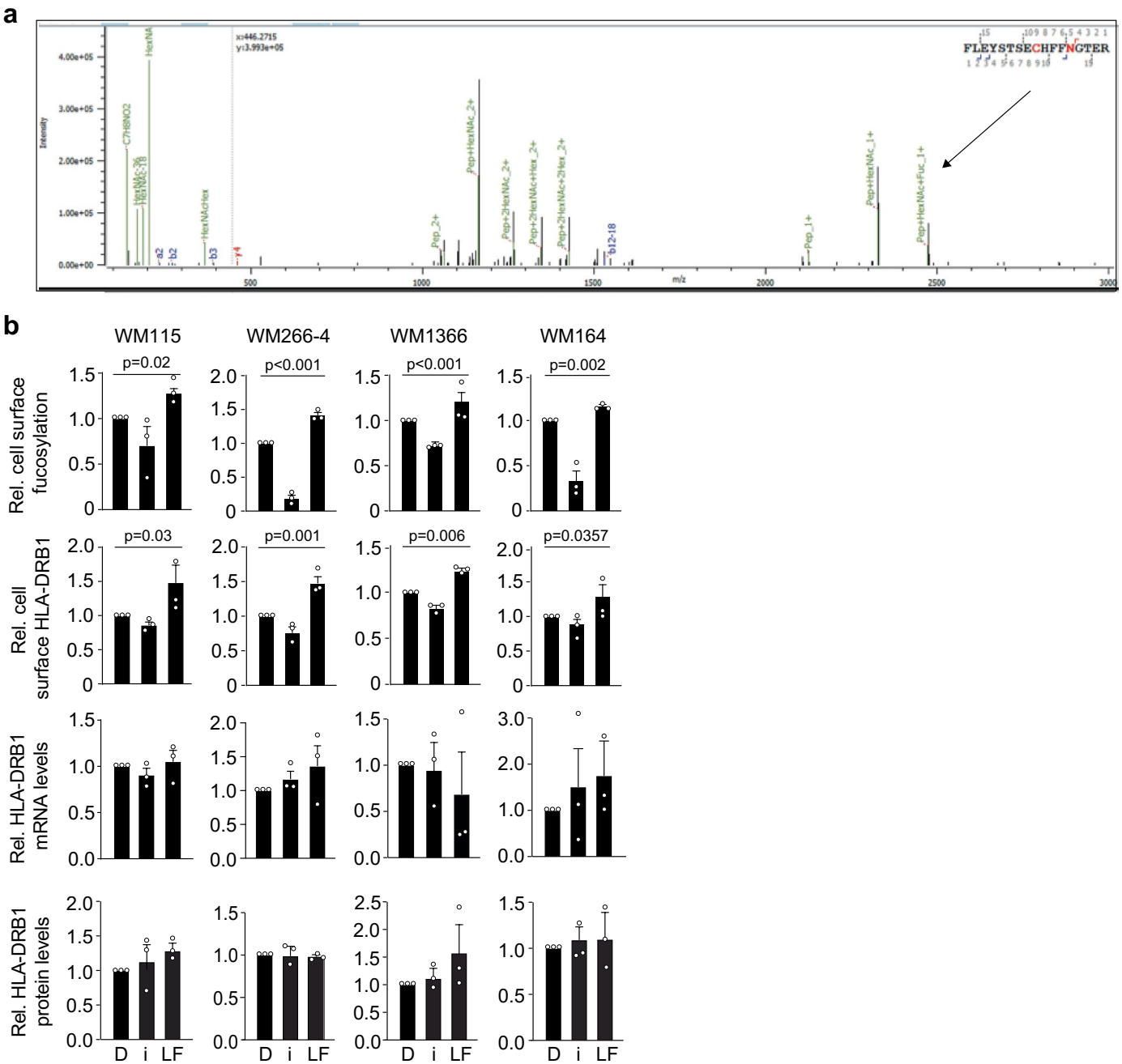

Extended Data Fig. 4 | nano-LC/MS spectral identification of fucosylated HLA-DRB1 peptide; and the effects of modulating fucosylation on HLA-DRB1 localization, total protein, and mRNA levels. (a) nano-LC/MS/MS spectra showing fucosylated HLA-DRB1 peptide (*arrow*). **(b)** Flow cytometric analysis for relative cell surface fucosylation (*upper*) and cell surface HLA-DRB1 levels (*upper middle*), qRT-PCR analysis of relative HLA-DRB1 mRNA levels (*lower middle*), and IB analysis of HLA-DRB1 protein levels (*lower*) in indicated melanoma cell lines treated with DMSO (D), 250 μM FUTi (i), or 250μM L-fuc (LF). n = 3 biologically independent experiments. All error bars represent standard error of the mean.

https://doi.org/10.1038/s43018-022-00506-7

a

Mass Spectrometry Input

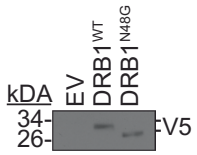

b

Top 5 pathways identified by Ingenuity Pathway Analysis

	p-value	Overlap (hits/pathway components)
Antigen presentation pathway	*2.31E-13*	*17.9% (7/39)*
Phagosome maturation	*7.86E-09*	*4.2% (7/166*
Crosstalk between dendritic and natural killer cells	*3.61E-07*	*5.4% (5/92)*
B cell development	*7.30E-07*	*9.1% (4/44)*
PD-1, PD-L1 cancer immunotherapy pathway	*7.67E-07*	*4.7% (5/107)*

Antigen Presentation Pathway fHLA-DRB1 binding partners identified	Fold-reduced binding (N48G to WT)
PDIA3 (protein disulfide isomerase family A member 3)	*-4.439*
CANX (calnexin)	*-3.795*
HLA-A (major histocompatibility complex, class I, A)	*-2.877*
HLA-G (major histocompatibility complex, class I, G)	*-1.765*
HLA-DRA (major histocompatibility complex, class II, DR alpha)	*-1.365*
HLA-DRB1 (major histocompatibility complex, class II, DR beta 1)	*-1.216*
HLA-DRB5 (major histocompatibility complex, class II, DR beta 5)	*-1.1*

c

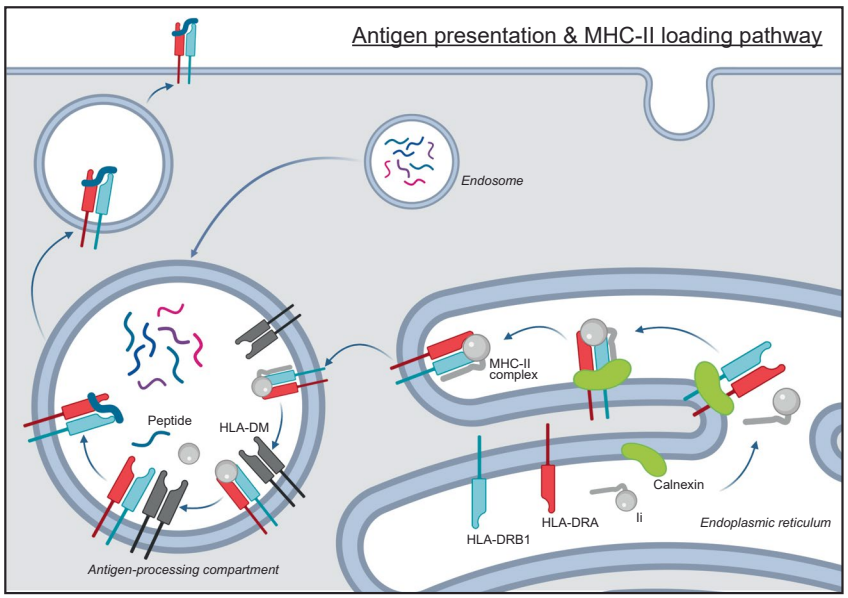

d

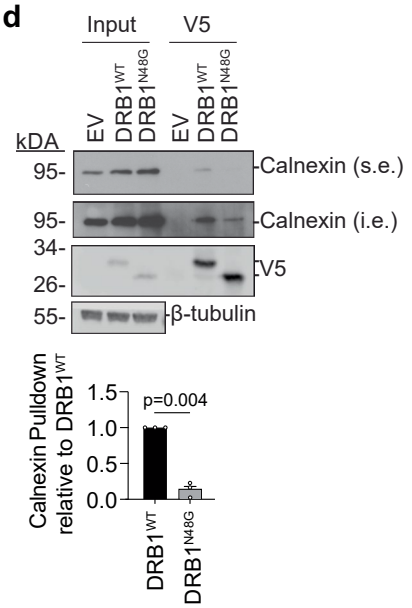

e

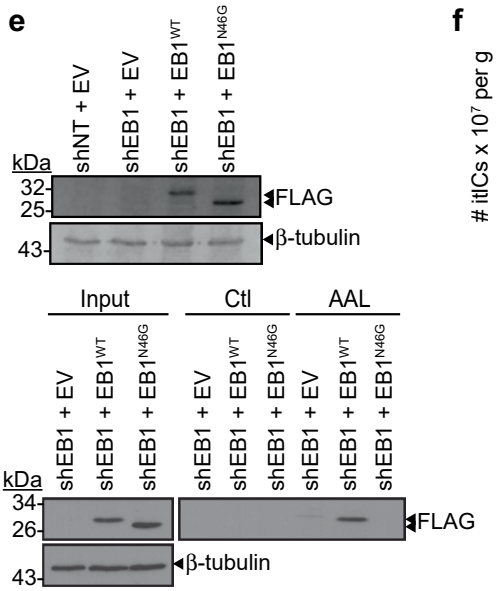

f

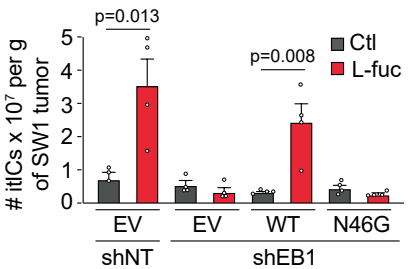

g

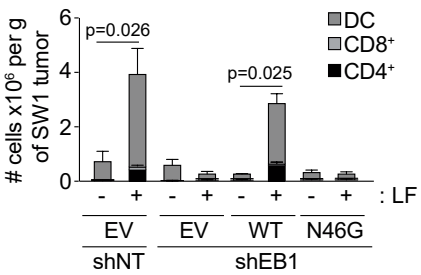

h

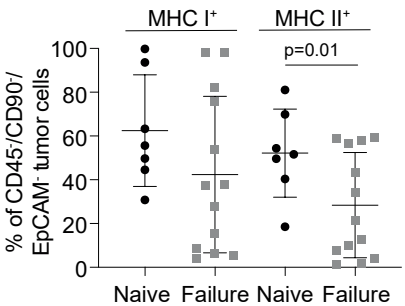

Extended Data Fig. 5 | See next page for caption.

https://doi.org/10.1038/s43018-022-00506-7

Extended Data Fig. 5 | Proteomic analysis reveal fuco/glycosylation of HLA-DRB1 decreases binding to calnexin; knockdown/reconstitution and fucosylation of EB1 WT and N46G and its effects on itICs *in vivo*; loss of MHCII is associated with anti-PD1 failure in melanoma patients. (a) IB analysis of 5% input of V5 IP of tagged EV, HLA-DRB1^{WT}, and HLA-DRB1^{N48G} mutant in WM793 melanoma cells. **(b)** (*top*) Top 5 pathways that are affected by HLA-DRB1 fuco/glycosylation identified by Ingenuity Pathway Analysis (Qiagen). (*bottom*) Individual proteins in the Antigen Presentation Pathway identified in the screen. **(c)** Schematic of proteins identified in the Antigen Presentation & MHC-II Loading Pathway. The schematic was created using BioRender.com. **(d)** (top) IP of EV, HLA-DRB1^{WT}, and HLA-DRB1^{N48G} and IB analysis of calnexin (short exposure (s.e.), calnexin (intermediate exposure (that is), V5, and β-tubulin. (bottom) Quantification of calnexin band intensity to V5 intensity in V5 IP lanes (relative to HLA-DRB^{WT}; (n = 3 biologically independent experiments). **(e)** (*upper*) IB analysis of non-targeting shRNA + empty vector (shNT + EV) or shEB1-expressing cells (*from* Extended Data Fig. 3b) reconstituted with FLAG-EV (shEB1 + EV), FLAG-EB1^{WT} (shEB1 + EB1^{WT}), or FLAG-EB1^{N46G} (shEB1 + EB1^{N46G}). (*lower*) LPD and IB analysis of indicated cells from (*upper*). Shown are representative images from 3 biologically independent experiments. **(f)** Total itIC counts and **(g)** indicated immune subpopulations in the shNT or shEB1 knockdown/EB1^{WT}- or EB1^{N46G}-reconstituted SW1 tumors of the Ctl- or LF-supplemented C3H/HeN mice. n = 4 mice per group. **(h)** % of total CD45^{-}/CD90^{-}/EpCAM^{-} tumor cells exhibiting positive pan MHC-I (*left*) or pan MHC-II (*lower*) staining from either anti-PD1 naïve patients (black squares; n = 7) or patients who failed anti-PD1 (*grey squares*; n = 13). All error bars represent standard error of the mean.

https://doi.org/10.1038/s43018-022-00506-7

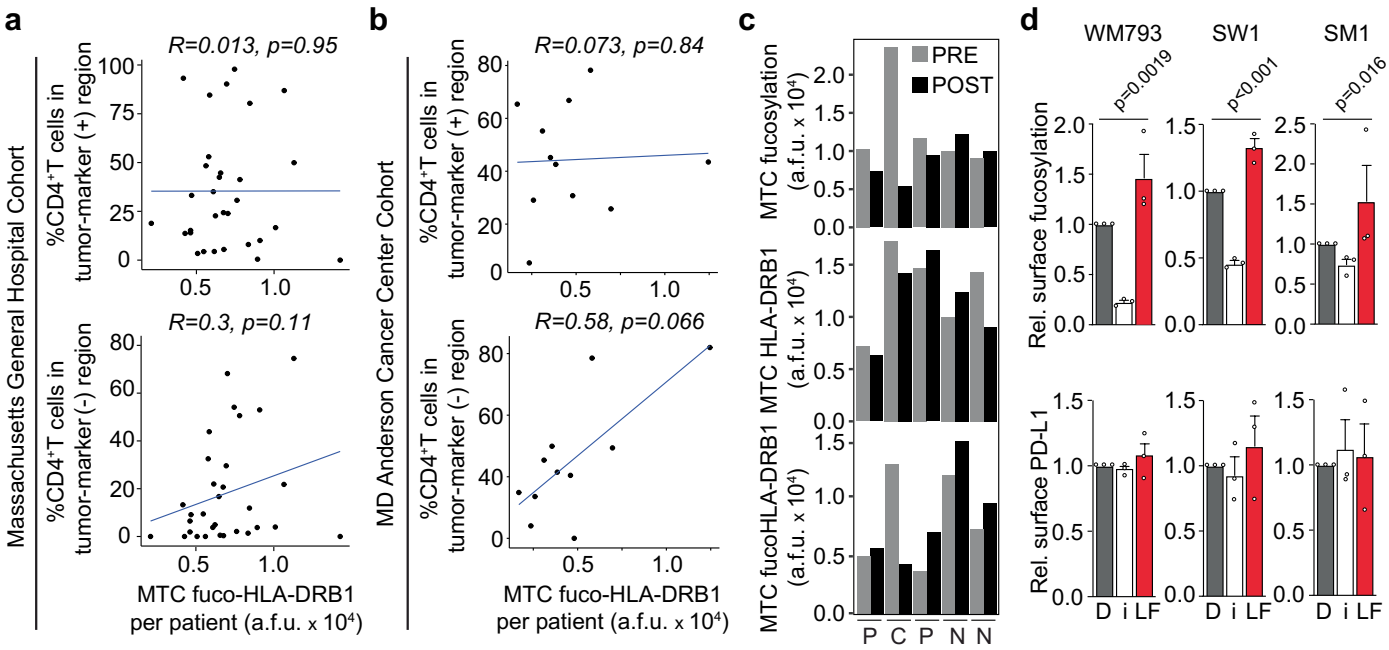

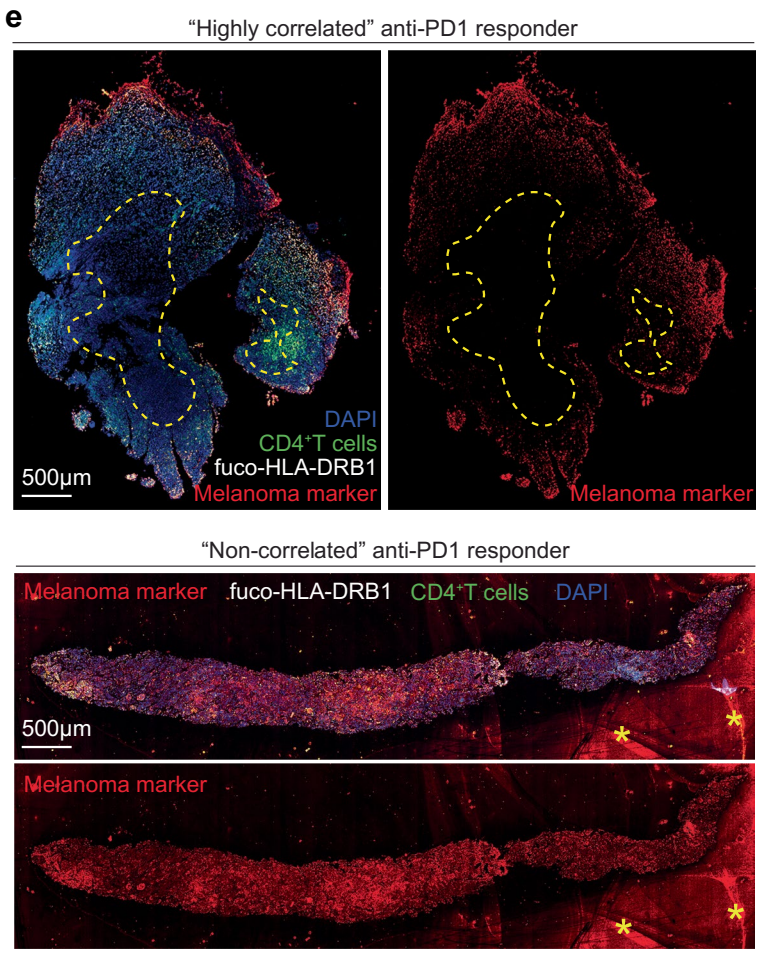

Extended Data Fig. 6 | See next page for caption.

https://doi.org/10.1038/s43018-022-00506-7

Extended Data Fig. 6 | Spatial and pre-/post-anti-PD1 trends in fucosylation, total-/fuco-HLA-DRB1 & CD4$^+$T cells in patient specimens, lack of effect of fucosylation on cell surface presence of melanoma PD-L1, & examples of stromal content discrepancy among patient biopsies. (a) WM793 (*left*), SW1 (*middle*), and SM1 (*right*) cells were treated with DMSO (D) or 250 μM FUTi (i) or L-fuc (LF) and subjected to flow cytometric assessment of changes in cell surface levels of fucosylation (*upper*) and PD-L1 (*lower*). n = 3 biologically independent experiments. All error bars represent standard error of the mean. Association of mean tumor cellular (MTC) fucosylated HLA-DRB1 with % CD4$^+$T cells either inside (tumor marker (+); *upper*) or outside (tumor border/periphery; tumor marker (-); *lower*) melanoma tumors in patients from **(b)** Massachusetts General Hospital or **(c)** MD Anderson Cancer Center (MDACC). **(d)** A 'Highly correlated' anti-PD1 responder biopsy with high fuco-HLA-DRB1 and CD4$^+$T cell (*upper*) vs. a 'non-correlated' responder biopsy with low fuco-HLA-DRB1 and CD4$^+$T cells were stained for indicated markers. Yellow dashed lines represent the tumor:stromal interface surrounding melanoma marker-negative stroma in the highly correlated responder that is absent in the non-correlated responder. Yellow asterisks indicate non-nucleated non-specific staining on the non-correlated responder slide. **(e)** Mean tumor cellular (MTC) total fucosylation (*upper*), total HLA-DRB1 (*middle*), or fucosylated HLA-DRB1 (*lower*) levels in MDACC patient-matched pre-/post-anti-PD1 tumor specimens. C/P/N = Complete/partial/non-responder, respectively. P-values shown are two-sided P-values derived from the Spearman correlation test.

nature portfolio

Corresponding author(s): Eric K. Lau

Last updated by author(s): Dec 14, 2022

Reporting Summary

Nature Portfolio wishes to improve the reproducibility of the work that we publish. This form provides structure for consistency and transparency in reporting. For further information on Nature Portfolio policies, see our Editorial Policies and the Editorial Policy Checklist.

Statistics

For all statistical analyses, confirm that the following items are present in the figure legend, table legend, main text, or Methods section.

n/a	Confirmed	
☐	☒	The exact sample size (*n*) for each experimental group/condition, given as a discrete number and unit of measurement
☐	☒	A statement on whether measurements were taken from distinct samples or whether the same sample was measured repeatedly
☐	☒	The statistical test(s) used AND whether they are one- or two-sided *Only common tests should be described solely by name; describe more complex techniques in the Methods section.*
☐	☒	A description of all covariates tested
☐	☒	A description of any assumptions or corrections, such as tests of normality and adjustment for multiple comparisons
☐	☒	A full description of the statistical parameters including central tendency (e.g. means) or other basic estimates (e.g. regression coefficient) AND variation (e.g. standard deviation) or associated estimates of uncertainty (e.g. confidence intervals)
☐	☒	For null hypothesis testing, the test statistic (e.g. *F*, *t*, *r*) with confidence intervals, effect sizes, degrees of freedom and *P* value noted *Give P values as exact values whenever suitable.*
☒	☐	For Bayesian analysis, information on the choice of priors and Markov chain Monte Carlo settings
☒	☐	For hierarchical and complex designs, identification of the appropriate level for tests and full reporting of outcomes
☐	☒	Estimates of effect sizes (e.g. Cohen's *d*, Pearson's *r*), indicating how they were calculated

Our web collection on statistics for biologists contains articles on many of the points above.

Software and code

Policy information about availability of computer code

Data collection	For flow cytometry, we used Cellquest v6 or FACSDiva v9 software (BD Biosciences) on a LSR Flow Cytometer (BD Biosciences) for collection of data. For qRT-PCR, we used CFX Manager v3.1 software on a CFX96 Touch Real-Time PCR Detection System (Bio-Rad)
Data analysis	Usage of these software in specific experiments are explained further in the main text and Methods sections. For mass spectrometry, data were analyzed using both Proteome Discoverer v2.1 (ThermoFisher Scientific) with Byonic (Protein Metrics) as a module and Byonic standalone v2.10.5. All extracted ion chromatograms (EICs) were generated using Xcalibur Qual Browser v4.0 (ThermoFisher Scientific). MaxQuant software (version 1.6.2.10) was used to identify and quantify the proteins for the DDA runs. For pathway analyses of our fucosylated proteomic hits, we used Ingenuity Pathway Analysis (Qiagen). For N-linked glycosylation site prediction of HLA-DRB1, we used NetNGlyc 1 (DTU Bioinformatics). For O-linked glycosylation site prediction HLA-DRB1, we used NetOGlyc 4 (DTU Bioinformatics). For structural modeling, we used PyMOL v2.0 (Molecular Graphics System, Schrödinger, LLC). For flow cytometry, we used FlowJo v9 software (BD Biosciences) for analysis. For analysis of mouse tumor images (e.g., fucosylation intensity), we used ImageJ v1.53a (NIH). For general statistical analyses, we used Prism v8 (GraphPad).

For manuscripts utilizing custom algorithms or software that are central to the research but not yet described in published literature, software must be made available to editors and reviewers. We strongly encourage code deposition in a community repository (e.g. GitHub). See the Nature Portfolio guidelines for submitting code & software for further information.

Data

Policy information about availability of data

All manuscripts must include a data availability statement. This statement should provide the following information, where applicable:

- Accession codes, unique identifiers, or web links for publicly available datasets
- A description of any restrictions on data availability
- For clinical datasets or third party data, please ensure that the statement adheres to our policy

Mass spectrometry data have been deposited in ProteomeXchange with the primary dataset identifiers as follows: Extended Data Fig. 2a: PXD038065; Extended Data Fig. 2e: PXD038636; Extended Data Fig. 3a: PXD038303; Extended Data Fig. 5a: PXD038068. Source data for Figs. 1, 2, 3, 4, 5, and 7 and Extended Data Figs. 1,2, 3, 4, 5, and 6 have been provided as Source Data files. The source data for the single-cell-level dot plots in Figs. 7bi, 7bii, and 7biii are provided via figshare (https://doi.org/10.6084/m9.figshare.21433155). All other data supporting the findings of this study are available from the corresponding author on reasonable request.

Human research participants

Policy information about studies involving human research participants and Sex and Gender in Research.

Reporting on sex and gender	This study focuses on basic biological mechanisms regulating tumor immunological interactions in melanoma, and as such, sex and gender were not predominant topics of study. However, factoring for biological variability, patient-derived de-identified specimens included tissues from both female and male patients. Inclusion criteria was not sex-based but rather based on availability, and specifically, confirmed diagnosis of melanoma and treatment with anti-PD1 immune checkpoint blockade therapy. In general, there were more male than female patient specimens, which likely reflects the higher incidence rate of melanoma in men than women.
Population characteristics	The tumor microarray used in Fig. 1i-1j is a commercial product from US Biomax. This microarray includes specimens from 18 female and 22 male patients; age range: 25-88; tumor stage range: 1A-4. For Figs. 6 and 7 and Extended Data Fig. 6, patient specimen characteristics were as follows: Moffitt Cancer Center patients: 2 female and 2 male patients, age range: 51-80 University of Texas MD Anderson Cancer Center patients: 3 female and 8 male patients, age range: 44-76 Massachusetts General Hospital patients: 10 female and 21 male, age range: 41-82 The PBMCs used in this study were purchased from LifeSouth without sex-based inclusion criteria and were derived from deidentified healthy male and female donors between the ages of 30-50 (average age range).
Recruitment	The tumor microarray used in Fig. 1i-1j is a commercial product from US Biomax, and thus the construction of the microarray was subject to availability and out of our control. We chose this particular microarray as it represented relatively even representation of female vs. male patients, staging, and tumor sites. For Figs. 6 and 7 and Extended Data Fig. 6, consented patients with advanced stage melanoma who received anti-PD1 immune checkpoint blockade therapy between 2014 and 2020 at Moffitt Cancer Center, UT MD Anderson Cancer Center, or Massachusetts General Hospital were identified, and specimens collected and analyzed following patient consent under respective Institutional Review Board-approved protocols. Responder status criteria: •For Moffitt Cancer Center: patients exhibiting >20 months of progression-free survival were considered as “Responders”, whereas “Non-Responder” patients progressed in less than 6 months after receiving anti-PD1. •For UT MD Anderson Cancer Center: responder status was defined as a complete or partial response and non-responder was defined as stable or progressive disease by RECIST 1.1. Pathologic response was defined by the presence or absence of viable tumor on pathologic review when available. •For Massachusetts General Hospital: patients were classified as responders (R) who showed clear radiographic decrease in disease at initial staging through a minimum of 12 weeks. Patients classified as non-responders (NR) did not respond to treatment radiographically and/or had clear and rapid progression. Progression free survival (PFS) is given in days from treatment start to radiographic scan when progression was first noted (uncensored) or last progression free scan (censured). Overall survival (OS) is given in days from treatment start to date of death (uncensored) or last follow-up (censored). The fresh PBMCs were purchased from LifeSouth bloodbank. The lots of PBMCs were acquired from deidentified healthy male and female donors. There were no recruitment criteria except that they are healthy and between the ages 30-50 (average age range).
Ethics oversight	For the TMA, donors provided consent prior to specimen donation to US Biomax. For Figs. 6 and 7 and Extended Data Fig. 6, previous studies from which this study acquired Moffitt patient specimens were performed under Moffitt's Institutional Review Board-approved protocols including the Total Cancer Care protocol. All patient samples were de-identified prior to use in research studies. All patients signed approved consent forms. All patient specimens acquired from the University of Texas MD Anderson Cancer Center and Massachusetts General Hospital were collected prior to this study for other studies and protocols that were previously approved by their respective Institutional Review Boards. Fresh PBMCs were purchased as a de-identified products from healthy human donors from LifeSouth bloodbank. Donors were consented by LifeSouth prior to donation.

Note that full information on the approval of the study protocol must also be provided in the manuscript.

Field-specific reporting

Please select the one below that is the best fit for your research. If you are not sure, read the appropriate sections before making your selection.

☒ Life sciences ☐ Behavioural & social sciences ☐ Ecological, evolutionary & environmental sciences

For a reference copy of the document with all sections, see nature.com/documents/nr-reporting-summary-flat.pdf

Life sciences study design

All studies must disclose on these points even when the disclosure is negative.

Sample size	For mouse models: We planned all experiments to implement 10 mice per group. With this number, we estimated the ability to detect a 10% difference in tumor development between any 2 conditions with a p-value of 0.05 and a power of 0.80, and a 20% change with a p-value of 0.05 and a power of 0.95. In our experience, 10 mice per group have been more than sufficient to provide statistical power and buffer for incidental loss of mice due to factors outside of our control (e.g., aberrant tumor ulceration resulting in exclusion of the animal from the results). This calculation has been used previously to designate groups of 10 mice (Lau et al. Sci Signal 2015). For patient specimen studies: our cohort numbers were limited by availability and inclusion criteria from each cancer center. For all other experiments involving other living entities (i.e., cell-based assays), every experiment was performed in at least standard biological triplicate. Experiments entailing specific sample sizes included flow cytometry. For all flow cytometric analyses, we stained and analyzed 1x10^6 per mouse tumor for at least 3 mice per treatment group per standard protocols from previous publications of our collaborator and co-author, Dr. Shari-Pilon Thomas. For cell surface flow cytometric analysis experiments using human or mouse melanoma cell lines, we stained ~1x10^5 cells per sample but used a gating and analysis standard of 10,000 cells per sample. As the study focus was not a sex-associated biological mechanism, we implemented both male and female mouse models as well as a tumor microarray with ~ equal distribution of male and female melanoma tissue donors, and both male and female bulk tumor tissue donors.
Data exclusions	No data were excluded from the analyses.
Replication	All cell-based experiments were repeated in independent biological triplicates. In addition, to ensure reproducibility, key experiments (for example, lectin pulldown and IP-lectin blot for HLA-DRB1 to demonstrate fucosylation) were performed independently by Lau laboratory members other than those who performed the experiments for the data shown in the Figures). All of the data shown include "successful" replication attempts; "unsuccessful" replication attempts that are not shown include for example, if on rare occasion, cells either were contaminated or lost stable expression of a viral construct. In those cases, cells were either re-cultured or parental cells were re-transduced to generate indicated cell lines, and the experiments were repeated until at least 3 independent biological replicates were attained. In no case, ever, were experiments repeated due to bias. Importantly, for the 12 mouse models showcased in this study, each successive mouse experiment generally included independently repeated control and experimental conditions from a preceding experiment, ensuring evidence of reproducibility and consistency. For example, control vs. fucose fed treatment mouse groups (no other injections or viral modifications, etc.) were independently replicated 7 times. For mass spectrometric experiments, mass spectrometry was performed once on samples pooled from 3 biological replicates. Subsequent validation was performed in biological triplicate.
Randomization	For cell- and mouse-based experiments, treatment groups were delineated as indicated in each experiment/Figure (detailed treatment group designs specific to each of the 12 mouse models in this study are in the Methods section); randomization was not applicable for these experiments. For the patient specimen staining analyses: Tumor microarray staining (Fig. 1i-k) was by definition randomized, as all biopsies were simultaneously stained and scanned. Patient tumor biopsy staining (Fig. 5c-e): We obtained blinded patient specimens from Moffitt, MD Anderson, and Harvard/Massachusetts General Hospital. We immunostained and analyzed the specimens completely blinded to patient responder status; thus, by design, all patient specimens were randomized during processing and analysis.
Blinding	Tumor microarray staining (Fig. 1i-k) and analysis was performed blinded, until the final analysis, whereupon the biostatisticians, who are not part of the Lau laboratory, were unblinded to tissue donor sex, age, and stage. Patient tumor biopsy staining (Fig. 4c-e): We obtained blinded patient specimens from Moffitt, MD Anderson, and Harvard/Massachusetts General Hospital. Staining and analysis was performed blinded, until the final analysis, whereupon the biostatisticians, who are not part of the Lau laboratory, were unblinded to responder patient responder status. The investigators were completely blinded to group allocation during data collection and all analyses.

Reporting for specific materials, systems and methods

We require information from authors about some types of materials, experimental systems and methods used in many studies. Here, indicate whether each material, system or method listed is relevant to your study. If you are not sure if a list item applies to your research, read the appropriate section before selecting a response.

Materials & experimental systems

n/a	Involved in the study
☐	☒ Antibodies
☐	☒ Eukaryotic cell lines
☒	☐ Palaeontology and archaeology
☐	☒ Animals and other organisms
☐	☒ Clinical data
☒	☐ Dual use research of concern

Methods

n/a	Involved in the study
☒	☐ ChIP-seq
☐	☒ Flow cytometry
☒	☐ MRI-based neuroimaging

Antibodies

Antibodies used

Mouse anti-V5 (Cat. #: v8012; final use concentration: 0.2 µg/mL; Clone #V5-10; Lot #00000999991; Millipore Sigma (St. Louis, MO))
•Website: https://www.sigmaaldrich.com/US/en/product/sigma/v8012
•Associated Figure(s): Fig 2c & 3c, extended data fig 6a-d

Mouse anti-V5 gel (Cat. #:a7345; Clone # V5-10; Lot #119M4791V; Millipore Sigma (St. Louis, MO))
•Website: https://www.sigmaaldrich.com/US/en/product/sigma/a7345?context=product
•Associated Figure(s): Fig 2c, extended data fig 6a-d

Mouse anti-human HLA-DRB1 (Cat. #:ab215835; final use concentration: 0.2 µg/mL for IF; Clone #HLA-DRB/1067; Lot# NA; Abcam (Cambridge, UK))
•Website: https://www.abcam.com/hla-class-ii-drb1-antibody-hla-drb1067-ab215835.html
•Associated Figure(s): Fig 3d, Fig 5b-f, Extended Data Fig 7b-e

Rabbit anti-human HLA-DRB1 (Cat. #:ab92371; final use concentration: 0.2 µg/mL for WB; Polyclonal; Lot #GR922220-2; Abcam (Cambridge, UK))
•Website: https://www.abcam.com/hla-class-ii-drb1-antibody-ab92371.html
•Associated Figure(s): Fig. 2a-e, Fig 3e, Extended Fig 3b

Mouse anti-⊟-tubulin (Cat. #: E7; final use concentration: 0.3 µg/mL; clone# E7; Lot# 11/29/18; developed by M. McCutcheon and S. Carroll and obtained from Developmental Studies Hybridoma Bank (University of Iowa, Iowa City, IA))
•Website: https://dshb.biology.uiowa.edu/E7_2
•Associated Figure(s): Fig 2a, Fig 3c,e, Extended Data Fig 1l, Extended Data Fig 5b, Extended Data Fig 6e

Goat anti-biotin (Cat. #: sp3000; final use concentration: 0.1 µg/mL; polyclonal; Lot# ZH0202; Vector Labs (Burlingame, CA))
•Website: https://vectorlabs.com/goat-anti-biotin-unconjugated.html#documents
•Associated Figure(s): Fig 5b-f, Extended Data Fig 7b-h

Anti-mouse CD4 (Cat. #: BE0003-1; Dosage: 20 mg/kg for immunodepletion; Clone# GK1.5; Lot# 689518A1; Bioxcell (West Lebanon, NH))
•Website: https://bxcell.com/product/m-cd4/
Manufacturer verified for use: immunodepletion, flow cytometry, western blot
•Associated Figure(s): Fig 1n-o, Extended Data Fig 1 n,p,q,u,v,w

Anti-mouse CD8 (Cat. #: BE0061; Dosage: 20 mg/kg for immunodepletion; Clone# 2.43; Lot #: 643017F1; Bioxcell (West Lebanon, NH))
•Website: https://bxcell.com/product/m-cd8a-2/
•Associated Figure(s): Fig 1m, Extended Data 1o,r,t

Anti-mouse IgGk horseradish peroxidase (HRP) (Cat. #: SC-516102; final use concentration: 0.04 µg/mL; Clone: NA; Lot#F1620; Santa Cruz Biotechnology (Dallas, TX))
•Website: https://www.scbt.com/p/m-igg-kappa-bp-hrp
•Associated Figure(s): Fig 2a-c, Fig 3c, Extended Data Fig 1l, Extended Data Fig 5b

Mouse anti-rabbit HRP (Cat. #: SC-2357; final use concentration: 0.04 µg/mL; Clone# NA; Lot# G0720; Santa Cruz Biotechnology (Dallas, TX))
•Website: https://www.scbt.com/p/mouse-anti-rabbit-igg-hrp
•Associated Figure(s): Fig 2a-c, Fig 3c, Extended Data Fig 1l, Extended Data Fig 5b

Goat anti-rabbit AlexaFluor 488 (Cat. #: A11008; final use concentration: 0.04 µg/mL; Clone # NA; Lot #1275894; ThermoFisher Scientific (Waltham, MA))
•Website: https://www.thermofisher.com/antibody/product/Goat-anti-Rabbit-IgG-H-L-Highly-Cross-Adsorbed-Secondary-Antibody-Polyclonal/A32731
•Associated Figure(s): Fig 3e, Extended Data 5b

Donkey anti-mouse AlexaFluor 594 (Cat. #: A21203; final use concentration: 0.05 µg/mL; Clone #NA; Lot #1918277; ThermoFisher Scientific (Waltham, MA))
•Website: https://www.thermofisher.com/antibody/product/Donkey-anti-Mouse-IgG-H-L-Highly-Cross-Adsorbed-Secondary-Antibody-Polyclonal/A32744
•Associated Figure(s): Fig 1i-k

AlexaFluor 594 donkey anti-rabbit (Cat. #: A21207; final use concentration: 0.05 µg/mL; Clone #NA; Lot #1938375; ThermoFisher Scientific (Waltham, MA))
•Website: https://www.thermofisher.com/antibody/product/Donkey-anti-Rabbit-IgG-H-L-Highly-Cross-Adsorbed-Secondary-Antibody-Polyclonal/A-21207
•Associated Figure(s): Fig 3d,

Rabbit anti-Mart1 (Cat. #: SAB4500949; final use concentration: 0.2 µg/mL; Clone #NA; Lot #310257; Millipore Sigma (St. Louis, MO)
•Website: https://www.sigmaaldrich.com/US/en/product/sigma/sab4500949?context=product
•Associated Figure(s): Fig 1i-k, Fig 5c-f, Extended Data Fig 1a,d,l, Extended Data Fig 4 b-h

Rabbit anti-S100 (Cat. #: Z0311; final use concentration: 0.2 µg/mL; Clone #NA; Lot #NA; Agilent Technologies (Santa Clara, CA))
•Website: https://www.agilent.com/en/product/immunohistochemistry/antibodies-controls/primary-antibodies/s100-(dako-omnis)-76198
•Associated Figure(s): Fig 1i-k, Fig 5c-f, Extended Data Fig 1a,d,l, Extended Data Fig 7 b-h

Rat APC anti-mouse CD3 (Cat. #: 100236; final use concentration: 0.5 µg/mL; Clone #17A2; Lot #B274725; Biolegend, inc. (San Diego, CA))
•Website: https://www.biolegend.com/en-us/products/apc-anti-mouse-cd3-antibody-8055
•Associated Figure(s): Fig 1c,d,g,h,o, Fig 2h, Extended Data Fig 1b,c,g,h,i,j,m,n,q,w, Extended Data Fig 3e

Rat Pacific Blue anti-mouse CD4 (Cat. #: 100428; final use concentration: 0.5 µg/mL; Clone #GK1.5; Lot #B265546; Biolegend, Inc. (San Diego, CA))
•Website:https://www.biolegend.com/en-us/products/pacific-blue-anti-mouse-cd4-antibody-3316?GroupID=BLG4745
•Associated Figure(s): Fig 1d,h,o, Fig 2h, Extended Data Fig 1j,n,q,w, Extended Data Fig 3e

Rat BV785 anti-mouse CD8 (Cat. #: 100750; final use concentration: 0.5 µg/mL; Clone #53-6.7; Lot #B266841; Biolegend (San Diego, CA))
•Website: https://www.biolegend.com/en-us/products/brilliant-violet-785-anti-mouse-cd8a-antibody-7957
•Associated Figure(s): Fig 1d,h,o, Fig 2h, Extended Data Fig 1j,w, Extended Data Fig 3e

Rat FITC anti-mouse F4/80 (Cat. #: 123108; final use concentration: 0.5 µg/mL; Clone #BM8; Lot #B257637; Biolegend, Inc (San Diego, CA))
•Website: https://www.biolegend.com/en-us/products/fitc-anti-mouse-f4-80-antibody-4067
•Associated Figure(s): Fig 1c,g, Extended Data Fig 1b,c,g,h,i,m

Rat APC anti-mouse GR-1 (Cat. #: 108412; final use concentration: 0.5 µg/mL; Clone #RB6-8C5; Lot #B288472; Biolegend, Inc. (San Diego, CA))
•Website: https://www.biolegend.com/en-us/products/apc-anti-mouse-ly-6g-ly-6c-gr-1-antibody-456
Manufacturer verified for use: flow cytometry
•Associated Figure(s): Fig 1c, Extended Data Fig 1b,c,g,i

Armenian Hamster PeCy7 anti-mouse CD11c (Cat. #: 117318; final use concentration: 0.5 µg/mL; Clone #N418; Lot #B269973; Biolegend, Inc. (San Diego, CA))
•Website: https://www.biolegend.com/en-us/products/pe-cyanine7-anti-mouse-cd11c-antibody-3086
•Associated Figure(s): Fig 1c,g,o, Fig 2h, Extended Data Fig 1b,c,g,l,m,w

Mouse PE anti-mouse NK1.1 (Cat. #: 156504; final use concentration: 0.5 µg/mL; Clone #PK136; Lot #B277026; Biolegend, Inc. (San Diego, CA))
•Website: https://www.biolegend.com/en-us/products/pe-anti-mouse-nk-1-1-antibody-16926
•Associated Figure(s): Extended Data Fig 1g,h,i,j,w

Rat PE anti-mouse CD49b (Cat. #: 108908; final use concentration: 0.5 µg/mL; Clone #DX5; Lot #4289830; Biolegend, Inc. (San Diego, CA))
•Website: https://www.biolegend.com/en-us/products/pe-anti-mouse-cd49b-pan-nk-cells-antibody-234
•Associated Figure(s): Fig 1c,g,o, Extended Data Fig 1b,c,m,w

Rat PerCP-Cy5.5 anti-mouse CD11b (Cat. #: 101228; final use concentration: 0.5 µg/mL; Clone #M1/70; Lot #B256661; Biolegend, Inc. (San Diego, CA))
•Website: https://www.biolegend.com/en-us/products/percp-cyanine5-5-anti-mouse-human-cd11b-antibody-4257
•Associated Figure(s): Fig 1c,g,o, Fig 2h, Extended Data Fig 1b,c,g,l,m,w

Rabbit anti-human PD-L1 (Cat. #: NBP1-76769; final use concentration: 0.5 µg/mL; clone #NBP1-76769; Lot #8293-1701; Novus Biologicals, Centennial, CO)
•Website: https://www.novusbio.com/products/pd-l1-antibody_nbp1-76769
•Associated Figure(s): Extended Data Fig. 7i

Rat PE anti-mouse PD-L1 (Cat. #: 124308; final use concentration: 0.5 µg/mL; clone #10F.9G2; Lot #B278301; Biolegend, (San Diego, CA))
•Website: https://www.biolegend.com/en-us/products/pe-anti-mouse-cd274-b7-h1-pd-l1-antibody-4497
•Associated Figure(s): Extended Data Fig. 7i

Phalloidin Alexafluor 488 (Cat. #: A12379; final use concentration: 0.2µg/mL; clone #NA; Lot #1737901; ThermoFisher Scientific (Waltham, MA))
•Website: https://www.thermofisher.com/order/catalog/product/A12379?ef_id=CjwKCAjwieuGBhAsEiwA1Ly_nbHglCspHMlFqajO6O2qiH_nv_inLTLvWwYXUfQUMh1OCprNzU7-

VBoCUI4QAvD_BwE:G:s&s_kwcid=AL!3652!3!447292198730!b!!g!!
&cid=bid_pca_iva_r01_co_cp1359_pjt0000_bid00000_0se_gaw_dy_pur_con&gclid=CjwKCAjwieuGBhAsEiwA1Ly_nbHglCspHMlFqaj
O6O2qiH_nv_inLTLvWwYXUfQUMh1OCprNzU7-VBoCUI4QAvD_BwE#/A12379?
ef_id=CjwKCAjwieuGBhAsEiwA1Ly_nbHglCspHMlFqajO6O2qiH_nv_inLTLvWwYXUfQUMh1OCprNzU7-
VBoCUI4QAvD_BwE:G:s&s_kwcid=AL!3652!3!447292198730!b!!g!!
&cid=bid_pca_iva_r01_co_cp1359_pjt0000_bid00000_0se_gaw_dy_pur_con&gclid=CjwKCAjwieuGBhAsEiwA1Ly_nbHglCspHMlFqaj
O6O2qiH_nv_inLTLvWwYXUfQUMh1OCprNzU7-VBoCUI4QAvD_BwE
•Associated Figure(s): Extended Data Fig. 7c

Mouse anti-FLAG (Cat. #: F1804; final use concentration: 0.2 µg/mL; clone #M2; Lot #SLBQ7119V; Millipore Sigma (St. Louis, MO))
•Website: https://www.sigmaaldrich.com/US/en/substance/monoclonalantiflagm2antibodyproducedinmouse1234598765?
context=product
•Associated Figure(s): Extended Data Fig. 1i, extended data 6c

Fabbit polyclonal anti-HLA-A (Cat. #: 15240-1-AP; final use concentration: 0.2 µg/mL; clone # NA; Lot #00006298; Proteintech (Rosemont, IL))
•Website: https://www.ptglab.com/products/HLA-A-Antibody-15240-1-AP.htm
•Associated Figure(s): Fig. 2a-c

Normal mouse IgG (Cat. #: SC-2025; final use concentration: NA; clone # NA; Lot #B0619; Santa Cruz Biotechnology (Dallas, TX))
•Website: https://www.scbt.com/p/normal-mouse-igg
•Associated Figure(s): Fig 2c

Rabbit anti-KDEL (Cat. #: PA1-013; final use concentration: 0.1 µg/mL; clone # JB42-04; Lot # VG3025834; ThermoFisher Scientific (Waltham, MA))
•Website: https://www.thermofisher.com/antibody/product/KDEL-Antibody-clone-JB42-04-Recombinant-Monoclonal/MA5-34715
•Associated Figure(s): Fig. 3d

Mouse anti-PD1 (Cat. #: BE-0146; Dosage 20 mg/kg; clone# RMP1-14; Lot# 780120S1C; Bioxcell (West Lebanon, NH))
•Website: https://bxcell.com/product/invivomab-anti-m-pd-1/
•Associated Figure(s): Fig 4a & b

Donkey anti-goat plus PLA secondary antibody (Cat. #: DUO-92003; final use concentration: NA; clone# NA; Lot# SLBZ8370; Millipore Sigma (St. Louis, MO))
•Website: https://www.sigmaaldrich.com/US/en/product/sigma/duo92003?context=product
•Associated Figure(s): Fig. 5b-5f, Extended Data Fig. 7ch

Donkey anti-mouse minus PLA secondary antibody (Cat. #: DUO-92004; final use concentration: NA clone# NA; Lot# SLCC8780; Millipore Sigma (St. Louis, MO))
•Website: https://www.sigmaaldrich.com/US/en/product/sigma/duo92004?context=product
•Associated Figure(s): Fig. 5b-5f, Extended Data Fig. 7cf

Rat anti-mouse CD8 (Cat. #: 550-281; final use concentration: 0.2 µg/mL; Clone# 53-6.7; Lot #5338976; BD Pharmingen (San Jose, CA))
•Website: https://www.bdbiosciences.com/en-us/products/reagents/flow-cytometry-reagents/research-reagents/single-color-antibodies-ruo/purified-rat-anti-mouse-cd8a.550281
•Associated Figure(s): Extended Data Fig. 1o, 1r

AlexaFluor 594 goat anti-rat secondary antibody (Cat. #: A11007; final use concentration: 0.05 µg/mL; Clone# NA; Lot# 1697164; ThermoFisher Scientific (Waltham, MA))
•Website: https://www.thermofisher.com/antibody/product/Goat-anti-Rat-IgG-H-L-Cross-Adsorbed-Secondary-Antibody-Polyclonal/A-11007
•Associated Figure(s): Extended Data Fig. 1o, 1r

Mouse anti-CD3 (Cat. #: SC-59013; final use concentration: 0.2 µg/mL; Clone# PS1; Lot # G2419; Santa Cruz Biotechnology (Dallas, TX)
•Website: https://www.scbt.com/p/cd3-antibody-ps1
•Associated Figure(s): Fig. 1i-1k

Mouse PE anti-pan-MHC-I (HLA-A,B,C) (Cat. #: 555553; Clone #: G46-2.6; final use dilution: 1:10; Lot #: multiple; BD Pharmingen (San Jose, CA))
•Website: https://www.bdbiosciences.com/en-us/products/reagents/flow-cytometry-reagents/research-reagents/single-color-antibodies-ruo/pe-mouse-anti-human-hla-abc.555553
•Associated Figure(s): Extended Data Fig. 6h

Mouse FITC anti-pan-MHC-II (HLA-DP, DQ, DQ)(Cat. #: 555558; Clone #: Tu39; Lot #: multiple; final use dilution: 1:10; BD Pharmingen (San Jose, CA))
•Website: https://www.bdbiosciences.com/en-us/products/reagents/flow-cytometry-reagents/research-reagents/single-color-antibodies-ruo/fitc-mouse-anti-human-hla-dr-dp-dq.555558
•Associated Figure(s): Extended Data Fig. 6h

Mouse PerPCy5.5 anti-CD45 (Cat. #: 45-9459-42; Clone #: 2D1; Lot #: multiple; final use dilution: 1:20; Invitrogen (Waltham, MA))
•Website: https://www.thermofisher.com/antibody/product/CD45-Antibody-clone-2D1-Monoclonal/45-9459-42
•Associated Figure(s): Extended Data Fig. 6h

Mouse APC anti-CD90 (Cat. #: 328114; Clone #: 5E10; Lot #: multiple; final use dilution: 1:20; Biolegend (San Diego, CA))
•Website: https://www.biolegend.com/en-us/products/apc-anti-human-cd90-thy1-antibody-4116

•Associated Figure(s): Extended Data Fig. 6h

Mouse BV421 anti EpCAM (Cat. #: 324220; Clone #: 9C4; Lot #: multiple; final use dilution: 1:20; Biolegend (San Diego, CA)).
•Website: https://www.biolegend.com/en-us/products/brilliant-violet-421-anti-human-cd326-epcam-antibody-7549
•Associated Figure(s): Extended Data Fig. 6h

Biotinylated AAL (Cat. #: B-1395; final use concentration: 0.4 µg/mL; Lot #ZH0504; Vector Labs, Burlingame, CA)
•Website: https://vectorlabs.com/biotinylated-aleuria-aurantia-lectin-aal.html
•Associated Figure(s): Fig 2c, Fig 3e, Fig 5b-e, Extended Data 5b, Extended Data Fig 7c-f

Fluorescein-conjugated AAL (Cat. #: FL-1391; final use concentration: 0.4 µg/mL; Lot# ZF0326; Vector Laboratories, Burlingame, CA)
•Website: https://vectorlabs.com/fluorescein-labeled-aleuria-aurantia-lectin-aal.html
•Associated Figure(s): Fig 1i-k, Fig 3e, Fig 5b-e, Extended Data 1a,d,l, Extended Data 5b, Extended data 7c-f

Agarose UEA1 and AAL (Cat. #: AL-1393 and AL-1063-2, respectively; Lot# ZG0918 for AAL; Vector Laboratories, (Burlingame, CA))
•Website: https://vectorlabs.com/agarose-bound-aleuria-aurantia-lectin-aal.html https://vectorlabs.com/agarose-bound-ulex-europaeus-agglutinin-i-uea-i.html
•Associated Figure(s): Fig 2b, Fig 3c, Extended Data 6e

Fixable Live/Dead stain (Biolegend (San Jose, CA)
•Website:https://www.biolegend.com/en-us/products/zombie-nir-fixable-viability-kit-8657?GroupID=BLG2181
•Associated Figure(s): Fig. 1b-d, 1f-h, 1o, 2g,h, Extended Data Fig. 1b,c,f,g,h,l,j,m,n,p,q,v,w, 3d,e, 4a

PKH26 Millipore Sigma (Cat. #: 555553; St. Louis, MO))
•Website:https://www.sigmaaldrich.com/US/en/product/sigma/pkh26gl?gclid=CjwKCAjwieuGBhAsEiwA1Ly_nQjfjFZr31KPneW6vzdP_OXJyufdHtdDgQD5n88STPgkzO-GumvM8hoCESoQAvD_BwE
•Associated Figure(s): Fig. 3e, Extended Fig. 5b, 7i

Alexa Fluor 647 anti-human/mouse Granzyme B Antibody (Cat. #: 515406; Lot # B266742; Concentration: 0.5 µg/mL; Biolegend (San Diego, CA))
Website: https://www.biolegend.com/en-us/products/alexa-fluor-647-anti-human-mouse-granzyme-b-antibody-6067?GroupID=BLG15670
Associated Figures: Extended Data Fig 3d & e

BUV805 Rat Anti-Mouse CD8a (Cat. # 612898; Lot # 1194016; Concentration: 0.5 µg/mL; BD Biosciences (Franklin Lakes, NJ))
Website: https://www.bdbiosciences.com/en-us/products/reagents/flow-cytometry-reagents/research-reagents/single-color-antibodies-ruo/buv805-rat-anti-mouse-cd8a.612898
Associated Figures: Extended Data Fig 3c-e, Fig. 4b

BV421 Rat Anti-Mouse I-A/I-E (Cat.# 562564 Lot # 1074223; Concentration: 0.5 µg/mL; BD Biosciences (Franklin Lakes, NJ))
Website: https://www.bdbiosciences.com/en-us/products/reagents/flow-cytometry-reagents/research-reagents/single-color-antibodies-ruo/bv421-rat-anti-mouse-i-a-i-e.562564
Associated Figures: Extended Data Fig 3c, Fig. 4b

Live/Dead Aqua (Cat# L34965; Lot #: multiple; ThermoFisher Scientific (Waltham, MA))
Website:https://www.thermofisher.com/order/catalog/product/L34957?s_kwcid=AL!3652!3!358452930868!e!!g!!live%20dead%20aqua&ef_id=CjwKCAjw8sCRBhA6EiwA6_IF4YuAc427TmvCQ_pkCYMPlc2WPRiJJVnVdniFZLRrqcfT57IgVnt6uxoCCaQQAvD_BwE:G:s&s_kwcid=AL!3652!3!358452930868!e!!g!!live%20dead%20aqua&cid=bid_pca_frg_r01_co_cp1359_pjt0000_bid00000_0se_gaw_bt_pur_con&gclid=CjwKCAjw8sCRBhA6EiwA6_IF4YuAc427TmvCQ_pkCYMPlc2WPRiJJVnVdniFZLRrqcfT57IgVnt6uxoCCaQQAvD_BwE
Associated Figures: Extended Data Fig 3c-e, Fig. 4b

BV605 anti-mouse CD11c (Cat. #:117334; Lot # B342521; Concentration: 0.5 µg/mL; Biolegend (San Diego, CA))
Website: https://www.biolegend.com/en-us/products/brilliant-violet-605-anti-mouse-cd11c-antibody-7865?GroupID=BLG11937
Associated Figures: Extended Data Fig 3c, Fig. 4b

BV711 Rat anti-mouse CD11b (Cat.# 563168; Lot # 1116158; Concentration: 0.5 µg/mL; BD Biosciences (Franklin Lakes, NJ))
Website: https://www.bdbiosciences.com/en-us/products/reagents/flow-cytometry-reagents/research-reagents/single-color-antibodies-ruo/bv711-rat-anti-cd11b.563168
Associated Figures: Extended Data Fig 3c-e, Fig 4b

BV421 Rat anti-mouse CD44 (Cat.# 563970; Lot #0337154; Concentration: 0.5 µg/mL; BD Biosciences (Franklin Lakes, NJ))
Website: https://www.bdbiosciences.com/en-us/products/reagents/flow-cytometry-reagents/research-reagents/single-color-antibodies-ruo/bv421-rat-anti-mouse-cd44.563970
Associated Figures: Extended Data Fig 3c, Fig 4b

BV650 Rat anti-mouse CD4 (Cat.# 563747; Lot #1013120; Concentration: 0.5 µg/mL; BD Biosciences (Franklin Lakes, NJ))
Website: https://www.bdbiosciences.com/en-us/products/reagents/flow-cytometry-reagents/research-reagents/single-color-antibodies-ruo/bv650-rat-anti-mouse-cd4.563747
Associated Figures: Extended Data Fig 3c-e, Fig 4b

BV785 Rat anti-mouse CD45 (Cat.# 564225; Lot #1175935; Concentration: 0.5 µg/mL; BD Biosciences (Franklin Lakes, NJ))
Website: https://www.bdbiosciences.com/en-us/products/reagents/flow-cytometry-reagents/research-reagents/single-color-antibodies-ruo/bv786-rat-anti-mouse-cd45.564225
Associated Figures: Extended Data Fig 3c-e, Fig 4b

APC anti-mouse F4/80 (Cat. #: 123116; Lot # B298926; Concentration: 0.5 µg/mL; Biolegend (San Diego, CA))
Website: https://www.biolegend.com/en-gb/products/apc-anti-mouse-f4-80-antibody-4071?GroupID=BLG5319
Associated Figures: Extended Data Fig 3c, Fig 4b

PeCy anti-mouse CD103 (Cat. #: 121426; Lot # B283947; Concentration: 0.5 µg/mL; Biolegend (San Diego, CA))
Website: https://www.biolegend.com/en-us/products/pe-cyanine7-anti-mouse-cd103-antibody-9899?GroupID=BLG7093
Associated Figures: Extended Data Fig 3c, Fig 4b

BUV Rat anti-mouse CD62L (Cat.# 612833; Lot #111748; Concentration: 0.5 µg/mL; BD Biosciences, (Franklin Lakes, NJ))
Website: https://www.bdbiosciences.com/en-us/products/reagents/flow-cytometry-reagents/research-reagents/single-color-antibodies/buv737-rat-anti-mouse-cd62l.612833
Associated Figures: Extended Data Fig 3c, Fig 4b

PeCy7 anti-mouse CRTAM (Cat. #: 142013; Lot # B285616; Concentration: 0.5 µg/mL; Biolegend, (San Diego, CA))
Website: https://www.biolegend.com/en-us/products/pe-cyanine7-anti-mouse-cd355-crtam-antibody-15073?GroupID=BLG9494
Associated Figures: Extended Data Fig 3d-e, Fig 4b

APC-R700 hamster anti-mouse CD95 (Cat.# 565130; Lot #1057239; Concentration: 0.5 µg/mL; BD Biosciences (Franklin Lakes, NJ))
Website: https://www.bdbiosciences.com/en-us/products/reagents/flow-cytometry-reagents/research-reagents/single-color-antibodies-ruo/apc-r700-hamster-anti-mouse-cd95.565130
Associated Figures: Extended Data Fig 3c, Fig 4b

PE-Dazzle Hamster anti-mouse FCεR1 (Cat. #: 139319; Lot # B343474; Concentration: 0.5 µg/mL; Biolegend (San Diego, CA))
Website: https://www.biolegend.com/en-us/products/pe-dazzle-594-anti-mouse-fcepsilonrialpha-antibody-14527?GroupID=BLG6716
Associated Figures: Extended Data Fig 3c, Fig 4b

Rabbit Calnexin (C5C9) R1 (Cat. #: 2679T; Lot # 4; Concentration: 1/1000; Cell Signaling Technology (Danvers, MA))
Website: https://www.cellsignal.com/products/primary-antibodies/calnexin-c5c9-rabbit-mab/2679
Associated Figures: Extended Data Fig 6d
Finglimod (hydrochloride) (FTY720) (Cat. #: 10006292; Lot # 0572050-040; Concentration: 20 µg per mouse every 2 days; Cayman Chemical (Ann Arbor MI))
Website: https://www.caymanchem.com/product/10006292/fingolimod-(hydrochloride)
Associated Figures: Extended Data Fig 3b-e

Goat anti-Integrin β5 (Cat#: ab31327; Lot# GR68472-8; Concentration: 0.5 µg/mL; Abcam (Cambridge, UK)))
Website: https://www.abcam.com/integrin-beta-5-antibody-ab31327.html
Associated Figures: Extended Data Fig 2e

Human Easy Sep CD4 isolation negative selection cocktail (Cat#: 17952; Lot# 10000072656; Stem Cell Technologies (Vancouver, Canada))
Website: https://www.stemcell.com/easysep-human-cd4-t-cell-isolation-kit.html
Associated Figures: Extended Data Fig 2a-e

Ficoll-Paque PLUS (Cat# 17144002; Lot# 10305896; Cytiva (Marlborough, MA))
Website: https://www.cytivalifesciences.com/en/us/shop/cell-therapy/media/ficoll-paque-plus-density-gradient-media-p-05824
Associated Figures: Extended Data Fig 2a-e

CD3/CD28 human dynabeads (Cat# 11131D; Lot# Multiple; Thermofisher Scientific (Waltham, MA))
Website: https://www.thermofisher.com/order/catalog/product/11131D
Associated Figures: Extended Data Fig 2a-e

Phospho-PKA Substrate (RRXS*/T*) (Cat. #: 9624S; Lot # 21; Concentration: 1/1000; Cell Signaling (Danvers, MA))
Website: https://www.cellsignal.com/products/primary-antibodies/phospho-pka-substrate-rrxs-t-100g7e-rabbit-mab/9624#:~:text=Phospho%2DPKA%20substrate%2Dspecific%20antibodies,high%20throughput%20kinase%20drug%20discovery.
Associated Figures: Extended Data Fig 2b

Ponceau Stain, Proteomics Grade (Cat. #: 97063-650; Lot # 20J1356566; VWR (Radnor, PA))
Website: https://us.vwr.com/store/product/7437354/ponceau-s-proteomics-grade
Associated Figures: Extended Data Fig 2b-c

Validation

Mouse anti-V5 (Cat. #: v8012; final use concentration: 0.2 µg/mL; Clone #V5-10; Lot #00000999991; Millipore Sigma (St. Louis, MO))
•Website https://www.sigmaaldrich.com/US/en/product/sigma/v8012
•Manufacturer verified for use: immunocytochemistry, western blot
•Relevant Reference(s): Ortuno D, Carlisle HJ, Miller S. Does inactivation of USP14 enhance degradation of proteasomal substrates that are associated with neurodegenerative diseases? F1000Res. 2016 Feb 4;5:137. doi: 10.12688/f1000research.7800.2. PMID: 26998235; PMCID: PMC4792207.
Ciabatti E, González-Rueda A, Mariotti L, Morgese F, Tripodi M. Life-Long Genetic and Functional Access to Neural Circuits Using Self-Inactivating Rabies Virus. Cell. 2017 Jul 13;170(2):382-392.e14. doi: 10.1016/j.cell.2017.06.014. Epub 2017 Jul 6. PMID: 28689641; PMCID: PMC5509544
•Associated Figure(s): Fig 2c & 3c, Extended data fig 6a-d

Mouse anti-V5 gel (Cat. #:a7345; Clone # V5-10; Lot #119M4791V; Millipore Sigma (St. Louis, MO))
•Website https://www.sigmaaldrich.com/US/en/product/sigma/a7345?context=product
•Manufacturer verified for use: affinity chromatography, immunoprecipitation

•Relevant Reference(s): Meng Q, Li M, Silberg MA, Conrad F, Bettencourt J, To R, Huang C, Ma J, Meyer K, Shimizu R, Cao L, Tomic MT, Marks JD. Domain-based assays of individual antibody concentrations in an oligoclonal combination targeting a single protein. Anal Biochem. 2012 Feb 15;421(2):351-61. doi: 10.1016/j.ab.2011.09.030. Epub 2011 Oct 6. PMID: 22037290; PMCID: PMC4209596.
Dasgupta A, Chen CH, Lee C, Gladfelter AS, Dunlap JC, Loros JJ. Biological Significance of Photoreceptor Photocycle Length: VIVID Photocycle Governs the Dynamic VIVID-White Collar Complex Pool Mediating Photo-adaptation and Response to Changes in Light Intensity. PLoS Genet. 2015 May 15;11(5):e1005215. doi: 10.1371/journal.pgen.1005215. PMID: 25978382; PMCID: PMC4433212
•Associated Figure(s): Fig 2c, Extended data fig 6a-d

Mouse anti-human HLA-DRB1 (Cat. #:ab215835; final use concentration: 0.2 µg/mL for IF; Clone #HLA-DRB/1067; Lot# NA; Abcam (Cambridge, UK))
•Website https://www.abcam.com/hla-class-ii-drb1-antibody-hla-drb1067-ab215835.html
•Manufacturer verified for use: immunohistochemistry, western blot, flow cytometry, immunocytochemistry
•Relevant Reference(s): NA
•Associated Figure(s): Fig 3d, Fig 5b-f, Extended Data Fig 7b-e

Rabbit anti-human HLA-DRB1 (Cat. #:ab92371; final use concentration: 0.2 µg/mL for WB; Polyclonal; Lot #GR922220-2; Abcam (Cambridge, UK))
•Website https://www.abcam.com/hla-class-ii-drb1-antibody-ab92371.html
•Manufacturer verified for use: western blot, ELISA
•Relevant Reference(s): NA
•Associated Figure(s): Fig. 2a-e, Fig 3e, Extended Fig 3b

Mouse anti-beta-tubulin (Cat. #: E7; final use concentration: 0.3 µg/mL; clone# E7; Lot# 11/29/18; developed by M. McCutcheon and S. Carroll and obtained from Developmental Studies Hybridoma Bank (University of Iowa, Iowa City, IA))
•Website https://dshb.biology.uiowa.edu/E7_2
•Manufacturer verified for use: immunofluorescence, immunohistochemistry, immunoprecipitation, western blot
•Relevant Reference(s): Chu DT, Klymkowsky MW. The appearance of acetylated alpha-tubulin during early development and cellular differentiation in Xenopus. Dev Biol. 1989 Nov;136(1):104-17. doi: 10.1016/0012-1606(89)90134-6. PMID: 2680681
Monyak RE, Emerson D, Schoenfeld BP, Zheng X, Chambers DB, Rosenfelt C, Langer S, Hinchey P, Choi CH, McDonald TV, Bolduc FV, Sehgal A, McBride SMJ, Jongens TA. Insulin signaling misregulation underlies circadian and cognitive deficits in a Drosophila fragile X model. Mol Psychiatry. 2017 Aug;22(8):1140-1148. doi: 10.1038/mp.2016.51. Epub 2016 Apr 19. PMID: 27090306; PMCID: PMC5071102
•Associated Figure(s): Fig 2a, Fig 3c,e, Extended Data Fig 1l, Extended Data Fig 5b, Extended Data Fig 6e

Goat anti-biotin (Cat. #: sp3000; final use concentration: 0.1 µg/mL; polyclonal; Lot# ZH0202; Vector Labs (Burlingame, CA))
•Website https://vectorlabs.com/goat-anti-biotin-unconjugated.html#documents
•Manufacturer verified for use: immunohistochemistry, immunofluorescence, in situ hybridization, blotting, ELISPOT, ELISA
•Relevant Reference(s): Mosialou I, Shikhel S, Liu JM, Maurizi A, Luo N, He Z, Huang Y, Zong H, Friedman RA, Barasch J, Lanzano P, Deng L, Leibel RL, Rubin M, Nickolas T, Chung W, Zeltser LM, Williams KW, Pessin JE, Kousteni S. MC4R-dependent suppression of appetite by bone-derived lipocalin 2. Nature. 2017 Mar 16;543(7645):385-390. doi: 10.1038/nature21697. Epub 2017 Mar 8. Erratum in: Nature. 2017 Jun 14;546(7658):440. PMID: 28273060; PMCID: PMC5975642
Cholanian M, Krajewski-Hall SJ, McMullen NT, Rance NE. Chronic oestradiol reduces the dendritic spine density of KNDy (kisspeptin/neurokinin B/dynorphin) neurones in the arcuate nucleus of ovariectomised Tac2-enhanced green fluorescent protein transgenic mice. J Neuroendocrinol. 2015 Apr;27(4):253-63. doi: 10.1111/jne.12263. PMID: 25659412; PMCID: PMC4788980
•Associated Figure(s): Fig 5b-f, Extended Data Fig 7b-h

Anti-mouse CD4 (Cat. #: BE0003-1; Dosage: 20 mg/kg for immunodepletion; Clone# GK1.5; Lot# 689518A1; Bioxcell (West Lebanon, NH))
•Website https://bxcell.com/product/m-cd4/
•Manufacturer verified for use: immunodepletion, flow cytometry, western blot
•Relevant Reference(s): Balogh KN, Templeton DJ, Cross JV. Macrophage Migration Inhibitory Factor protects cancer cells from immunogenic cell death and impairs anti-tumor immune responses. PLoS One. 2018 Jun 4;13(6):e0197702. doi: 10.1371/journal.pone.0197702. PMID: 29864117; PMCID: PMC5986154.
Budda SA, Zenewicz LA. IL-22 deficiency increases CD4 T cell responses to mucosal immunization. Vaccine. 2018 Jun 14;36(25):3694-3700. doi: 10.1016/j.vaccine.2018.05.011. Epub 2018 May 5. PMID: 29739717
•Associated Figure(s): Fig 1n-o, Extended Data Fig 1 n,p,q,u,v,w

Anti-mouse CD8 (Cat. #: BE0061; Dosage: 20 mg/kg for immunodepletion; Clone# 2.43; Lot #: 643017F1; Bioxcell (West Lebanon, NH))
•Website https://bxcell.com/product/m-cd8a-2/
•Manufacturer verified for use: immunodepletion, western blot
•Relevant Reference(s): Balogh KN, Templeton DJ, Cross JV. Macrophage Migration Inhibitory Factor protects cancer cells from immunogenic cell death and impairs anti-tumor immune responses. PLoS One. 2018 Jun 4;13(6):e0197702. doi: 10.1371/journal.pone.0197702. PMID: 29864117; PMCID: PMC5986154.
Li J, Lee Y, Li Y, Jiang Y, Lu H, Zang W, Zhao X, Liu L, Chen Y, Tan H, Yang Z, Zhang MQ, Mak TW, Ni L, Dong C. Co-inhibitory Molecule B7 Superfamily Member 1 Expressed by Tumor-Infiltrating Myeloid Cells Induces Dysfunction of Anti-tumor CD8+ T Cells. Immunity. 2018 Apr 17;48(4):773-786.e5. doi: 10.1016/j.immuni.2018.03.018. Epub 2018 Apr 3. PMID: 29625896
•Associated Figure(s): Fig 1m, Extended Data 1o,r,t

Anti-mouse IgGk horseradish peroxidase (HRP) (Cat. #: SC-516102; final use concentration: 0.04 µg/mL; Clone: NA; Lot#F1620; Santa Cruz Biotechnology (Dallas, TX))
•Website https://www.scbt.com/p/m-igg-kappa-bp-hrp
•Manufacturer verified for use: western blot, immunohistochemistry
•Relevant Reference(s): Mani R, Rose S, Suresh A, Sambantham S, Anandan B, Ibrahim M, Meena B. Cellular alterations and damage to the renal tissue of marine catfish Arius arius following Cd exposure and the possible sequestrant role of Metallothionein. Mar Pollut Bull. 2021 Feb;163:111930. doi: 10.1016/j.marpolbul.2020.111930. Epub 2020 Dec 26. PMID: 33373888.

Franco-Molina MA, Santana-Krímskaya SE, Madrigal-de-León LM, Coronado-Cerda EE, Zárate-Triviño DG, Hernández-Martínez SP, García-Coronado PL, Rodríguez-Padilla C. Evaluation of the cytotoxic and immunogenic potential of temozolamide, panobinostat, and Lophophora williamsii extract against C6 glioma cells. EXCLI J. 2021 Mar 9;20:614-624. doi: 10.17179/excli2020-3181. PMID: 33883986; PMCID: PMC8056056
•Associated Figure(s): Fig 2a-c, Fig 3c, Extended Data Fig 1l, Extended Data Fig 5b

Mouse anti-rabbit HRP (Cat. #: SC-2357; final use concentration: 0.04 µg/mL; Clone# NA; Lot# G0720; Santa Cruz Biotechnology (Dallas, TX))
•Website https://www.scbt.com/p/mouse-anti-rabbit-igg-hrp
•Manufacturer verified for use: western blot, immunohistochemistry
•Relevant Reference(s): Mani R, Rose S, Suresh A, Sambantham S, Anandan B, Ibrahim M, Meena B. Cellular alterations and damage to the renal tissue of marine catfish Arius arius following Cd exposure and the possible sequestrant role of Metallothionein. Mar Pollut Bull. 2021 Feb;163:111930. doi: 10.1016/j.marpolbul.2020.111930. Epub 2020 Dec 26. PMID: 33373888
Guo L, Bai Y, Ni T, Li Y, Cao R, Ji S, Li S. MicroRNA-153-3p suppresses retinoblastoma cell growth and invasion via targeting the IGF1R/Raf/MEK and IGF1R/PI3K/AKT signaling pathways. Int J Oncol. 2021 Jul;59(1):47. doi: 10.3892/ijo.2021.5227. Epub 2021 May 26. PMID: 34036380; PMCID: PMC8143749.
•Associated Figure(s): Fig 2a-c, Fig 3c, Extended Data Fig 1l, Extended Data Fig 5b

Goat anti-rabbit AlexaFluor 488 (Cat. #: A11008; final use concentration: 0.04 µg/mL; Clone # NA; Lot #1275894; ThermoFisher Scientific (Waltham, MA))
•Website https://www.thermofisher.com/antibody/product/Goat-anti-Rabbit-IgG-H-L-Highly-Cross-Adsorbed-Secondary-Antibody-Polyclonal/A32731
•Manufacturer verified for use: western blot, immunocytochemistry
•Relevant Reference(s): Saju JM, Hossain MS, Liew WC, Pradhan A, Thevasagayam NM, Tan LSE, Anand A, Olsson PE, Orbán L. Heat Shock Factor 5 Is Essential for Spermatogenesis in Zebrafish. Cell Rep. 2018 Dec 18;25(12):3252-3261.e4. doi: 10.1016/j.celrep.2018.11.090. PMID: 30566854
Fetoni AR, Zorzi V, Paciello F, Ziraldo G, Peres C, Raspa M, Scavizzi F, Salvatore AM, Crispino G, Tognola G, Gentile G, Spampinato AG, Cuccaro D, Guarnaccia M, Morello G, Van Camp G, Fransen E, Brumat M, Girotto G, Paludetti G, Gasparini P, Cavallaro S, Mammano F. Cx26 partial loss causes accelerated presbycusis by redox imbalance and dysregulation of Nfr2 pathway. Redox Biol. 2018 Oct;19:301-317. doi: 10.1016/j.redox.2018.08.002. Epub 2018 Aug 7. PMID: 30199819; PMCID: PMC6129666.
•Associated Figure(s): Fig 3e, Extended Data 5b

Donkey anti-mouse AlexaFluor 594 (Cat. #: A21203; final use concentration: 0.05 µg/mL; Clone #NA; Lot #1918277; ThermoFisher Scientific (Waltham, MA))
•Website https://www.thermofisher.com/antibody/product/Donkey-anti-Mouse-IgG-H-L-Highly-Cross-Adsorbed-Secondary-Antibody-Polyclonal/A32744
•Manufacturer verified for use: immunocytochemistry
•Relevant Reference(s): Komabayashi-Suzuki M, Yamanishi E, Watanabe C, Okamura M, Tabata H, Iwai R, Ajioka I, Matsushita J, Kidoya H, Takakura N, Okamoto T, Kinoshita K, Ichihashi M, Nagata KI, Ema M, Mizutani KI. Spatiotemporally Dependent Vascularization Is Differently Utilized among Neural Progenitor Subtypes during Neocortical Development. Cell Rep. 2019 Oct 29;29(5):1113-1129.e5. doi: 10.1016/j.celrep.2019.09.048. PMID: 31665628
•Associated Figure(s): Fig 1i-k

AlexaFluor 594 donkey anti-rabbit (Cat. #: A21207; final use concentration: 0.05 µg/mL; Clone #NA; Lot #1938375; ThermoFisher Scientific (Waltham, MA))
•Website https://www.thermofisher.com/antibody/product/Donkey-anti-Rabbit-IgG-H-L-Highly-Cross-Adsorbed-Secondary-Antibody-Polyclonal/A-21207
•Manufacturer verified for use: immunocytochemistry, immunohistochemistry, flow cytometry, immunocytochemistry
•Relevant Reference(s): Baskfield A, Li R, Beers J, Zou J, Liu C, Zheng W. An induced pluripotent stem cell line (TRNDi009-C) from a Niemann-Pick disease type A patient carrying a heterozygous p.L302P (c.905 T>C) mutation in the SMPD1 gene. Stem Cell Res. 2019 Jul;38:101461. doi: 10.1016/j.scr.2019.101461. Epub 2019 May 15. PMID: 31132580; PMCID: PMC6686851
Hong J, Xu M, Li R, Cheng YS, Kouznetsova J, Beers J, Liu C, Zou J, Zheng W. Generation of an induced pluripotent stem cell line (TRNDi008-A) from a Hunter syndrome patient carrying a hemizygous 208insC mutation in the IDS gene. Stem Cell Res. 2019 May;37:101451. doi: 10.1016/j.scr.2019.101451. Epub 2019 Apr 25. PMID: 31071499; PMCID: PMC6642610
•Associated Figure(s): Fig 3d

Rabbit anti-Mart1 (Cat. #: SAB4500949; final use concentration: 0.2 µg/mL; Clone #NA; Lot #310257; Millipore Sigma (St. Louis, MO)
•Website https://www.sigmaaldrich.com/US/en/product/sigma/sab4500949?context=product
•Manufacturer verified for use: ELISA, immunohistochemistry, western blot
•Relevant Reference(s): Valmori D, Fonteneau JF, Lizana CM, Gervois N, Liénard D, Rimoldi D, Jongeneel V, Jotereau F, Cerottini JC, Romero P. Enhanced generation of specific tumor-reactive CTL in vitro by selected Melan-A/MART-1 immunodominant peptide analogues. J Immunol. 1998 Feb 15;160(4):1750-8. PMID: 9469433.
Chiu CG, Nakamura Y, Chong KK, Huang SK, Kawas NP, Triche T, Elashoff D, Kiyohara E, Irie RF, Morton DL, Hoon DS. Genome-wide characterization of circulating tumor cells identifies novel prognostic genomic alterations in systemic melanoma metastasis. Clin Chem. 2014 Jun;60(6):873-85. doi: 10.1373/clinchem.2013.213611. Epub 2014 Apr 9. PMID: 24718909
•Associated Figure(s): Fig 1i-k, Fig 5c-f, Extended Data Fig 1a,d,l, Extended Data Fig 4 b-h

Rabbit anti-S100 (Cat. #: Z0311; final use concentration: 0.2 µg/mL; Clone #NA; Lot #NA; Agilent Technologies (Santa Clara, CA))
•Website https://www.agilent.com/en/product/immunohistochemistry/antibodies-controls/primary-antibodies/s100-(dako-omnis)-76198
•Manufacturer verified for use: immunohistochemistry
•Relevant Reference(s): NA
•Associated Figure(s): Fig 1i-k, Fig 5c-f, Extended Data Fig 1a,d,l, Extended Data Fig 7 b-h

Rat APC anti-mouse CD3 (Cat. #: 100236; final use concentration: 0.5 µg/mL; Clone #17A2; Lot #B274725; Biolegend, inc. (San Diego, CA))

•Website https://www.biolegend.com/en-us/products/apc-anti-mouse-cd3-antibody-8055
•Manufacturer verified for use: flow cytometry
•Relevant Reference(s): Liu Y, et al. 2017. Oncogene. 10.1038/onc.2017.209
Agelidis A, et al. 2017. Cell Rep. 10.1016/j.celrep.2017.06.041
•Associated Figure(s): Fig 1c,d,g,h,o, Fig 2h, Extended Data Fig 1b,c,g,h,i,j,m,n,q,w, Extended Data Fig 3e

Rat Pacific Blue anti-mouse CD4 (Cat. #: 100428; final use concentration: 0.5 µg/mL; Clone #GK1.5; Lot #B265546; Biolegend, Inc. (San Diego, CA))
•Websitehttps://www.biolegend.com/en-us/products/pacific-blue-anti-mouse-cd4-antibody-3316?GroupID=BLG4745
•Manufacturer verified for use: flow cytometry
•Relevant Reference(s): Borkner L, et al. 2017. J Immunol. 10.4049/jimmunol.1602115
Vacca M, et al. 2017. Front Immunol. . 10.3389/fimmu.2017.01462
•Associated Figure(s): Fig 1d,h,o, Fig 2h, Extended Data Fig 1j,n,q,w, Extended Data Fig 3e

Rat BV785 anti-mouse CD8 (Cat. #: 100750; final use concentration: 0.5 µg/mL; Clone #53-6.7; Lot #B266841; Biolegend (San Diego, CA))
•Website https://www.biolegend.com/en-us/products/brilliant-violet-785-anti-mouse-cd8a-antibody-7957
•Manufacturer verified for use: flow cytometry
•Relevant Reference(s): Shih FF, et al. 2006. J. Immunol. 176:3438. Bouwer HGA, et al. 2006.
P. Natl. Acad. Sci. USA 103:5102.
•Associated Figure(s): Fig 1d,h,o, Fig 2h, Extended Data Fig 1j,w, Extended Data Fig 3e

Rat FITC anti-mouse F4/80 (Cat. #: 123108; final use concentration: 0.5 µg/mL; Clone #BM8; Lot #B257637; Biolegend, Inc (San Diego, CA))
•Website https://www.biolegend.com/en-us/products/fitc-anti-mouse-f4-80-antibody-4067
•Manufacturer verified for use: flow cytometry
•Relevant Reference(s): Kobayashi M, et al.2008. J. Leukoc. Biol. 83:1354
Poeckel D, et al. 2009. J. Biol Chem. 284:21077
•Associated Figure(s): Fig 1c,g, Extended Data Fig 1b,c,g,h,i,m

Rat APC anti-mouse GR-1 (Cat. #: 108412; final use concentration: 0.5 µg/mL; Clone #RB6-8C5; Lot #B288472; Biolegend, Inc. (San Diego, CA))
•Website https://www.biolegend.com/en-us/products/apc-anti-mouse-ly-6g-ly-6c-gr-1-antibody-456
•Manufacturer verified for use: flow cytometry
•Relevant Reference(s): Andoniou CE, et al. 2005. Nature Immunology 6:1011
Dzhagalov I, et al. 2007. Blood 109:1620
•Associated Figure(s): Fig 1c, Extended Data Fig 1b,c,g,i

Armenian Hamster PeCy7 anti-mouse CD11c (Cat. #: 117318; final use concentration: 0.5 µg/mL; Clone #N418; Lot #B269973; Biolegend, Inc. (San Diego, CA))
•Website https://www.biolegend.com/en-us/products/pe-cyanine7-anti-mouse-cd11c-antibody-3086
•Manufacturer verified for use: flow cytometry
•Relevant Reference(s): Cervantes-Barragan L, et al. 2007. Blood 109:1131.
Turnquist HR, et al. 2007. J. Immunol. 178:7018. (FC)
•Associated Figure(s): Fig 1c,g,o, Fig 2h, Extended Data Fig 1b,c,g,l,m,w

Mouse PE anti-mouse NK1.1 (Cat. #: 156504; final use concentration: 0.5 µg/mL; Clone #PK136; Lot #B277026; Biolegend, Inc. (San Diego, CA))
•Website https://www.biolegend.com/en-us/products/pe-anti-mouse-nk-1-1-antibody-16926
•Manufacturer verified for use: flow cytometry
•Relevant Reference(s): Lanier LL. 1997. Immunity 6:371.
Yokoyama WM, Seaman WE. 1993. Annu. Rev. Immunol. 11:613.
•Associated Figure(s): Extended Data Fig 1g,h,i,j,w

Rat PE anti-mouse CD49b (Cat. #: 108908; final use concentration: 0.5 µg/mL; Clone #DX5; Lot #4289830; Biolegend, Inc. (San Diego, CA))
•Website https://www.biolegend.com/en-us/products/pe-anti-mouse-cd49b-pan-nk-cells-antibody-234
•Manufacturer verified for use: flow cytometry
•Relevant Reference(s): Del Barco Barrantes I, et al. 2018. Stem Cell Reports. 10:257.
Seong J, et al. 2018. Development. 145:14
•Associated Figure(s): Fig 1c,g,o, Extended Data Fig 1b,c,m,w

Rat PerCP-Cy5.5 anti-mouse CD11b (Cat. #: 101228; final use concentration: 0.5 µg/mL; Clone #M1/70; Lot #B256661; Biolegend, Inc. (San Diego, CA))
•Website https://www.biolegend.com/en-us/products/percp-cyanine5-5-anti-mouse-human-cd11b-antibody-4257
•Manufacturer verified for use: flow cytometry
•Relevant Reference(s): Milasan A, et al. 2017. J Am Heart Assoc. 10.1161/JAHA.117.006892. Bennett FC, et al. 2018. Neuron. 98:1170
•Associated Figure(s): Fig 1c,g,o, Fig 2h, Extended Data Fig 1b,c,g,l,m,w

Rabbit anti-human PD-L1 (Cat. #: NBP1-76769; final use concentration: 0.5 µg/mL; clone #NBP1-76769; Lot #8293-1701; Novus Biologicals, Centennial, CO)
•Website https://www.novusbio.com/products/pd-l1-antibody_nbp1-76769
•Manufacturer verified for use: western blot, ELISA, flow cytometry, immunocytochemistry/immunofluorescence, immunohistochemistry (FFPE/frozen)
•Relevant Reference(s): Holokai L, Chakrabarti J, Lundy J et al. Murine- and Human-Derived Autologous Organoid/Immune Cell Co-

Cultures as Pre-Clinical Models of Pancreatic Ductal Adenocarcinoma Cancers Dec 17 2020. Yang A, Li MY, Zhang ZH et al. Erianin regulates programmed cell death ligand 1 expression and enhances cytotoxic T lymphocyte activity J Ethnopharmacol Nov 18 2020 [PMID: 33220359] (IHC, ICC/IF)
•Associated Figure(s): Extended Data Fig. 7i

Rat PE anti-mouse PD-L1 (Cat. #: 124308; final use concentration: 0.5 µg/mL; clone #10F.9G2; Lot #B278301; Biolegend, (San Diego, CA))
•Website https://www.biolegend.com/en-us/products/pe-anti-mouse-cd274-b7-h1-pd-l1-antibody-4497
•Manufacturer verified for use: flow cytometry
•Relevant Reference(s): Maier H, et al. 2007. J. Immunol. 178:2714. Meng Q, et al. 2006. Invest. Ophthalmol. Vis. Sci. 47:4444.
•Associated Figure(s): Extended Data Fig. 7i

Phalloidin Alexafluor 488 (Cat. #: A12379; final use concentration: 0.2µg/mL; clone #NA; Lot #1737901; ThermoFisher Scientific (Waltham, MA))
•Website https://www.thermofisher.com/order/catalog/product/A12379?ef_id=CjwKCAjwieuGBhAsEiwA1Ly_nbHglCspHMlFqajO6O2qiH_nv_inLTLvWwYXUfQUMh1OCprNzU7-VBoCUI4QAvD_BwE:G:s&s_kwcid=AL!3652!3!447292198730!b!!g!!&cid=bid_pca_iva_r01_co_cp1359_pjt0000_bid00000_0se_gaw_dy_pur_con&gclid=CjwKCAjwieuGBhAsEiwA1Ly_nbHglCspHMlFqajO6O2qiH_nv_inLTLvWwYXUfQUMh1OCprNzU7-VBoCUI4QAvD_BwE#/A12379?ef_id=CjwKCAjwieuGBhAsEiwA1Ly_nbHglCspHMlFqajO6O2qiH_nv_inLTLvWwYXUfQUMh1OCprNzU7-VBoCUI4QAvD_BwE:G:s&s_kwcid=AL!3652!3!447292198730!b!!g!!&cid=bid_pca_iva_r01_co_cp1359_pjt0000_bid00000_0se_gaw_dy_pur_con&gclid=CjwKCAjwieuGBhAsEiwA1Ly_nbHglCspHMlFqajO6O2qiH_nv_inLTLvWwYXUfQUMh1OCprNzU7-VBoCUI4QAvD_BwE
•Manufacturer verified for use: immunofluorescent immunocytochemistry
•Relevant Reference(s): Baddeley D, Crossman D, Rossberger S, Cheyne JE, Montgomery JM, Jayasinghe ID, Cremer C, Cannell MB, Soeller C,
PLoS One (2011) 6:e20645-e20645
•Associated Figure(s): Extended Data Fig. 7c

Mouse anti-FLAG (Cat. #: F1804; final use concentration: 0.2 µg/mL; clone #M2; Lot #SLBQ7119V; Millipore Sigma (St. Louis, MO))
•Website https://www.sigmaaldrich.com/US/en/substance/monoclonalantiflagm2antibodyproducedinmouse1234598765?context=product
•Manufacturer verified for use: western blot, immunoprecipitation, immunohistochemistry, immunofluorescence, immunocytochemistry.
•Relevant Reference(s):
Monika Srivastava et al. Nature communications, 6, 6253-6253 (2015-02-24)
•Associated Figure(s): Extended Data Fig. 1i, extended data 6c

Rabbit polyclonal anti-HLA-A (Cat. #: 15240-1-AP; final use concentration: 0.2 µg/mL; clone # NA; Lot #00006298; Proteintech (Rosemont, IL))
•Website https://www.ptglab.com/products/HLA-A-Antibody-15240-1-AP.htm
•Manufacturer verified for use: flow cytometry, immunofluorescence, immunohistochemistry, immunoprecipitation, western blot, ELISA
•Relevant Reference(s): Hao L et al. Front Oncol. 2020 May 6;10:615. doi: 10.3389/fonc.2020.00615
•Associated Figure(s): Fig. 2a-c

Normal mouse IgG (Cat. #: SC-2025; final use concentration: NA; clone # NA; Lot #B0619; Santa Cruz Biotechnology (Dallas, TX))
•Website https://www.scbt.com/p/normal-mouse-igg
•Manufacturer verified for use: negative control for western blot, immunoprecipitation, and immunohistochemistry
•Relevant Reference(s): Bejjani et al. Nucleic Acids Res. 2021 Mar 18;49(5):2488-2508. doi: 10.1093/nar/gkab053.
•Associated Figure(s): Fig 2c

Rabbit anti-KDEL (Cat. #: PA1-013; final use concentration: 0.1 µg/mL; clone # JB42-04; Lot # VG3025834; ThermoFisher Scientific (Waltham, MA))
•Website https://www.thermofisher.com/antibody/product/KDEL-Antibody-clone-JB42-04-Recombinant-Monoclonal/MA5-34715
•Manufacturer verified for use: western blot, immunohistochemistry, flow cytometry, immunocytochemistry (immunofluorescent)
•Relevant Reference(s): NA
•Associated Figure(s): Fig. 3d

Mouse anti-PD1 (Cat. #: BE-0146; Dosage 20 mg/kg; clone# RMP1-14; Lot# 780120S1C; Bioxcell (West Lebanon, NH))
•Website https://bxcell.com/product/invivomab-anti-m-pd-1/
•Manufacturer verified for use: immunocytochemistry, western blot, in vivo blockade of PD1:PD-L1 immune checkpoint
•Relevant Reference(s): Grasselly et al. Front Immunol. 2018 Oct 9;9:2100. doi: 10.3389/fimmu.2018.02100
•Associated Figure(s): Fig 4a & b

Donkey anti-goat plus PLA secondary antibody (Cat. #: DUO-92003; final use concentration: NA; clone# NA; Lot# SLBZ8370; Millipore Sigma (St. Louis, MO))
•Website https://www.sigmaaldrich.com/US/en/product/sigma/duo92003?context=product
•Manufacturer verified for use: proximity ligation assay
•Relevant Reference(s): A Frappaolo et al. Methods in cell biology, 137, 85-103 (2017-01-10), Annabel Christ et al. Developmental cell, 22(2), 268-278 (2012-02-22)
•Associated Figure(s): Fig. 5b-5f, Extended Data Fig. 7ch

Donkey anti-mouse minus PLA secondary antibody (Cat. #: DUO-92004; final use concentration: NA clone# NA; Lot# SLCC8780; Millipore Sigma (St. Louis, MO))
•Website https://www.sigmaaldrich.com/US/en/product/sigma/duo92004?context=product

•Manufacturer verified for use: proximity ligation assay
•Relevant Reference(s): A Frappaolo et al. Methods in cell biology, 137, 85-103 (2017-01-10), Annabel Christ et al. Developmental cell, 22(2), 268-278 (2012-02-22)
•Associated Figure(s): Fig. 5b-5f, Extended Data Fig. 7cf

Rat anti-mouse CD8 (Cat. #: 550-281; final use concentration: 0.2 µg/mL; Clone# 53-6.7; Lot #5338976; BD Pharmingen (San Jose, CA))
•Website https://www.bdbiosciences.com/en-us/products/reagents/flow-cytometry-reagents/research-reagents/single-color-antibodies-ruo/purified-rat-anti-mouse-cd8a.550281
•Manufacturer verified for use: flow cytometry, immunohistochemistry
•Relevant Reference(s): Alexander-Miller MA, Leggatt GR, Sarin A, Berzofsky JA. Role of antigen, CD8, and cytotoxic T lymphocyte (CTL) avidity in high dose antigen induction of apoptosis of effector CTL. J Exp Med. 1996; 184(2):485-492.
•Associated Figure(s): Extended Data Fig. 1o,r

AlexaFluor 594 goat anti-rat secondary antibody (Cat. #: A11007; final use concentration: 0.05 µg/mL; Clone# NA; Lot# 1697164; ThermoFisher Scientific (Waltham, MA))
•Website https://www.thermofisher.com/antibody/product/Goat-anti-Rat-IgG-H-L-Cross-Adsorbed-Secondary-Antibody-Polyclonal/A-11007
•Manufacturer verified for use: western blot, immunohistochemistry, immunocytochemistry, flow cytometry
•Relevant Reference(s): Bancells et al., Nat Microbiol. 2019 Jan;4(1):144-154. doi: 10.1038/s41564-018-0291-7.
•Associated Figure(s): Extended Data Fig. 1o,r

Mouse anti-CD3 (Cat. #: SC-59013; final use concentration: 0.2 µg/mL; Clone# PS1; Lot # G2419; Santa Cruz Biotechnology (Dallas, TX)
•Website https://www.scbt.com/p/cd3-antibody-ps1
•Manufacturer verified for use: western blot, immunoprecipitation, immunofluorescesnce, immunohistochemistry
•Relevant Reference(s): Ino et al., Oncotarget. 2019 Feb 1;10(10):1149-1159. doi: 10.18632/oncotarget.26646.
•Associated Figure(s): Fig. 1i-1k

Mouse PE anti-pan-MHC-I (HLA-A,B,C) (Cat. #: 555553; Clone #: G46-2.6; Lot #: multiple; BD Pharmingen (San Jose, CA)
•Website https://www.bdbiosciences.com/en-us/products/reagents/flow-cytometry-reagents/research-reagents/single-color-antibodies-ruo/pe-mouse-anti-human-hla-abc.555553
•Manufacturer verified for use: flow cytometry
•Relevant Reference(s): Crisa L, Cirulli V, Ellisman MH, Ishii JK, Elices MJ, Salomon DR. Cell adhesion and migration are regulated at distinct stages of thymic T cell development: the roles of fibronectin, VLA4, and VLA5. J Exp Med. 1996; 184(1):215-228.
•Associated Figure(s): Extended Data Fig. 6h

Mouse FITC anti-pan-MHC-II (HLA-DP, DQ, DQ)(Cat. #: 555558; Clone #: Tu39; Lot #: multiple; BD Pharmingen (San Jose, CA)
•Website https://www.bdbiosciences.com/en-us/products/reagents/flow-cytometry-reagents/research-reagents/single-color-antibodies-ruo/fitc-mouse-anti-human-hla-dr-dp-dq.555558
•Manufacturer verified for use: flow cytometry
•Relevant Reference(s): Pawelec G, Ziegler A, Wernet P. Dissection of human allostimulatory determinants with cloned T cells: stimulation inhibition by monoclonal antibodies TU22, 34, 35, 36, 37, 39, 43, and 58 against distinct human MHC class II molecules. Hum Immunol. 1985; 12(3):165-176.
•Associated Figure(s): Extended Data Fig. 6h

Mouse PerPCy5.5 anti-CD45 (Cat. #: 45-9459-42; Clone #: 2D1; Lot #: multiple; Invitrogen (Waltham, MA))
•Website https://www.thermofisher.com/antibody/product/CD45-Antibody-clone-2D1-Monoclonal/45-9459-42
•Manufacturer verified for use: flow cytometry
•Relevant Reference(s): Watanabe et al., JCI Insight. 2018 Apr 5;3(7):e99573. doi: 10.1172/jci.insight.99573.
•Associated Figure(s): Extended Data Fig. 6h

Mouse APC anti-CD90 (Cat. #: 328114; Clone #: 5E10; Lot #: multiple; Biolegend (San Diego, CA))
•Website https://www.biolegend.com/en-us/products/apc-anti-human-cd90-thy1-antibody-4116
•Manufacturer verified for use: flow cytometry
•Relevant Reference(s): Craig W, et al. 1993. J. Exp. Med. 177:1331.
•Associated Figure(s): Extended Data Fig. 6h

Mouse BV421 anti EpCAM (Cat. #: 324220; Clone #: 9C4; Lot #: multiple; Biolegend (San Diego, CA)).
•Website https://www.biolegend.com/en-us/products/brilliant-violet-421-anti-human-cd326-epcam-antibody-7549
•Manufacturer verified for use: flow cytometry
•Relevant Reference(s): Lammers R, et al. 2002. Exp. Hematol. 30:537.
•Associated Figure(s): Extended Data Fig. 6h

Fixable Live/Dead stain (Biolegend (San Jose, CA)
•Website https://www.biolegend.com/en-us/products/zombie-nir-fixable-viability-kit-8657?GroupID=BLG2181
•Manufacturer verified for use: flow cytometry
•Relevant Reference(s): McMaster SR, et al. 2015. PLoS One. 10:115725.
•Associated Figure(s): Fig. 1b-d, 1f-h, 1o, 2g,h, Extended Data Fig. 1b,c,f,g,h,l,j,m,n,p,q,v,w, 3d,e, 4a

PKH26 Millipore Sigma (Cat. #: 555553; St. Louis, MO))
•Websitehttps://www.sigmaaldrich.com/US/en/product/sigma/pkh26gl?gclid=CjwKCAjwieuGBhAsEiwA1Ly_nQjfjFZr31KPneW6vzdP_OXJyufdHtdDgQD5n88STPgkzO-GumvM8hoCESoQAvD_BwE
•Manufacturer verified for use: in vitro cell labeling, flow cytometry
•Relevant Reference(s): Ofra Ben Menachem-Zidon et al. PloS one, 14(6), e0218081-e0218081 (2019-06-14)
•Associated Figure(s): Fig. 3e, Extended Data Fig. 5b, 7i

Biotinylated AAL (Cat. #: B-1395; final use concentration: 0.4 µg/mL; Lot #ZH0504; Vector Labs, Burlingame, CA)
•Website https://vectorlabs.com/biotinylated-aleuria-aurantia-lectin-aal.html
•Manufacturer verified for use: immunohistochemistry/immunocytochemistry, immunofluorescence, blotting, elispot, ELISA
•Relevant Reference(s): Arriagada C, Cavieres VA, Luchsinger C, González AE, Muñoz VC, Cancino J, Burgos PV, Mardones GA. GOLPH3 Regulates EGFR in T98G Glioblastoma Cells by Modulating Its Glycosylation and Ubiquitylation. Int J Mol Sci. 2020 Nov 23;21(22):8880. doi: 10.3390/ijms21228880. PMID: 33238647; PMCID: PMC7700535.
Taubenschmid J, Stadlmann J, Jost M, Klokk TI, Rillahan CD, Leibbrandt A, Mechtler K, Paulson JC, Jude J, Zuber J, Sandvig K, Elling U, Marquardt T, Thiel C, Koerner C, Penninger JM. A vital sugar code for ricin toxicity. Cell Res. 2017 Nov;27(11):1351-1364. doi: 10.1038/cr.2017.116. Epub 2017 Sep 19. PMID: 28925387; PMCID: PMC5674155
•Associated Figure(s): Fig 2c, Fig 3e, Fig 5b-e, Extended Data 5b, Extended Data Fig 7c-f

Fluorescein-conjugated AAL (Cat. #: FL-1391; final use concentration: 0.4 µg/mL; Lot# ZF0326; Vector Laboratories, Burlingame, CA)
•Website https://vectorlabs.com/fluorescein-labeled-aleuria-aurantia-lectin-aal.html
•Manufacturer verified for use: immunofluorescence
•Relevant Reference(s): Bae K, Zheng W, Ma Y, Huang Z. Real-Time Monitoring of Pharmacokinetics of Antibiotics in Biofilms with Raman-Tagged Hyperspectral Stimulated Raman Scattering Microscopy. Theranostics. 2019 Feb 14;9(5):1348-1357. doi: 10.7150/thno.32043. PMID: 30867835; PMCID: PMC6401501.
Palaiologou E, Etter O, Goggin P, Chatelet DS, Johnston DA, Lofthouse EM, Doherty R, Pearson-Farr J, Sengers BG, Torrens C, Cleal JK, Page AM, Lewis RM. Human placental villi contain stromal macrovesicles associated with networks of stellate cells. J Anat. 2020 Jan;236(1):132-141. doi: 10.1111/joa.13082. Epub 2019 Sep 11. PMID: 31512233; PMCID: PMC6904625
•Associated Figure(s): Fig 1i-k, Fig 3e, Fig 5b-e, Extended Data 1a,d,l, Extended Data 5b, Extended data 7c-f

Agarose UEA1 and AAL (Cat. #: AL-1393 and AL-1063-2, respectively; Lot# ZG0918 for AAL; Vector Laboratories, (Burlingame, CA))
•Website https://vectorlabs.com/agarose-bound-aleuria-aurantia-lectin-aal.html https://vectorlabs.com/agarose-bound-ulex-europaeus-agglutinin-i-uea-i.html
•Manufacturer verified for use: affinity chromatography
•Relevant Reference(s): Amorim Filho L, Szwarcwald CL, Mateos SOG, Leon ACMP, Medronho RA, Veloso VG, Lopes JIF, Porto LCMS, Chieppe A, Werneck GL; Grupo Hemorio de Pesquisa em Covid-19. Seroprevalence of anti-SARS-CoV-2 among blood donors in Rio de Janeiro, Brazil. Rev Saude Publica. 2020;54:69. doi: 10.11606/s1518-8787.2020054002643. Epub 2020 Jul 6. PMID: 32638883; PMCID: PMC7334006.
Liu Y, He J, Li C, Benitez R, Fu S, Marrero J, Lubman DM. Identification and confirmation of biomarkers using an integrated platform for quantitative analysis of glycoproteins and their glycosylations. J Proteome Res. 2010 Feb 5;9(2):798-805. doi: 10.1021/pr900715p. PMID: 19961239; PMCID: PMC2838716.
•Associated Figure(s): Fig 2b, Fig 3c, Extended Data 6e

Alexa Fluor 647 anti-human/mouse Granzyme B Antibody (Cat. #: 515406; Lot # B266742; Concentration: 0.5 µg/mL; Biolegend (San Diego, CA))
Website: https://www.biolegend.com/en-us/products/alexa-fluor-647-anti-human-mouse-granzyme-b-antibody-6067?GroupID=BLG15670
Manufacturer's verified use: Flow Cytometry
Relevant References: Griffin BD, Muthumani K, Warner BM, Majer A, Hagan M, Audet J, Stein DR, Ranadheera C, Racine T, De La Vega MA, Piret J, Kucas S, Tran KN, Frost KL, De Graff C, Soule G, Scharikow L, Scott J, McTavish G, Smid V, Park YK, Maslow JN, Sardesai NY, Kim JJ, Yao XJ, Bello A, Lindsay R, Boivin G, Booth SA, Kobasa D, Embury-Hyatt C, Safronetz D, Weiner DB, Kobinger GP. DNA vaccination protects mice against Zika virus-induced damage to the testes. Nat Commun. 2017 Jun 7;8:15743. doi: 10.1038/ncomms15743. PMID: 28589934; PMCID: PMC5467228.
Gordon-Alonso M, Hirsch T, Wildmann C, van der Bruggen P. Galectin-3 captures interferon-gamma in the tumor matrix reducing chemokine gradient production and T-cell tumor infiltration. Nat Commun. 2017 Oct 6;8(1):793. doi: 10.1038/s41467-017-00925-6. PMID: 28986561; PMCID: PMC5630615.
Associated Figures: Extended Data Fig 3d & e

BUV805 Rat Anti-Mouse CD8a (Cat. # 612898; Lot # 1194016; Concentration: 0.5 µg/mL; BD Biosciences (Franklin Lakes, NJ))
Website: https://www.bdbiosciences.com/en-us/products/reagents/flow-cytometry-reagents/research-reagents/single-color-antibodies-ruo/buv805-rat-anti-mouse-cd8a.612898
Manufacturer's verified use: Flow Cytometry
Relevant References: Fujiura Y, Kawaguchi M, Kondo Y, et al. Development of CD8 alpha alpha+ intestinal intraepithelial T cells in beta 2-microglobulin- and/or TAP1-deficient mice. J Immunol. 1996; 156(8):2710-2715. (Clone-specific: Flow cytometry)
Ledbetter JA, Rouse RV, Micklem HS, Herzenberg LA. T cell subsets defined by expression of Lyt-1,2,3 and Thy-1 antigens. Two-parameter immunofluorescence and cytotoxicity analysis with monoclonal antibodies modifies current views. J Exp Med. 1980; 152(2):280-295.
Associated Figures: Extended Data Fig 3c-e, Fig. 4b

BV421 Rat Anti-Mouse I-A/I-E (Cat.# 562564 Lot # 1074223; Concentration: 0.5 µg/mL; BD Biosciences (Franklin Lakes, NJ))
Website: https://www.bdbiosciences.com/en-us/products/reagents/flow-cytometry-reagents/research-reagents/single-color-antibodies-ruo/bv421-rat-anti-mouse-i-a-i-e.562564
Manufacturer's verified use: Flow Cytometry, Immunofluorescence
Relevant References: Ernst DN, McQuitty DN, Weigle WO, Hobbs MV. Expression of membrane activation antigens on murine B lymphocytes stimulated with lipopolysaccharide. Cell Immunol. 1988; 114(1):161-173
Viville S, Neefjes J, Lotteau V, et al. Mice lacking the MHC class II-associated invariant chain. Cell. 1993; 72(4):635-648.
Associated Figures: Extended Data Fig 3c, Fig. 4b

Live/Dead Aqua (Cat# L34965; Lot #: multiple; ThermoFisher Scientific (Waltham, MA))
Website:https://www.thermofisher.com/order/catalog/product/L34957?s_kwcid=AL!3652!3!358452930868!e!!g!!live%20dead%20aqua&ef_id=CjwKCAjw8sCRBhA6EiwA6_IF4YuAc427TmvCQ_pkCYMPlc2WPRiJJVnVdniFZLRrqcfT57IgVnt6uxoCCaQQAvD_BwE:G:s&s_kwcid=AL!3652!3!358452930868!e!!g!!live%20dead%20aqua&cid=bid_pca_frg_r01_co_cp1359_pjt0000_bid00000_0se_gaw_bt_pur_con&gclid=CjwKCAjw8sCRBhA6EiwA6_IF4YuAc427T

mvCQ_pkCYMPlc2WPRiJJVnVdniFZLRrqcfT57IgVnt6uxoCCaQQAvD_BwE
Manufacturer's verified use: Flow Cytometry
Relevant References: Zeng X, Wei YL, Huang J, Newell EW, Yu H, Kidd BA, Kuhns MS, Waters RW, Davis MM, Weaver CT, Chien YH. γδ T cells recognize a microbial encoded B cell antigen to initiate a rapid antigen-specific interleukin-17 response. Immunity. 2012 Sep 21;37(3):524-34. doi: 10.1016/j.immuni.2012.06.011. Epub 2012 Sep 6. PMID: 22960222; PMCID: PMC3495981.
Idoyaga J, Suda N, Suda K, Park CG, Steinman RM. Antibody to Langerin/CD207 localizes large numbers of CD8alpha+ dendritic cells to the marginal zone of mouse spleen. Proc Natl Acad Sci U S A. 2009 Feb 3;106(5):1524-9. doi: 10.1073/pnas.0812247106. Epub 2009 Jan 23. PMID: 19168629; PMCID: PMC2635812.
Associated Figures: Extended Data Fig 3c-e, Fig. 4b

BV605 anti-mouse CD11c (Cat. #:117334; Lot # B342521; Concentration: 0.5 µg/mL; Biolegend (San Diego, CA))
Website: https://www.biolegend.com/en-us/products/brilliant-violet-605-anti-mouse-cd11c-antibody-7865?GroupID=BLG11937
Manufacturer's verified use: Flow Cytometry
Relevant References: de Mingo Pulido Á, Gardner A, Hiebler S, Soliman H, Rugo HS, Krummel MF, Coussens LM, Ruffell B. TIM-3 Regulates CD103+Dendritic Cell Function and Response to Chemotherapy in Breast Cancer. Cancer Cell. 2018 Jan 8;33(1):60-74.e6. doi: 10.1016/j.ccell.2017.11.019. PMID: 29316433; PMCID: PMC5764109.
Medler TR, Murugan D, Horton W, Kumar S, Cotechini T, Forsyth AM, Leyshock P, Leitenberger JJ, Kulesz-Martin M, Margolin AA, Werb Z, Coussens LM. Complement C5a Fosters Squamous Carcinogenesis and Limits T Cell Response to Chemotherapy. Cancer Cell. 2018 Oct 8;34(4):561-578.e6. doi: 10.1016/j.ccell.2018.09.003. PMID: 30300579; PMCID: PMC6246036.
Associated Figures: Extended Data Fig 3c, Fig. 4b

BV711 Rat anti-mouse CD11b (Cat.# 563168; Lot # 1116158; Concentration: 0.5 µg/mL; BD Biosciences (Franklin Lakes, NJ))
Website: https://www.bdbiosciences.com/en-us/products/reagents/flow-cytometry-reagents/research-reagents/single-color-antibodies-ruo/bv711-rat-anti-cd11b.563168
Manufacturer's verified use: Flow Cytometry
Relevant References: Ault KA, Springer TA. Cross-reaction of a rat-anti-mouse phagocyte-specific monoclonal antibody (anti-Mac-1) with human monocytes and natural killer cells. J Immunol. 1981 Jan;126(1):359-64. PMID: 7451976.
Driver DJ, McHeyzer-Williams LJ, Cool M, Stetson DB, McHeyzer-Williams MG. Development and maintenance of a B220- memory B cell compartment. J Immunol. 2001 Aug 1;167(3):1393-405. doi: 10.4049/jimmunol.167.3.1393. PMID: 11466358.
Associated Figures: Extended Data Fig 3c-e, Fig 4b

BV421 Rat anti-mouse CD44 (Cat.# 563970; Lot #0337154; Concentration: 0.5 µg/mL; BD Biosciences (Franklin Lakes, NJ))
Website: https://www.bdbiosciences.com/en-us/products/reagents/flow-cytometry-reagents/research-reagents/single-color-antibodies-ruo/bv421-rat-anti-mouse-cd44.563970
Manufacturer's verified use: Flow Cytometry
Relevant References: Ernst DN, Weigle WO, Noonan DJ, McQuitty DN, Hobbs MV. The age-associated increase in IFN-gamma synthesis by mouse CD8+ T cells correlates with shifts in the frequencies of cell subsets defined by membrane CD44, CD45RB, 3G11, and MEL-14 expression. J Immunol. 1993 Jul 15;151(2):575-87. PMID: 7687616.
Hathcock KS, Hirano H, Murakami S, Hodes RJ. CD44 expression on activated B cells. Differential capacity for CD44-dependent binding to hyaluronic acid. J Immunol. 1993 Dec 15;151(12):6712-22. PMID: 7505013.
Associated Figures: Extended Data Fig 3c, Fig 4b

BV650 Rat anti-mouse CD4 (Cat.# 563747; Lot #1013120; Concentration: 0.5 µg/mL; BD Biosciences (Franklin Lakes, NJ))
Website: https://www.bdbiosciences.com/en-us/products/reagents/flow-cytometry-reagents/research-reagents/single-color-antibodies-ruo/bv650-rat-anti-mouse-cd4.563747
Manufacturer's verified use: Flow Cytometry
Relevant References: Godfrey DI, Kennedy J, Mombaerts P, Tonegawa S, Zlotnik A. Onset of TCR-beta gene rearrangement and role of TCR-beta expression during CD3-CD4-CD8- thymocyte differentiation. J Immunol. 1994 May 15;152(10):4783-92. PMID: 7513723.
Tanaka T, Tsudo M, Karasuyama H, Kitamura F, Kono T, Hatakeyama M, Taniguchi T, Miyasaka M. A novel monoclonal antibody against murine IL-2 receptor beta-chain. Characterization of receptor expression in normal lymphoid cells and EL-4 cells. J Immunol. 1991 Oct 1;147(7):2222-8. PMID: 1918958.
Associated Figures: Extended Data Fig 3c-e, Fig 4b

BV786 Rat anti-mouse CD45 (Cat.# 564225; Lot #1175935; Concentration: 0.5 µg/mL; BD Biosciences (Franklin Lakes, NJ))
Website: https://www.bdbiosciences.com/en-us/products/reagents/flow-cytometry-reagents/research-reagents/single-color-antibodies-ruo/bv786-rat-anti-mouse-cd45.564225
Manufacturer's verified use: Flow Cytometry
Relevant References: Salazar GA, Peñaloza HF, Pardo-Roa C, Schultz BM, Muñoz-Durango N, Gómez RS, Salazar FJ, Pizarro DP, Riedel CA, González PA, Alvarez-Lobos M, Kalergis AM, Bueno SM. Interleukin-10 Production by T and B Cells Is a Key Factor to Promote Systemic Salmonella enterica Serovar Typhimurium Infection in Mice. Front Immunol. 2017 Aug 2;8:889. doi: 10.3389/fimmu.2017.00889. PMID: 28824622; PMCID: PMC5539121.
Gallizioli M, Miró-Mur F, Otxoa-de-Amezaga A, Cugota R, Salas-Perdomo A, Justicia C, Brait VH, Ruiz-Jaén F, Arbaizar-Rovirosa M, Pedragosa J, Bonfill-Teixidor E, Gelderblom M, Magnus T, Cano E, Del Fresno C, Sancho D, Planas AM. Dendritic Cells and Microglia Have Non-redundant Functions in the Inflamed Brain with Protective Effects of Type 1 cDCs. Cell Rep. 2020 Oct 20;33(3):108291. doi: 10.1016/j.celrep.2020.108291. PMID: 33086061; PMCID: PMC7578563.
Associated Figures: Extended Data Fig 3c-e, Fig 4b

APC anti-mouse F4/80 (Cat. #: 123116; Lot # B298926; Concentration: 0.5 µg/mL; Biolegend (San Diego, CA))
Website: https://www.biolegend.com/en-gb/products/apc-anti-mouse-f4-80-antibody-4071?GroupID=BLG5319
Manufacturer's verified use: Flow Cytometry
Relevant References: Qi F, Bai S, Wang D, Xu L, Hu H, Zeng S, Chai R, Liu B. Macrophages produce IL-33 by activating MAPK signaling pathway during RSV infection. Mol Immunol. 2017 Jul;87:284-292. doi: 10.1016/j.molimm.2017.05.008. Epub 2017 May 19. PMID: 28531812.
Gonçalves NP, Moreira J, Martins D, Vieira P, Obici L, Merlini G, Saraiva M, Saraiva MJ. Differential expression of Cathepsin E in transthyretin amyloidosis: from neuropathology to the immune system. J Neuroinflammation. 2017 Jun 6;14(1):115. doi: 10.1186/

s12974-017-0891-9. PMID: 28583160; PMCID: PMC5460450.
Associated Figures: Extended Data Fig 3c, Fig 4b

PeCy anti-mouse CD103 (Cat. #: 121426; Lot # B283947; Concentration: 0.5 µg/mL; Biolegend (San Diego, CA))
Website: https://www.biolegend.com/en-us/products/pe-cyanine7-anti-mouse-cd103-antibody-9899?GroupID=BLG7093
Manufacturer's verified use: Flow Cytometry
Relevant References: de Mingo Pulido Á, Gardner A, Hiebler S, Soliman H, Rugo HS, Krummel MF, Coussens LM, Ruffell B. TIM-3 Regulates CD103+Dendritic Cell Function and Response to Chemotherapy in Breast Cancer. Cancer Cell. 2018 Jan 8;33(1):60-74.e6. doi: 10.1016/j.ccell.2017.11.019. PMID: 29316433; PMCID: PMC5764109.
Hernández-Santos N, Wiesner DL, Fites JS, McDermott AJ, Warner T, Wüthrich M, Klein BS. Lung Epithelial Cells Coordinate Innate Lymphocytes and Immunity against Pulmonary Fungal Infection. Cell Host Microbe. 2018 Apr 11;23(4):511-522.e5. doi: 10.1016/j.chom.2018.02.011. Epub 2018 Mar 22. Erratum in: Cell Host Microbe. 2019 Apr 10;25(4):630. PMID: 29576482; PMCID: PMC5951304.
Associated Figures: Extended Data Fig 3c, Fig 4b

BUV Rat anti-mouse CD62L (Cat.# 612833; Lot #111748; Concentration: 0.5 µg/mL; BD Biosciences, (Franklin Lakes, NJ))
Website: https://www.bdbiosciences.com/en-us/products/reagents/flow-cytometry-reagents/research-reagents/single-color-antibodies/buv737-rat-anti-mouse-cd62l.612833
Manufacturer's verified use: Flow Cytometry
Relevant References: Jung TM, Gallatin WM, Weissman IL, Dailey MO. Down-regulation of homing receptors after T cell activation. J Immunol. 1988 Dec 15;141(12):4110-7. PMID: 3058798.
Yang G, Mizuno MT, Hellström KE, Chen L. B7-negative versus B7-positive P815 tumor: differential requirements for priming of an antitumor immune response in lymph nodes. J Immunol. 1997 Jan 15;158(2):851-8. PMID: 8993003.
Associated Figures: Extended Data Fig 3c, Fig 4b

PeCy7 anti-mouse CRTAM (Cat. #: 142013; Lot # B285616; Concentration: 0.5 µg/mL; Biolegend, (San Diego, CA))
Website: https://www.biolegend.com/en-us/products/pe-cyanine7-anti-mouse-cd355-crtam-antibody-15073?GroupID=BLG9494
Manufacturer's verified use: Flow Cytometry
Relevant References: Takeuchi A, Badr Mel S, Miyauchi K, Ishihara C, Onishi R, Guo Z, Sasaki Y, Ike H, Takumi A, Tsuji NM, Murakami Y, Katakai T, Kubo M, Saito T. CRTAM determines the CD4+ cytotoxic T lymphocyte lineage. J Exp Med. 2016 Jan 11;213(1):123-38. doi: 10.1084/jem.20150519. Epub 2015 Dec 22. PMID: 26694968; PMCID: PMC4710199.
Chang JT, Ciocca ML, Kinjyo I, Palanivel VR, McClurkin CE, Dejong CS, Mooney EC, Kim JS, Steinel NC, Oliaro J, Yin CC, Florea BI, Overkleeft HS, Berg LJ, Russell SM, Koretzky GA, Jordan MS, Reiner SL. Asymmetric proteasome segregation as a mechanism for unequal partitioning of the transcription factor T-bet during T lymphocyte division. Immunity. 2011 Apr 22;34(4):492-504. doi: 10.1016/j.immuni.2011.03.017. Epub 2011 Apr 14. PMID: 21497118; PMCID: PMC3088519.
Associated Figures: Extended Data Fig 3d-e, Fig 4b

APC-R700 hamster anti-mouse CD95 (Cat.# 565130; Lot #1057239; Concentration: 0.5 µg/mL; BD Biosciences (Franklin Lakes, NJ))
Website: https://www.bdbiosciences.com/en-us/products/reagents/flow-cytometry-reagents/research-reagents/single-color-antibodies-ruo/apc-r700-hamster-anti-mouse-cd95.565130
Manufacturer's verified use: Flow Cytometry
Relevant References: Yang Y, Mercep M, Ware CF, Ashwell JD. Fas and activation-induced Fas ligand mediate apoptosis of T cell hybridomas: inhibition of Fas ligand expression by retinoic acid and glucocorticoids. J Exp Med. 1995 May 1;181(5):1673-82. doi: 10.1084/jem.181.5.1673. PMID: 7536793; PMCID: PMC2192012.
Ogasawara J, Suda T, Nagata S. Selective apoptosis of CD4+CD8+ thymocytes by the anti-Fas antibody. J Exp Med. 1995 Feb 1;181(2):485-91. doi: 10.1084/jem.181.2.485. PMID: 7530758; PMCID: PMC2191897.
Associated Figures: Extended Data Fig 3c, Fig 4b

PE-Dazzle Hamster anti-mouse FCεR1 (Cat. #: 139319; Lot # B343474; Concentration: 0.5 µg/mL; Biolegend (San Diego, CA))
Website: https://www.biolegend.com/en-us/products/pe-dazzle-594-anti-mouse-fcepsilonrialpha-antibody-14527?GroupID=BLG6716
Manufacturer's verified use: Flow Cytometry
Relevant References: Obata K, Mukai K, Tsujimura Y, Ishiwata K, Kawano Y, Minegishi Y, Watanabe N, Karasuyama H. Basophils are essential initiators of a novel type of chronic allergic inflammation. Blood. 2007 Aug 1;110(3):913-20. doi: 10.1182/blood-2007-01-068718. Epub 2007 Apr 4. PMID: 17409268.
Arinobu Y, Iwasaki H, Gurish MF, Mizuno S, Shigematsu H, Ozawa H, Tenen DG, Austen KF, Akashi K. Developmental checkpoints of the basophil/mast cell lineages in adult murine hematopoiesis. Proc Natl Acad Sci U S A. 2005 Dec 13;102(50):18105-10. doi: 10.1073/pnas.0509148102. Epub 2005 Dec 5. PMID: 16330751; PMCID: PMC1312421.
Associated Figures: Extended Data Fig 3c, Fig 4b

Rabbit Calnexin (C5C9) R1 (Cat. #: 2679T; Lot # 4; Concentration: 1/1000; Cell Signaling Technology (Danvers, MA))
Website: https://www.cellsignal.com/products/primary-antibodies/calnexin-c5c9-rabbit-mab/2679
Manufacturer's verified use: Western Blotting, Immunohistochemistry, Immunofluorescence
Relevant References: Rogers MA, Buffolo F, Schlotter F, Atkins SK, Lee LH, Halu A, Blaser MC, Tsolaki E, Higashi H, Luther K, Daaboul G, Bouten CVC, Body SC, Singh SA, Bertazzo S, Libby P, Aikawa M, Aikawa E. Annexin A1-dependent tethering promotes extracellular vesicle aggregation revealed with single-extracellular vesicle analysis. Sci Adv. 2020 Sep 16;6(38):eabb1244. doi: 10.1126/sciadv.abb1244. PMID: 32938681; PMCID: PMC7494353.
Stefanius K, Servage K, de Souza Santos M, Gray HF, Toombs JE, Chimalapati S, Kim MS, Malladi VS, Brekken R, Orth K. Human pancreatic cancer cell exosomes, but not human normal cell exosomes, act as an initiator in cell transformation. Elife. 2019 May 28;8:e40226. doi: 10.7554/eLife.40226. PMID: 31134894; PMCID: PMC6538373.
Associated Figures: Extended Data Fig 6d

Goat anti-Integrin β5 (Cat#: ab31327; Lot# GR68472-8; Concentration: 0.5 µg/mL; Abcam (Cambridge, UK))
Website: https://www.abcam.com/integrin-beta-5-antibody-ab31327.html
Manufacturer's verified use: Western Blot
Relevant References: Kim W, Choi J, Yoon H, Lee J, Jun JH. Detrimental effects of lipopolysaccharide on the attachment and

outgrowth of various trophoblastic spheroids on human endometrial epithelial cells. Clin Exp Reprod Med. 2021 Jun;48(2):132-141. doi: 10.5653/cerm.2021.04448. Epub 2021 May 31. PMID: 34078006; PMCID: PMC8176151.
Dong H, Liu H, Zhou W, Zhang F, Li C, Chen J, Tan C, Tang B, Yu P. GLI1 activation by non-classical pathway integrin αvβ3/ERK1/2 maintains stem cell-like phenotype of multicellular aggregates in gastric cancer peritoneal metastasis. Cell Death Dis. 2019 Jul 31;10(8):574. doi: 10.1038/s41419-019-1776-x. PMID: 31366904; PMCID: PMC6668446.
Associated Figures: Extended Data Fig 2e

Phospho-PKA Substrate (RRXS*/T*) (Cat. #: 9624S; Lot # 21; Concentration: 1/1000; Cell Signaling (Danvers, MA))
Website: https://www.cellsignal.com/products/primary-antibodies/phospho-pka-substrate-rrxs-t-100g7e-rabbit-mab/9624#:~:text=Phospho%2DPKA%20substrate%2Dspecific%20antibodies,high%20throughput%20kinase%20drug%20discovery.
Manufacturer's verified use: Western Blotting, Immunorecipitation, ELISA
Relevant References: Li GB, Fu RQ, Shen HM, Zhou J, Hu XY, Liu YX, Li YN, Zhang HW, Liu X, Zhang YH, Huang C, Zhang R, Gao N. Polyphyllin I induces mitophagic and apoptotic cell death in human breast cancer cells by increasing mitochondrial PINK1 levels. Oncotarget. 2017 Feb 7;8(6):10359-10374. doi: 10.18632/oncotarget.14413. PMID: 28060722; PMCID: PMC5354664.
Christensen B, Nellemann B, Jørgensen JO, Pedersen SB, Jessen N. Erythropoietin does not activate erythropoietin receptor signaling or lipolytic pathways in human subcutaneous white adipose tissue in vivo. Lipids Health Dis. 2016 Sep 17;15(1):160. doi: 10.1186/s12944-016-0327-z. PMID: 27640183; PMCID: PMC5027120.
Associated Figures: Extended Data Fig 2b

Eukaryotic cell lines

Policy information about cell lines and Sex and Gender in Research

Cell line source(s)	NHEM (normal adult epidermal melanocytes) were obtained from Lonza. WM793 (original source: Wistar Institute), 1205Lu (original source: Wistar Institute), A375 (original source: ATCC), WM1366 (original source: Wistar Institute), WM164 (original source: Wistar Institute), and SW1 melanoma cells were obtained from the Ronai laboratory (Sanford-Burnham Prebys Medical Discovery Institute (La Jolla, CA)). WM983A and WM983B cells were purchased from Rockland Immunochemicals (Limerick, PA). WM115 and WM266-4 cells were purchased from ATCC (Manassas, VA). SM1 cells were obtained from the Smalley laboratory at Moffitt Cancer Center (original source was the Ribas Laboratory (Koya et al. 2012; PMID: 22693252).
Authentication	The identities of all cell lines (human and mouse) in the Lau Laboratory were initially verified as of December 2019 by short tandem repeat (STR)-based authentication "CellCheck" services provided through IDEXX BioResearch (idexxbioresearch.com). Repeat authentication of cell identities were performed annually on routinely used and newly acquired cell lines. The most recent round of authentication was performed as of October 2020. All rounds of authentication have confirmed the proper identities of all cell lines in the Lau laboratory (used in this study).
Mycoplasma contamination	In general, testing for mycoplasma, is performed once every 2-3 months on all cells in culture in the Lau laboratory, including those implemented in this study. We test using the Invivogen PlasmoTest Mycoplasma Detection Kit (https://www.invivogen.com/plasmotest). This assay delineates myco-positive from myco-negative cells using a colorimetric readout: positive cell media turns blue color (compared with a positive control in the kit); negative cell media does not.
Commonly misidentified lines (See ICLAC register)	We used 1205Lu cells, which are listed as a commonly misidentified cell line Our authentication showed that they are pure 1205Lu cultures without contaminant lines.

Animals and other research organisms

Policy information about studies involving animals; ARRIVE guidelines recommended for reporting animal research, and Sex and Gender in Research

Laboratory animals	Four-to-six-week-old female C3H/HeN and male C57BL6 mice were purchased from Charles Rivers Laboratories for the indicated experiments. Four-to-six-week-old male NSG mice from the Lau laboratory breeding colony were used for the indicated experiments.
Wild animals	This study did not involve wild animals.
Reporting on sex	Our study and its experiments and analyses were not focused on sex-associated outcomes/phenotypes/mechanisms. Thus, our animal modeling experiments included mice of both sexes. For example, SW1 mouse melanoma tumors (which originated in a female mouse) were grafted into syngeneic female C3H/HeN mice, whereas SM1 mouse melanoma tumors (which originated in a male mouse), were greated into syngeneic male C57BL6 mice.
Field-collected samples	This study did not involved field-collected samples.
Ethics oversight	All animals were housed at the Vincent A. Stabile Research building animal facility at H. Lee Moffitt Cancer Center & Research Institute, which is fully accredited by the Association for Assessment and Accreditation of Laboratory Animal Care International (AAALAC, #434), and are managed in accordance with the Guide for the Care and Use of Laboratory Animals ("The Guide"), the Animal Welfare Regulations Title 9 Code of Federal Regulations Subchapter A, "Animal Welfare", Parts 1-3 (AWR), the Public Health Service Policy on Humane Care and Use of Laboratory Animals (PHS Policy), and by the USF Institutional Animal Care and Use Committee's Principles and Procedures of Animal Care and Use (IACUC Principles). The experiments and protocols detailed in this

study received institutional approval by the Moffitt IACUC (RIS00001625). The Lau laboratory also has a Moffitt IACUC-approved, active NSG breeding colony (protocol: #IS00008112) from which we sourced NSG mice for the experiments indicated in the manuscript.

Note that full information on the approval of the study protocol must also be provided in the manuscript.

Clinical data

Policy information about clinical studies

All manuscripts should comply with the ICMJE guidelines for publication of clinical research and a completed CONSORT checklist must be included with all submissions.

Clinical trial registration	This study did not involve a clinical trial.
Study protocol	*Note where the full trial protocol can be accessed OR if not available, explain why.*
Data collection	*Describe the settings and locales of data collection, noting the time periods of recruitment and data collection.*
Outcomes	

Flow Cytometry

Plots

Confirm that:

☒ The axis labels state the marker and fluorochrome used (e.g. CD4-FITC).

☒ The axis scales are clearly visible. Include numbers along axes only for bottom left plot of group (a 'group' is an analysis of identical markers).

☒ All plots are contour plots with outliers or pseudocolor plots.

☒ A numerical value for number of cells or percentage (with statistics) is provided.

Methodology

Sample preparation	Surgically resected patient tumors or mouse tumors/spleens were minced to less than 1-mm fragments. Minced tumor sample was enzymatically digested in enzyme media comprised of RPMI with collagenase type IV (1 mg/mL), DNase type IV (30 U/mL), and hyaluronidase type V (100 µg/mL) (Sigma). Single cell suspensions were strained through 40-micron nylon mesh and counted for viability via trypan blue exclusion. Tumor homogenates were thawed and stained as indicated in the Methods section of the manuscript.
Instrument	BD FACsCalibur and BD LSRII Analyzer
Software	Cellquest v6, FACsDIVA v9, FlowJo v9
Cell population abundance	For Figs. 1 and 3 and Extended Data Fig. 1: itICs: total # ; 1x10^6 cells total were stained and analyzed per condition/group as in Supplementary Figure S1. % of subpopulation were based on that total. For Figs. 2 and 5: Dendritic and CD4+T cell subpopulations: 2 x 10^6 cells for tumors and 2.5 x 10^5 for lymph nodes were fixed and immunofluorescently stained and analyzed as in Supplementary Figures S2 and S3. For Fig. 4 and Extended Data Fig. 4: For cell surface AAL/HLA-DRB1/PKH26: a minimum of 1x10^4 cells were stained and analyzed as in Supplementary Figure S4. For Extended Data 5h: For cell surface pan-MHC-I and pan-MHC-II: 5x10^5 single cells were stained and analyzed as in Supplementary Figure S5.
Gating strategy	Detailed gating strategies are illustrated in the submitted Supplementary Information file. Generally, they are as follows: •For intratumoral immune cell (itIC) and splenic profiling: 1 x 10^6 itICs or splenocytes were fixed and immunofluorescently stained with the indicated itIC subpopulation markers. The cells were first gated for FSC/SSC and live/dead cell stain (Zombie NIR). Then the live stained single cells were subsequently gated for indicated stains per cell type as indicated (APC anti-mouse CD3, Pacific Blue anti-mouse CD4, BV785 anti-mouse CD8, FITC anti-mouse F4/80, PeCy7 anti-mouse CD11c, PE anti-mouse NK1.1 or PE anti-mouse DX5, and PerCP-Cy5.5 anti-mouse CD11b). •Assessment of dendritic subpopulations: 2 x 10^6 cells for tumors and 2.5 x 10^5 for lymph nodes were fixed and immunofluorescently stained and analyzed as in Supplementary Figures S2 and S3. Cells were gated for FSC/SSC, followed by live/dead stain (live/dead aqua). After gating for CD45+ cells, dendritic cells were gated for CD11c, using F4/80 to gate out macrophages/monocyte populations. For specific dendritic cell populations, MHCII+ cells were gated by CD103 and CD11b to identify cDC1s and FCεR1 was used to identify cDC2s and monocyte-derived dendritic cells (moDCs).

•Assessment of CD4+T cell subpopulations: 2 x 10^6 cells for tumors and 2.5 x 10^5 for lymph nodes were fixed and immunofluorescently stained and analyzed as in Supplementary Figures S2 and S3. Cells were gated for FSC/SSC, followed by live/dead stain (live/dead aqua). After gating for CD45+ cells, CD11b was used to exclude myeloid cells from the analysis. CD4 + and CD8+ subpopulations were gated from this, followed by CRTAM and Granzyme B as cytotoxic markers. For memory phenotypes, CD4+ and CD8+ cells were gated by CD62L and CD44, followed by CD95.

•Assessment of cell surface fucosylation, HLA-DRB1, and PD-L1:
Cells were first gated for FSC and SSC followed by gating for indicated stains. A minimum of 1x10^4 cells were analyzed within the singlet SSC-FSC gate for analysis of mean fluorescence intensity (MFI) of AAL-FITC, HLA-DRB1-AF488, or PKH26. AAL and HLA-DRB1 values were normalized to the respective PKH26 values (which reflect plasma membrane surface area) in order to discern AAL or HLA-DRB1 intensity per plasma membrane area.

•Assessment of cell surface pan-MHC-I and pan-MHC-II:
5x10^5 single cells were first gated for FSC and SSC followed by gating for live cells (based on live/dead cell staining (Zombie NIR) followed by gating for CD45- and CD90-/EPCAM-negative cells. Cells were then profiled for pan MHC-I (HLA-A/B/C) or pan MHC-II (HLA-DR/DP/DQ) (as shown in Supplementary Information).

**Note, flow cytometric plots that were analyzed in FlowJo were subsequently transformed into column charts, where signals measured by flow were normalized as indicated in the Methods and Figure Legends.

☒ Tick this box to confirm that a figure exemplifying the gating strategy is provided in the Supplementary Information.